SYNTHESIS AND CHARACTERIZATION OF IRON OXIDE NANOPARTICLES FOR INCORPORATION INTO ORGANIC ELECTRONIC DEVICES

SYNTHESIS AND CHARACTERIZATION OF IRON OXIDE NANOPARTICLES FOR INCORPORATION INTO ORGANIC ELECTRONIC DEVICES

By Kunyu Liang, B. ENG.

A THESIS SUBMITTED TO THE DEPARTMENT OF ENGINEERING PHYSICS AND THE SCHOOL OF GRADUATE STUDIES OF MCMASTER UNIVERSITY IN PARTIAL FULFILMENT OF THE REQUIREMENTS FOR THE DEGREE OF MASTER OF APPLIED SCIENCE

McMaster University Master of Applied Science (2018) Hamilton, Ontario (Engineering Physics)
TITLE:
AUTHOR: Kunyu Liang, B.Eng. (Jinan University, Guangzhou, China)
SUPERVISOR: Dr. Ayse Z. Turak
NUMBER OF PAGES: ix, 113

Abstract

Surface modification of electrodes becomes a powerful process to improve the performance of organic electronic devices such as organic light emitting diodes (OLEDs) and organic photovoltaic cells (OPVs), boosting their further commercialization. Effective improvement can be achieved by introducing several types of nanoparticles onto the electrodes. Magnetic fields also have influence in the organic electronics, due to charge transport mechanisms of organic semiconducting materials. Therefore, magnetic nanoparticles are of particular interest.

Magnetic γ-Fe_2O_3 nanoparticles have been produced using diblock copolymer reverse micelles method. The processes were elucidated in detail by Raman spectroscopy to reveal the iron oxide evolution. Compositional and structural information of individual γ-Fe_2O_3 nanoparticles were also characterized thoroughly by transmission electron microscopy (TEM) equipped with energy-dispersive X-ray spectroscopy (EDX) and electron energy loss spectroscopy (EELS), while their magnetic properties of the nanoparticles arrays were also evaluated by superconducting quantum interference device (SQUID) magnetometer. The low temperature annealing process was developed to facilitate the incorporation of γ-Fe_2O_3 nanoparticles in practical devices. Introducing γ-Fe_2O_3 nanoparticles onto the anode of basic OPV devices showed a positive effect on performance during the preliminary test.

By using several methods, dispersion of γ-Fe_2O_3 nanoparticles can be tuned, examined by disLocate which is a comprehensive suite of tools for quantitative dispersion analysis. Additionally, the size of the nanoparticles can be changed simply by changing the loading ratio of $FeCl_3$ below the maximum loading which was determined by quantum mechanical mapping using atomic force microscopy (AFM-QNM). With high control in terms of size and dispersion, the magnetic γ-Fe_2O_3 nanoparticles are ready to be employed to study the surface modification and magnetic effect on organic electronic devices.

List of publications

1. Bumstead, M., Liang, K., Hanta, G., Hui, L. S., Turak, A. (2018). disLocate: tools to rapidly quantify local intermolecular structure to assess two-dimensional order in self-assembled systems. Scientific reports, 8(1), 1554.

2. K. Liang, L.S. Hui, A. Turak, Evolution of iron oxide nanoparticles by the reverse micelle method, J. Mater. Chem. C (unpublished)

3. G. Hanta, K. Liang, A. Turak, Young's Modulus variations to track loading precursor salts in reverse micelles, Langmuir (unpublished)

4. S. Lee, G. Yun, J. Kim, G. Hanta, K. Liang, L. Kojvic, L. S. Hui, A. Turak, and W. Kim, Improved hole injection for blue phosphorescent organic light-emitting diodes using solution deposited tin oxide nanoparticles decorated ITO anodes, Applied Physics Letters (submitted)

Contents

List of Figures

Chapter 1

Intoduction

Thin film organic electronic devices are starting to exert a remarkable influence onto the modern electronic market. Next generation displays consisting of organic light emitting diodes (OLEDs) are already used in mobile phones, televisions, while significant progress is also being made in organic photovoltaic cells (OPVs) for harvesting solar energy.[1–3] The ongoing developments in this field are stimulated by the high processibility of organic semiconductor materials. Most of the organic semiconductor molecules are compatible with the convenient solution-based processing methods such as spin coating, inkjet printing, and roll-to-roll manufacturing,[4–7] giving rise to potential low-cost large scale device fabrication. Additionally, they have been incorporated into stretchable electronics which are another fast-growing advanced application.[8]

Despite the technical relevance, the relatively low efficiency in these devices compared to inorganic counterparts hinders their further commercialization. Nevertheless, several approaches can be applied to improve the performance of organic electronic devices. For instance, interfacial modification is one of the frequently-used method.[9] Organic devices are usually composed of several layers of different materials with conductive metal or metal oxide electrodes, leading to a variety of interfaces that impede the charge carriers transport during operation. Among various interfaces, the interface between electrodes and organic semiconductors is particularly important, as it has a direct impact on the charge extraction and injection processes.[10, 11] Thus, surface modification of electrodes play an important role in improving the performance of organic electronics, especially for OPV and OLED devices. This usually involves tuning

the work function (Fermi level, E_F) of the anode to match up the highest-occupied molecular orbital (HOMO) of the organic semiconductor to minimize the hole transport barrier.[11] Similarly, the work function of the cathode can be tailored to match up the lowest-unoccupied molecular orbital (LUMO) of the organic semiconductor to lower the electron transport barrier. A variety of high work function metal oxides[11] have been applied to modify the anodes, contributing to the state-of-the-art OPVs[12] and OLEDs[13].

In addition, magnetic fields have been found to be able to change the electroluminescence and photocurrent of organic semiconducting materials and thus organic electronic devices.[14] The excited states (excitons) of organic semiconductors are responsible for the electronic process. Due to the electron-spin multiplicities, the electron and hole can have either parallel or antiparallel spin configuration when the exciton is formed, giving rise to singlet and triplet excited states with a statistic ratio of 1:3 under random-spin capture. The singlet and triplet excited states can be mutually converted by spin flipping mechanisms. In principle, an external magnetic field can affect the spin configuration of electrons and holes during exciton formation or change the mutual conversion between singlet and triplet excited states, as it affects the spin precessions of electrons and holes. This can lead to the variation of the singlet and triplet ratio. Since the lifetime of singlet and triplet states are significantly different, the variation of the singlet to triplet ratio in turn influences the electronic processes of the devices, especially for OPV and OLED. Recently, it has been proposed that introducing a small amount of isolated magnetic nanoparticles onto the electrode can lead to a higher singlet/triplet ratio under small applied magnetic field and thus enhanced the performance of OPV[15] and OLEDs.[16, 17] Together with their abundance and stability, magnetic iron oxides are a good candidate for studying the magnetic effect in OPV and OLED devices. In addition, recent work has suggested that the thickness of the oxide film has a major affect on the performance improvements in OLEDs,[18] with a sub-monolayer/discontinuous film showing the greatest impact.[16] Therefore, it is of interest to pursue a method to produce and deposit magnetic iron oxides nanoparticles with high controllability in terms of size and dispersion, in order to explore the magnetic effect on the OPV and OLED devices.

The main focus of this thesis is to synthesize and deposit magnetic iron oxide

nanoparticles in highly controllable manner. In order to accomplish this goal, diblock copolymer reverse micelles have been applied in nanoparticle production. The process of iron oxide formation was determined in detail, which is described in Chapter 4. The composition, crystal structure, and magnetic properties of monolayer iron oxide nanoparticles are also investigated using a variety of characterization in Chapter 5, where the preliminary results from OPV devices incorporated with these monolayer nanoparticles are shown. Finally, the dispersion and size control of the nanoparticles are addressed in Chapter 6 for the potential application in the future.

Chapter 2

Background and motivation

2.1 Magnetic iron oxide nanoparticles

Magnetic iron oxide nanoparticles are of widespread interest due to their abundance, stability, and biocompatibility.[19] For decades, they have been applied in not only fundamental research about the magnetization mechanisms but also in a wide range of applications,[20, 21] including drug delivery systems,[22] magnetic resonance imaging,[23, 24] and hyperthermia[25, 26]. Apart from the bio-medical related applications, nanoscale iron oxide have also been incorporated in electronic devices such as the high-density data storage disks,[27] Li-ion batteries,[28] gas sensors,[29] and also solar cells[30]. Recently, magnetic nanoparticles have been reported to have a positive impact on the performance of organic electronics devices.[15, 18, 31] In practice, the magnetic properties of iron oxide nanoparticles are essential for all of the potential application, which is directly related to the crystal structures and nanoscale size.[21, 32, 33]

2.1.1 Crystal structures

The crystal structure of iron oxide nanoparticles has a strong impact on their magnetic properties as it determines the arrangement of Fe and O atoms and thus the magnetic dipoles. Depending on the arrangement of the magnetic dipoles with and without the applied magnetic field, materials can be categorized into diamagnetic, paramagnetic,

ferromagnetic, ferrimagnetic and antiferromagnetic, as indicated in Figure 2.1 from Jeong[34]. Diamagnetic and paramagnetic materials yield a weak magnetic response. Diamagnetic materials do not possess magnetic dipoles without an applied magnetic field, but they have weak induced dipoles aligned opposite to a field. Paramagnetic materials have randomly oriented magnetic dipoles which can be aligned in the same direction of the magnetic field. In contrast, long-range order of magnetic dipoles exists in ferromagnetic materials, yielding a strong magnetic moment. For ferrimagnetic materials, the long-range order strong dipoles are accompanied with adjacent weaker magnetic dipoles aligning oppositely, which also possesses strong magnetic moment. In antiferromagnetic materials, the adjacent magnetic dipoles are antiparallel in the same magnitude, so they cancel each other and thus result in a zero net magnetization. Therefore, the most useful magnetic materials are ferromagnetic and ferrimagnetic, whose basic magnetic properties are usually determined from the typical magnetization curve (magnetization (M) vs magnetic field strength (H)) as shown in Figure 2.2.[34]

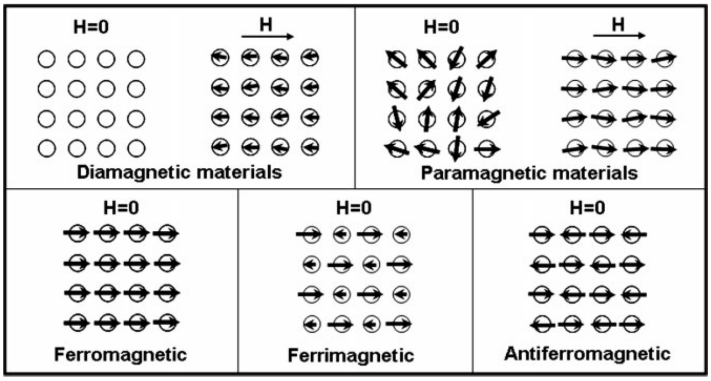

Figure 2.1: Schematic representation of the magnetic dipoles arrangements for five different categories of materials with and without applying a magnetic field(H). Apdapted with permission from [34].

There are numerous phases of iron oxide with different crystallographic structures and/or variable oxidation states of Fe ions but not all of them possesses significant magnetic property at room temperature. For iron(III) oxide, α-Fe_2O_3 with corundum structure ($R\bar{3}\bar{c}$) and the γ-Fe_2O_3 with inverse spinel structure ($Fd\bar{3}m$) exist in nature, while other polymorphs: β-Fe_2O_3 with bixbyite structure ($Ia\bar{3}$) and ϵ-Fe_2O_3 with orthorhombic structure ($Pna2_1$) are rare phases that are generally produced in the laboratory.[35, 36] The other common phase, similar to γ-Fe_2O_3, Iron(II,III) oxide

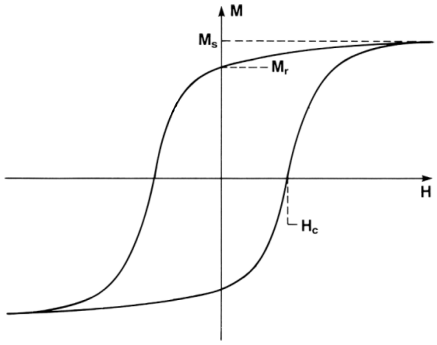

Figure 2.2: Representation of typical magnetization curve for ferromagnetic and ferrimagnetic materials. M_s: the saturation magnetization-maximum value of M; M_r: the remanence magnetization-residual magnetization at zero field strength; and H_c:the coercivity or coercive field, the applied field required to bring magnetization back to zero.

(Fe_3O_4) also possesses an inverse spinel structure,[37, 38] and could transform into γ-Fe_2O_3 at relatively low temperature under ambient condition.[39]

Figure 2.3 shows the crystallographic unit cells of different iron(III) oxides, reprinted from MacHala.[36] Among those phases at room temperature, α-Fe_2O_3 exhibits a weak ferromagnetism,[35, 36] while β-Fe_2O_3 shows paramagnetism,[40] both showing low saturation magnetization (weak magnetic response). ϵ-Fe_2O_3 have been reported displaying a large coercive field at room temperature, yet its magnetic behavior is not completely understood.[36, 41, 42] Interestingly, γ-Fe_2O_3 diplays ferrimagnetism at room temperature[35, 36, 38], exhibiting strong magentic response. Together with its prominent magnetic performance, high Curie temperature(T_C = 928 K) and remarkable chemical stability,[19] γ-Fe_2O_3 is of particular interest in practical applications.[21, 32]

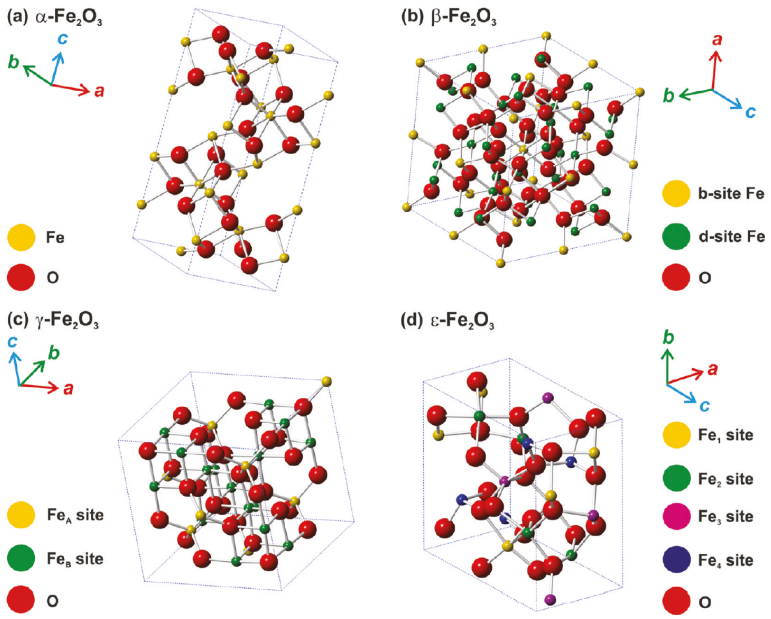

Figure 2.3: Schematic of crystallographic unit cells of several iron(III) oxides. Reproduced with permission from reference [36]. Copyright American Chemical Society.

2.1.2 Nanoscale size

Apart from crystal structure, the size of the iron oxide nanoparticles is another important factor that affect the magnetic properties. Two critical size limit, the single domain limit and the superparamagnetic limit, have been investigated extensively for magnetic nanoparticles.[32] The existence of the domain walls is governed by the competition between the magnetostatic energy(E_{MS}, E_{MS} $\sim$ Volume of the particle(V)) and the domain wall energy(E_{dw}, E_{dw} $\sim$ interface area of domains(S)). When the size decreases to a certain point, the single domain configuration is energetically favorable. This single domain limit, related to several anisotropic energy terms, normally exists in the region from several tens to hundreds of nanometers.[43]. The single domain critical diameter (D_{single}) for spherical magnetic nanoparticles could be estimated by the following equation:[32, 33]

$$D_{single} \approx 36\frac{\sqrt{AK_{eff}}}{\mu_0 M_s^2} \tag{2.1}$$

(In equation 2.1, A: exchange constant, K_{eff}: effective anisotropy constant, μ_0: vacuum permeability and M_s: saturation magnetization.) Below this limit, the nanoparticles would be magnetized in a way that all the magnetic moments of atoms are aligned in one direction.[44] According to previous report, the K_{eff} of γ-Fe_2O_3 is on the order of 4 to 8 $\times$ 10^3 J/m^3 for nanoparticles,[45, 46] being similar to that of the bulk, while the M_s of the bulk γ-Fe_2O_3 is around 350 emu/cm^3 (for volume magnitization: 1emu/cm^3 converts to 10^3 A/m).[39, 46] Additionally, the exchange constant is 10^{-11} J/m for γ-Fe_2O_3.[47] Therefore, one can estimate the lowest limit of D_{single} for spherical γ-Fe_2O_3 nanoparticles situates at around 50nm.

The alignment of single domain nanoparticles is mostly governed by the anisotropy energy (E_a), which is defined as:

$$E_a = K_{eff} V \sin^2(\theta) \tag{2.2}$$

with V and θ representing the volume of the nanoparticles and the angle between the magnetization and the easy axis (the direction when E_a is minimized).[21, 32] Magnetization reversal can only happen with magnetic moment rotation without the domain wall motion. Consequently, the single domain nanoparticles could have large coercivity (H_c) compared to the larger multidomain particles.[39, 48] With the size further decreasing, the superparamagnetic limit would be reached at a point where the thermal energy K_BT (25.7meV) overcomes E_a, causing a spontaneous magnetization reversal.[33] The relaxation time for magnetization reversal is expressed by the Neel-Brown expression as follows:[32, 33, 49]

$$\tau = \tau_0 exp(\frac{K_{eff} V}{K_B T}) \tag{2.3}$$

Where τ_0 is typically in the range between 10^{-11} and 10^{-9}s. Since the K_{eff} of γ-Fe_2O_3 is known,[45, 46] the critical diameter that causes the spontaneous magnetization reversal can be estimated to be at around 12nm. Below this limit, the τ shares the similar magnitude as τ_0, causing the high frequency magnetization reversal, which result zero net magnetization during typical measurement duration. Hence, the nanoparticles could exhibit superparamagnetic features without H_c while maintaining a decent value of M_s. However, the decrease of size also deteriorates the M_s of the nanoparticles as

the ratio of the surface atoms become prominent because of the incomplete coordinations and broken exchange bonds on the surface, which can lead to surface magnetic anisotropy, giving rise to what is known as the surface spin-canting effect.[50–53]

Overall, the magnetic properties of iron oxide nanoparticles rely heavily on the crystal structure and the size. Hence, the confirmation of the crystal structure is very important for their further usage, which will be discussed later in section 2.3. On the other hand, the size also has a large influence on the magnetic properties as described above. To control the magnetic properties, controlling the size distribution becomes essential, so it is necessary to employ methods that could synthesize nanoparticles with narrow size distribution.

2.2 Diblock copolymer reverse micelles for nanoparticles synthesis

The traditional methods to produce nanoparticles include physical milling, sputtering, and chemical reactions, which usually require an additional process to avoid the aggregation of the particles and also possess low controllability of the size or shape.[21, 54] To tackle this problem, one of the recent advancement is employing diblock copolymers self-assembly templates which offers rigid space confinement.[55] Particularly, diblock copolymers micelles have been used to produce nanoparticles since the late 1990s.[56–58] Those diblock copolymers usually consist of two chemically different blocks with one non-polar (hydrophobic) and another polar (hydrophilic). With selective non-polar solvents, the diblock copolymers could form reverse micelles with the core of polar blocks surrounded by the corona of non-polar blocks.[56] The internal structures related to the size of core and corona for micelles of several diblock copolymers were well characterized by dynamic light scattering[59] and small angle neutron scattering,[60] showing a narrow size distribution nature. By incorporating the proper metal precursors which are usually polar in nature and thus have the affinity to combine with the polar core, different types of diblock copolymer reverse micelles have been adopted to produce different nanoparticles including metals, metals oxides and metal alloys.[55, 61, 62]

Among the various types of diblock copolymer, the polystyrene-*b*-poly(vinyl pyridine)(PS-*b*-PVP) families, including polystyrene-*b*-poly(4 vinyl pyridine)(PS-*b*-P4VP) and polystyrene-*b*-poly(2 vinyl pyridine)(PS-*b*-P2VP), are frequently used in the fabrication of nanoparticles. The early classical example was to employ PS-*b*-P4VP in the production of Au nanoparticles by incorporating $HAuCl_4$ which protonated and attached to the vinyl pyridine micellar core via electrostatic interaction.[63] In addition to the noble metal nanoparticles, recently, several magnetic nanoparticles (Pt, Co, Fe) and bimetallic nanoparticles (FePt, CoPt) array were also produced using either PS-*b*-P4VP or PS-*b*-P2VP.[62] In these systems, the PS-*b*-P2VP or PS-*b*-P4VP were usually dissolved in toluene, a selective non-polar solvent for the PS block, to form the reverse micelles with non-polar PS corona and polar PVP core. The proper precursor salts were then added and infiltrated inside the polar core, driven by the solubility difference or specific interactions.[56] After that, the precursor loaded micelles could be applied to coat the surface typically by spin-coating or dip-coating. By performing plasma treatment, the polymeric micelles layers would vanish and expose the corresponding nanoparticles. This strategy greatly facilitates the surface modification without the use of wet chemical etchant. The following schematic Figure 2.4[64] summarizes of the above procedure.

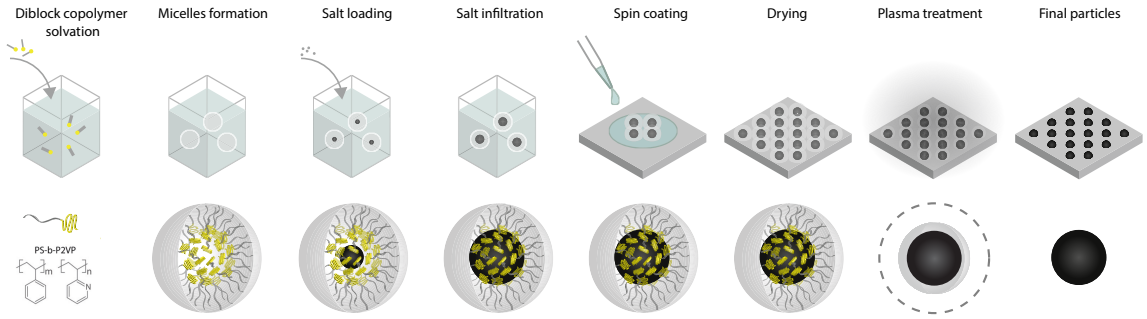

Figure 2.4: Schematic of nanoparticles synthesis using polystyrene-*b*-poly(2 vinyl pyridine) diblock copolymer reverse micelles. Adapted with permission from reference [64].

One of the significant advantages of this approach is that the resultant nanoparticle arrays adapts similar dispersion to that of the loaded micelles, offering excellent flexibility in tuning the spacing and arrangement of these nanoparticles. For example,

the quasi-hexagonal two-dimensional array of Au nanoparticles was generated using $HAuCl_4$ \ PS-*b*-P2VP by dip-coating and oxygen plasma treatment.[57] In this case, the interparticle distance changes with the varying molecular weight of PS or P2VP. The use of different non-polar solvents and concentrations of the diblock copolymer also affected the dispersion of the PS-*b*-P2VP reverse micelles as reported by Krishnamoorthy.[65] The above ideas, can be summarized using the Figure 2.5 from the recent study.[1] In addition, the spin-coating speeds were also reported to change the micelles dispersion.[65, 66] The detail examination of the dispersion of the micelles will be discussed in Chapter 6.

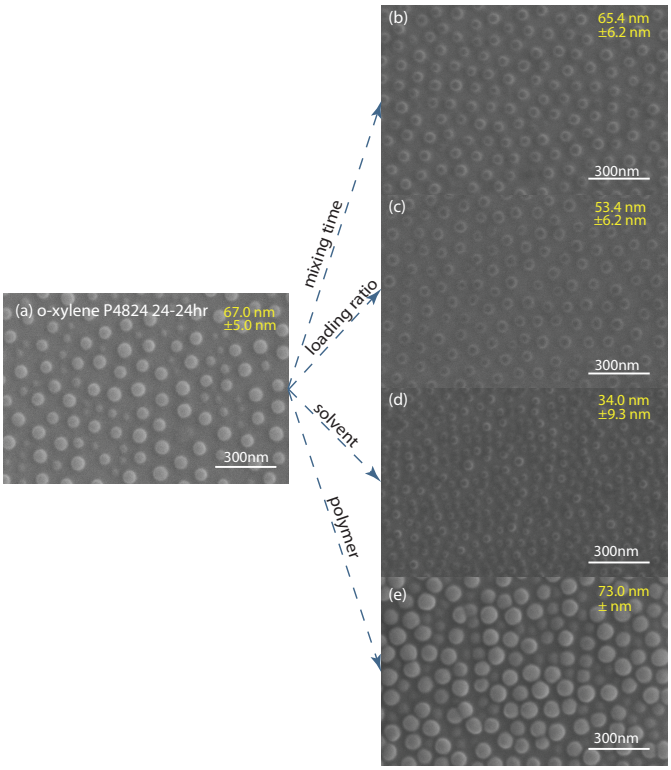

Figure 2.5: Different ways to modify dispersion of PS-*b*-P2VP reverse micelles.

Another advantage of this method is the size tunability of the resulted nanoparticles. By simply changing the amount of precursor loading or the block length of PS

[1]Figure adapt from the paper in preparation, "Synthesizing Monodispersed Methylammonium Lead Iodide Perovskite Nanoparticles by Reverse Micelles Templating, L. S. Hui, C. Beswick, A. W. Getachew, H. Heibrunner, K. Liang, G, Hanta, H. Dawood, M. Scharber, N. Isik, R. LaPierre, N. S. Sariciftci, and A. Turak"

and P2VP, different size of different types of nanoparticles, including magnetic metal nanoparticles, were generated successfully.[57, 62, 67] These convenient ways to alter the dispersion and size could change the properties of the nanoparticles and thus have different impacts on the surface modification.

2.2.1 PS-*b*-P2VP reverse micelles formation and several related parameters

Typically, PS-*b*-P2VP reverse micelles are formed in the selective solvent for the non-polar polystyrene (PS) blocks, when the concentration of the PS-*b*-P2VP is above the critical micelles concentration (cmc). Toluene is typically used as a solvent for PS-*b*-P2VP to form the reverse micelles.[56, 58, 59] The cmc for the PS-*b*-P2VP (300 styrene units in PS block and 300 2-vinyl pyridine units in P2VP block) was found to be at around 0.1mg/ml.[58] During the micelles formation, the non-polar polystyrene(PS) blocks align toward the polymer-solvent interfaces to form the corona as PS is highly soluble in toluene (a non-polar solvent), while the polar poly(2-vinyl pyridine)(P2VP) blocks concentrate inside to form the core, driven by lowering the free energy of the system. Figure 2.6 shows the schematic for PS-*b*-P2VP reverse micelles formation.

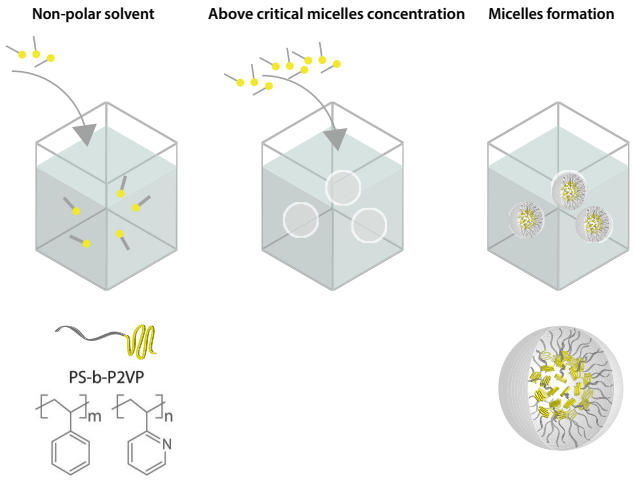

Figure 2.6: Schematic for PS-*b*-P2VP reverse micelles formation.

In addition, the size of the micelles should remain unchanged for concentrations between 1mg/ml to 5mg/ml.[58]. The size of the micelles is closely related to the

aggregation number (the total number of diblock copolymer molecule in single micelles) which can be changed with the block length of PS or P2VP.[59] Therefore, different size of micelles can be obtained by varying the molecular weight in PS or P2VP block of PS-*b*-P2VP. Moreover, using different solvent also appears to have a large impact on the reverse micelles, as it directly interacts with the PS block of PS-*b*-P2VP.[65] Therefore, many parameters can be changed to manipulate the PS-*b*-P2VP reverse micelles. Some of them will be presented in Chapter 6.

2.2.2 Using PS-*b*-P2VP reverse micelles for iron oxide nanoparticles production

An iron salt, $FeCl_3$, was recently found to be a suitable precursor for loading PS-*b*-P2VP reverse micelles.[52, 67, 68] Similar to the procedure described in Figure 2.4, oxygen plasma was employed for the purpose of removing the carbon-based micelles and oxidizing the $FeCl_3$, together by an annealing process (600°C in vacuum for 2h) to increase the crystallinity of the nanoparticles.[52] Yet, there is no detailed investigation of the $FeCl_3$ loading and iron oxide formation in these reverse micelles processes nor the crystal structure of the related iron oxide nanoparticles. In order to apply the iron oxides nanoparticles into the actual OPV or OLED devices to explore the magnetic effects as described in the introduction, it is necessary to determine the exact iron oxide formation processes and their crystal structures during the typical reverse micelles process. The above issues will be elaborated in Chapter 4 in the thesis.

In addition, $FeCl_3$ was found to coordinate with the lone pair electrons on nitrogen atoms of vinyl pyridine unit in neat PS-*b*-P2VP.[69] Since PS-*b*-P2VP reverse micelles have limited amount of the vinyl pyridine unit, there could be a saturation loading of $FeCl_3$ due to the steric configuration and the available nitrogen atoms in the P2VP core. Over-loading of $FeCl_3$ into PS-*b*-P2VP reverse micelles has been observed, leading to poor quality nanoparticles.[68] It is thus important to investigate the saturation limit of $FeCl_3$ in PS-*b*-P2VP reverse micelles to fully take advantage of reverse micelles method for size and dispersion control. By using quantum mechanical mapping in atomic force microscopy, this saturation limit is elucidated in this thesis(See 6.5 for detail).

2.3 Different techniques for characterizing iron oxide nanoparticles

The properties of the iron oxide nanoparticles require a variety of characterization techniques, especially for the limited amount and size of the nanoparticles from reverse micelles synthesis and the diversity of crystal structures.

To determine crystal structures, X-ray diffraction(XRD) is commonly used to characterize different iron oxides. Yet it requires a relatively large amount of material (normally large powders or thick films) to yield decent data output, which is not compatible with the small amount of materials from reverse micelles synthesis. In addition, XRD is not adequate to distinguish two important magnetic iron oxides: γ-Fe_2O_3 and Fe_3O_4 due to their similar crystal structure, as this technique is based on the constructive interference of X-rays or electron from the crystal structure of samples.[70, 71] Therefore other methods need to be applied in order to distinguish between γ-Fe_2O_3 and Fe_3O_4.

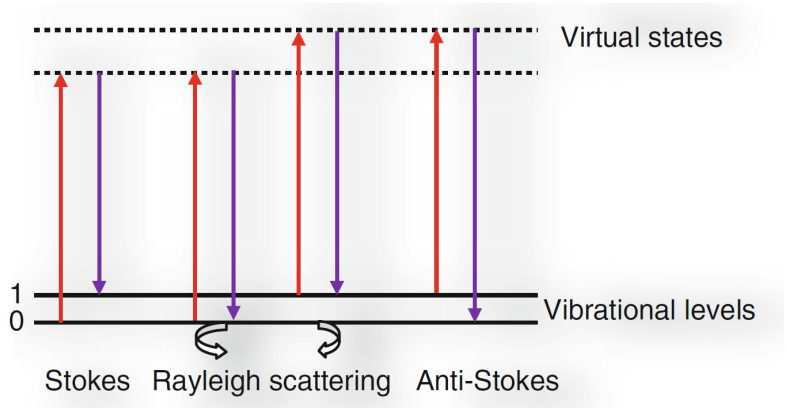

Figure 2.7: Illustration of Raman scattering processes. Adapted with permission from reference [72].

Raman spectroscopy appears to be a versatile technique for characterizing iron oxides, since different phases exhibit distinctive Raman peaks.[72–76] The spectrum is

a result of Raman scattering radiation, an inelastic scattering process of photons with phonons, providing detailed information of the material based on the vibrational modes of the phonons, as indicated in Figure 2.7 from Soler.[72] The Raman spectra originate from the Stokes and anti-Stokes components in the dipole moment, from which the polarizability can be expanded as a linear function of the oscillation frequency and its availability is governed by the selection rules [77]. As an incident photon interacts with a molecule, it induces a dipole moment P to the electron cloud. The Raman spectrum can be induced by the frequency shift from the incident frequency (μ_0)of the photon as a result of the vibrational frequency of the molecule (μ_m). It is therefore, capable of revealing the material properties, such as the atomic bonds, vibrational states, crystallinity and strain. Groups have reported the iron oxides vibrational modes calculated by the density function theory (DFT) and group theory simulations [72, 74]. In addition, Raman spectroscopy has been used to investigate PS-*b*-P2VP[78, 79] and $FeCl_3$.[80–82] Importantly, PS-*b*-P2VP, iron oxides, and $FeCl_3$ characteristic vibrational modes corresponds to the Raman shift at different wavenumbers with respect to each other, which greatly facilitate the spectra interpretation. Hence, Raman spectroscopy is an excellent candidate for studying the evolution of the iron oxide nanoparticles from the very beginning of the synthesis process using PS-*b*-P2VP and $FeCl_3$ (See Chapter 4).

To investigate the individual iron oxide nanoparticles directly, it is necessary to apply other techniques with the ability to acquire information from nanometer scale. For instance, atomic force microscopy (AFM) is used to measure the morphology of nano-sized objects, especially for the micelles and nanoparticles arrays in flat surfaces,[83–85] with the high accuracy in height (z) direction. Yet, there is a limitation to acquire the morphology of a large area with AFM due to its relatively slow scanning speed. Another frequently-used method to obtain the morphology in nanometer scale is scanning electron microscopy (SEM) which offers real-time imaging with wide range magnification.[86, 87] Figure 2.8 shows the schematic of electron beam-sample interaction in electron microscopy. For SEM, secondary electrons (SE) are typically collected to acquire the topographic information. In addition, transmission electron microscopy (TEM) equipped with energy-dispersive X-ray spectroscopy(EDX) or electron energy loss spectroscopy (EELS) has been proved to be particularly helpful in characterizing nanoparticles, offering an effective way to reveal the crystal structure and the composition of the single nanoparticles.[39, 88, 89] In TEM, the elastically scattered electrons

are collected for electron diffraction, while the inelastically scattered electrons yield EELS spectra. In addition, the characteristic X-rays are detected to obtain EDX spectra.

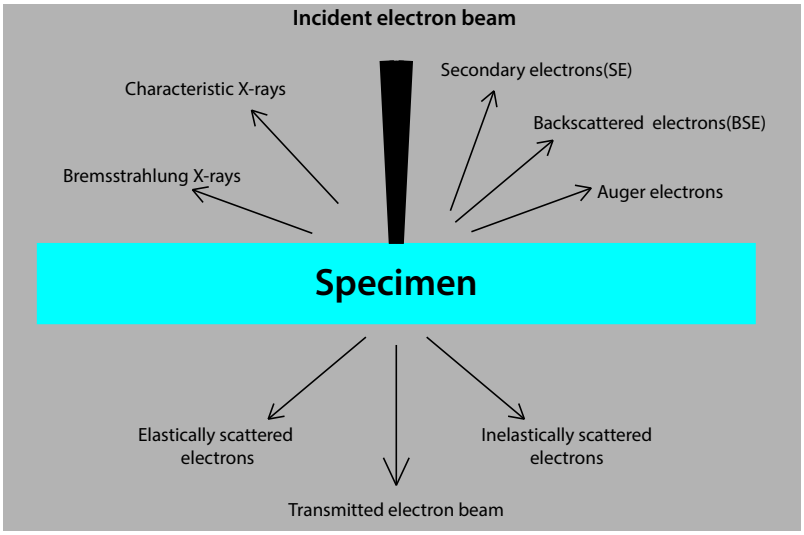

Figure 2.8: Schematic illustration of electron beam-sample interaction.

In terms of measuring the magnetic properties of the nanoparticles, superconducting quantum interference device magnetometer (SQUID) is usually applied especially for the small amount of material such as a thin layer of nanoparticles[62, 90, 91], thin films[92, 93] and etc. Figure 2.9 shows the typical structure of the SQUID magnetometer. The detection circuit has two opposed Helmholtz detection coils and the SQUID input coil connected in series. The current that flows in response to a change in flux is given by:

$$\Delta I = \frac{\Delta \Phi}{L} \tag{2.4}$$

, where ΔI is the induced current due to the flux change $\Delta\Phi$, and L is the circuit's inductance. During measurement, the sample is vibrated between the two counter-wound detection coils. When the sample passes through a coil, it results in the change of flux in that coil by the amount proportional to the magnetic moment (M) of the sample. SQUID magnetometer can measure extremely small variations in magnetic flux, having sensitivities on the order of 10^{-8} emu.[94]

Applying various types of characterization techniques, it is possible to gain a better

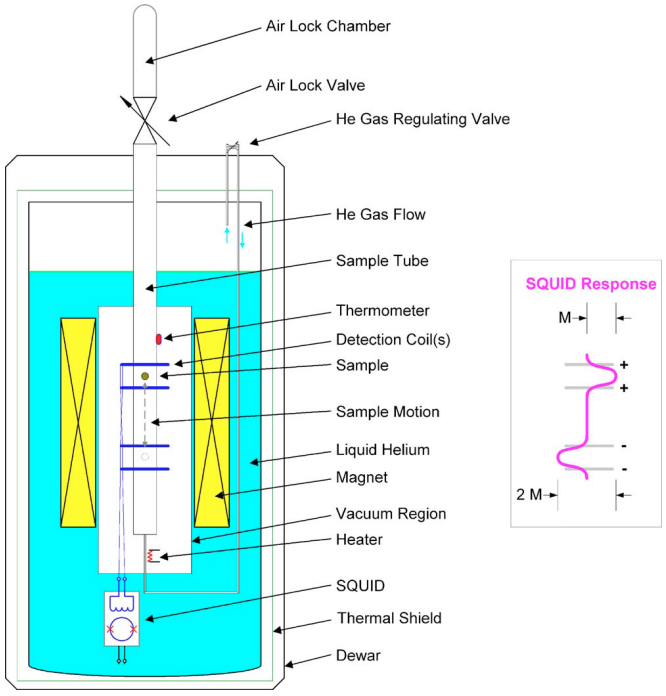

Figure 2.9: Schematic representation of SQUID magnetometer. The figure on the right represents a response of the detection coils as a function of sample position height. Reproduced from reference [94].

understanding of the morphology, crystal structure and magnetic properties of the iron oxide nanoparticles.

2.4 Magnetic effect on organic semiconductor

The excited states (excitons) are responsible for electronic processes in organic semiconductor. Due to the spin configuration of electron-hole pairs that form the excitons, the excited states are divided into singlet and triplet states with the statistical ratio of 1 to 3. In these excited states, the long-range Coulombic attraction determines the binding energy in excitons, while the short-range spin-spin interaction yields the energy difference between singlet and triplet states.[14, 95] The conversion between singlet and triplet excitons can be achieved by a spin flipping mechanism from hyperfine interaction or spin-orbital coupling.[14, 96] It has been found that magnetic field can affect the spin dependent pairing of electrons and holes during the exciton pair formation or

change the interconversions between singlet and triplet excited states.[14] Therefore, the singlet to triplet ratios can be altered. Since singlet and triplet excited states have different impact on the related electronic processes such as dissociation and decay of the excited states, magnetic field have a potential to influence the photocurrent and electroluminescence of organic semiconductors and thus the related devices.

2.4.1 Incorporation of magnetic materials onto OPV and OLED devices

Recently, Wu[16] reported that applying isolated Co magnetic nanoparticles onto the anode of OLEDs resulted in the enhancement of electroluminescence under a small magnetic field. They proposed the spin-polarized hole injection from the Co magnetic nanoparticles, which increase the singlet ratio in the OLED, leading to an improvement in electroluminescence. Similar effect was found by applying a thin layer on the anode,[18] where the current efficiency (cd/A) was improved by 10.5% with optimum thickness under 1500Oe applied field. Additionally, magnetic iron oxides have been applied to modify the anode of the OPV, leading to smoother contact, better transparency and higher conducitivity of the anode, which improves the power efficiency of OPVs.[15] However, the magnetic effect was not addressed in the same study. Recently, magnetic fields showed positive impact on poly[4,4-bis(2-ethylhexyl)-cyclopenta-(2,1-b;3,4-b)dithiophen]-2,6-diyl-alt-(2,1,3- benzo-thiadiazole)24,7-diyl (PCPDTBT) which is intensively used in bulk heterojunction solar cells, by affecting the current through the PCPDTBT-based diode.[97] Overall, to investigate how the magnetic nanoparticles could affect OPV and OLED is essential for their further development.

Chapter 3

Overall experimental

3.1 Materials

Polystyrene-block-poly(2-vinyl pyridine)(PS-*b*-P2VP, M_n: 48500-*b*-70000)–P1330, polystyrene-block-poly(2-vinyl pyridine) (PS-*b*-P2VP, M_n: 75000-*b*-66500)–P4824 and homopolymer poly(2-vinyl pyridine) (M_n: 77000)–HP2VP were purchased from Polymer Source Inc. The Iron(III) chloride($FeCl_3$, sublimed grade, $\geqslant$ 99.9%) and Iodine(ACS reagent, $\geqslant$ 99.8%) were purchased from Sigma-Aldrich for loading and staining the micelles respectively.

For solvents, toluene(HPLC grade, $\geqslant$ 99.8%), hexanes(HPLC grade), tetrahydrofuran(reagent grade), acetone(reagent grade) and 2-propanol(reagent grade) were purchased from Caledon Laboratories Ltd. In addition, ethanol(95%vol) was bought from Commercial Alcohols and o-xylene(reagent grade, $\geqslant$ 98.0%) was bought from Sigma-Aldrich. All the solvents were used as received.

In terms of organic solar cells fabrication, the poly(2,3-dihydrothieno-1,4-dioxin)-poly(styrene sulfonate)(PEDOT:PSS) was acquired from Ossila while the poly(3-hexylthiophene-2,5-diyl)(P3HT) and [6,6]-phenyl-C_{61}-butyric acid methyl ester(PCBM) were obtained from Luminescence Technology Corp. The chlorobenzene($\geqslant$ 99.5%) for dissolving the P3HT and PCBM was purchased from VWR International.

3.2 Synthesis of iron oxide nanoparticles

3.2.1 PS-*b*-P2VP fritting

The Polystyrene-block-poly(2-vinyl pyridine)(PS-*b*-P2VP, M_n: 48500-*b*-70000)–P1330 and poly-styrene-block-poly(2-vinyl pyridine) (PS-*b*-P2VP, M_n: 75000-*b*-66500)–P4824 were fritted to exclude the impurities. The PS-*b*-P2VP powders were added to a clean vial and then tetrahydrofuran(around 10ml) was introduced to dissolve the PS-*b*-P2VP. Ultrasonication was applied to speed up the dissolving process. The resulted solution was filtered by glass pipette filled with glass wool and then dropped into a beaker with 250ml hexane. The precipitates of the PS-*b*-P2VP were suspended in a large amount of hexane(nonsolvent for PS-*b*-P2VP) under 350rpm stirring. To collect the precipitates, the above mixture was filtered through a fine pore size filter funnel under the aid of a vacuum pump. The precipitates were dried overnight under ambient environment before collecting for further usage.

3.2.2 PS-*b*-P2VP reverse micelles formation and iron precursor loading

To prepare a typical PS-*b*-P2VP reverse micelles solution, the fritted PS-*b*-P2VP powders(either P1330 or P4824)were dissolved in o-xylene(or toluene) to yield the 3mg/ml solution which was above the critical micelle concentration.[58, 98] The non-polar polystyrene(PS) blocks align toward the polymer-solvent interfaces to form the corona of reverse micelles as PS is highly soluble in o-xylene or toluene(both non-polar solvent, while the polar poly(2-vinyl pyridine)(P2VP) blocks concentrate inside to form the core. The solutions were kept under magnetic stirring for at least 24h before iron precursor loading.

The loading of the iron precursor into the reverse micelles was done by adding a certain amount of $FeCl_3$ into the reverse micelles solution. Here, the loading ratio was defined as the ratio between the amount of Fe^{3+} and the total amount of 2-vinyl pyridine(2VP) units of the PS-*b*-P2VP(unit in mole). After adding the $FeCl_3$, the solutions were kept under magnetic stirring for 24h to allow adequate loading(i.e. $FeCl_3$

infiltrated into the reverse micelles core). Details about different loading ratios will be described in the corresponding sections.

The detailed procedures for the homopolymer poly(2-vinyl pyridine) assisted loading can be seen in the experimental section in Chapter 6.

3.2.3 Oxygen plasma treatment of the loaded micelles

To produce the iron oxide nanoparticles, the above $FeCl_3$ loaded reverse micelles solution was typically spin coated onto a clean silicon substrate. Oxygen plasma treatment was employed to convert the $FeCl_3$ precursor into iron oxide and remove the carbon-based micelles. Details about oxygen plasma treatment parameters will be described in section 3.3.3.

3.3 Other processes

3.3.1 Substrates and vials cleaning

The substrates(including Si, smooth ITO/glass, patterned ITO/glass) and vials were immersed in a clean beaker with acetone for a 15 minutes ultrasonic bath treatment(ultrasonic cleaner,VGT-1620QTD) and subsequently with 2-propanol for another 15 mintues ultrasonic bath treatment. A N_2 gun was used to dry the substrates and vials after solvents cleaning.

3.3.2 Spin coating

The spin coating processes were performed on a spin coater outside the glovebox (Laurell Technologies, WS-650MZ-23NPP) or a spin coater inside the glovebox (Specialty Coating Inc, G3P). The micelles solutions were transferred by a mechanical pipette for spin coating. To generate a single layer of micelles on substrates, the standard procedures were using 4μl of the micelles solution for single dynamic spin coating with 2000rpm spin speed. The spin coating time was set to 45s. The effect of other spin

speeds will be described in Chapter 6.

3.3.3 Oxygen plasma treatment

The oxygen plasma treatments were conducted in a Harrick Plasma cleaner (PDC-001-HP) for iron oxide nanoparticles formation and polymeric micelles removal. The power of the plasma cleaner was adjusted to 29.6W(Med) with 30 sccm O_2 gas flow rate, corresponding to around 950mtorr in the plasma chamber. The typical plasma treatment duration was 25 minutes for one substrate coated with a monolayer of micelles.

3.3.4 Annealing

Annealing of the iron oxide nanoparticles was carried out in a Lindberg tube furnace where the nanoparticles coated substrates were kept on top of an alumina boat sitting in the middle of the furnace tube. The tube having glass caps of both ends enables annealing under different gas environments (typically N_2 in our case). The typical annealing condition was 600°C for 2h under N_2 environment, which was confirmed to increase the crystallinity of the nanoparticles with γ phase crystal structure(See Chapter 4 for detial). Other annealing conditions will be described in the Chapter 5.

3.4 Characterization techniques

3.4.1 Raman spectroscopy

Raman spectroscopy was performed by a Renishaw inVia spectrometer at 514nm laser excitation. The laser power was set to 10mW and an objective of 20x and 1800 l per mm grating was used. The baseline of spectra was created and then subtracted to highlight the peaks of interest. In addition, the spectra were smoothed by Savitzky-Golay function in Origin. After that, the full spectra, which corresponded to the Raman shift from 150cm^{-1} to 2000cm^{-1}, were normalized into the value between 0 to 1 to facilitate the comparison. Moreover, to highlight the iron oxide characteristic peaks, the portion

from the Raman shift between 150cm^{-1} and 900cm^{-1} was normalized between 0 and 1. The processed spectra from 150cm^{-1} to 900cm^{-1} were further deconvoluted using Lorentzian line shape profiles for comparison.

3.4.2 Atomic force microscopy

The substrates for atomic force microscopy(AFM) characterization were silicon(thickness: 500um, orientation: <100>, University Wafer.) or smooth ITO thin film on glass. AFM images were collected by an Asylum MFP-3D instrument(Oxford Instruments Asylum Research Inc.) in the alternating current mode under ambient environment. AFM probes(Oxford Instruments Asylum Research Inc.) with spring constant of 26N/m and resonant frequency at 300kHz were applied in tapping mode for topography scan. WSxM was used to process the AFM raw data.[99]

3.4.3 Scanning electron microscopy

The substrates for scanning electron microscopy(SEM) characterization were P-doped silicon wafers(thickness: 380um, orientation: <100>, resistivity: 0.001-0.005ohm·cm, University Wafer.) which were conductive enough to allow the direct SEM imaging of micelles/nanoparticles without coating. The micelles/nanoparticles coated substrates were mounted by carbon tape and nickel paste on 25.4mm standard Al stubs. The SEM characterizations were conducted in FEI Versa 3D SEM with a Schottky thermal field emitter electron gun. The accelerating voltage and probe current were normally adjusted to 5kV and 12pA to minimize the charging effect, which still maintained good signal-to-noise ratio for high-quality imaging.

3.4.4 Transmission electron microscopy

The silicon nitride membranes window grids ($0.1 \times 0.1mm$, 3×3 array, 10nm thick, Norcada Inc) were used for transmission electron microscopy (TEM) characterization. This type of girds can withstand our routine oxygen plasma treatment and annealing (up to 600°C) condition. The samples were spin coated on the grids with the help of

a customized grid holder, which allow the direct observation of single nanoparticles. The TEM (JEOL 2010F) imaging was operated at 200kV with the field emission gun (FEG) source. The selected area electron diffraction (SAED) was carried out using a 1.2um aperture for studying the crystal structure. In addition, energy-dispersive X-ray spectroscopy (EDX) and electron energy loss spectroscopy (EELS) were performed for acquiring the compositional information in the scanning transmission electron microscopy(STEM) mode under the same TEM. The TEM, SAED, and EELS data were processed by Gatan Microscopy Suite 3 software and the EDX data was processed by INCA Microscopy Suite.

3.4.5 Superconducting quantum interference device magnetometer

The magnetic properties of the nanoparticles were measured by a liquid Helium cooled superconducting quantum interference device magnetometer (SQUID)(Quantum Design, Inc.). The measurements of the samples were performed at 300K with an applied magnetic field between -20000Oe and 20000Oe. Data points were collected by each 100Oe increment from -5000Oe to 5000Oe and each 1000Oe increment for the rest of the range.

3.4.6 IV measurement

The I-V testings were carried out using a Xtralien X-100 source measure unit in combination with a push-fit test board from Ossila, using the I-V measurement Python script. The equipment included a Ossila push fit test board, a Xtralien X-100 source measure unit, a source measure unit AC adapter, a BNC Cable, and a USB cable. The Ossila push fit test board was attached to the Xtralien X-100 source measure unit via channel 1 by a BNC cable, while the source measure unit was connected to a power supply by the AC adapter and to the computer by the USB cable. The I-V sweeping range and interval will be described in the corresponding device I-V testing section later.

3.5 Organic solar cells fabrication

The diodes and organic solar cells were fabricated using 6 pixels ITO/glass substrates and encapsulating glass coverslip from Ossila. The cleaning was conducted by the same procedures in section 3.3.1.

The structure of the organic solar cells was ITO/PEDOT:PSS/P3HT:PCBM/Al. The PEDOT:PSS layers were spun at 6000rpm for 30s using 30μl volume. A cotton swab dipped in DI water was then applied to wipe the cathode strip and anode strips along the sides of the substrates. After that, the substrates were annealed on a hotplate at 150°C for 5min. Subsequently, 20μl of P3HT:PCBM solutions were used to spin coat on PEDOT:PSS layer using 2000rpm for 15s. Here, the P3HT and PCBM were dissolved in Chlorobenzene in a mass ratio of 1:0.6, yielding a concentration of 25mg/ml. After P3HT:PCBM spin coating, the cathode strip and anode strips were cleaned with a cotton swab dipped in chlorobenzene. The substrates were annealed at 100°C for 5min after spin coating of P3HT:PCBM. Finally, the Al layer was deposited using physical vapor deposition(PVD) under high vacuum(2×10^{-7} mbar) with great control over its thickness which is around 50nm. The encapsulation was done by applying a UV-curable epoxy in conjunction with a glass coverslip under UV light for 1min.

Chapter 4

Evolution of iron oxide nanoparticles from the reverse micelles method tracked by Raman spectroscopy

[1]

4.1 Experimental

The $FeCl_3$ loaded micelles and iron oxide nanoparticles were synthesized following the procedures as described in section 3.2 and 3.3 in Chapter 3.The polystyrene-block-poly(2-vinyl pyridine)(PS-*b*-P2VP, M_n: 75000-*b*-66500, labeled as P4824) was used in this experiment.

For the Raman characterization, all the samples were fabricated by drop-casting (2ul for 2 times) the loaded P4824 micelles using o-xylene as solvent on freshly cleaved KBr substrates to get enough materials for spectra acquisition, as the spin coated sample could not yield a sufficient Raman signal in the system. In addition, the loading ratio (the number of the Fe^{3+} ion divided by the number of the 2VP units

[1] "Chapter submitted for publication with some modifications as K. lIANG, L.S. Hui, A. Turak, Evolution of iron oxide nanoparticles by the reverse micelle method, J. Mater. Chem. C"

in PS-*b*-P2VP) was set to 1.5 in this study. Following the synthesis processes in chapter 3, coated KBr substrate was treated with 25 mins oxygen plasma before annealing. The same substrate was then annealed at 600°C in N_2 for 2h for phase identification of iron oxide nanoparticles. Extra annealing was carried out at the same condition (600°C in N_2 for 2h) to investigate the phase transformation of the iron oxide nanoparticles. Raman spectra of the sample at each stages were collected. As a reference, the Raman spectrum of drop-casted empty P4824 micelles was also collected for comparison. Finally, the poly(2-vinyl pyridine) homopolymer(HP2VP, M_n: 77000g/mol) was used to study the interaction between $FeCl_3$ and poly(2-vinyl pyridine). In this case, 6mg of HP2VP was added to 1ml o-xylene with $FeCl_3$ to yield a 0.3 loading ratio mixture and then kept stirring for at least 24h before drop-casting on a freshly cleaved KBr substrate. In order to generate adequate signals for the spectra acquisition, the laser was focused at regions with high concentration of materials, which is on the "coffee stain" area as the drop-casted sample solution dried off.

4.2 Evolution of iron oxide nanoparticles in the reverse micelles syntheses

Raman spectroscopy has been used to identify the phases of iron oxide thin films[100], particle aggregations[39] and bulk solids[101], as each phase of iron oxide has unique Raman active phonons corresponding to different Raman shifts.[72, 74–76, 102] It provides a convenient way to differentiate the exact phase. In particular, owing to the similar crystal structure and magnetic property, the phase identification between γ-Fe_2O_3 and Fe_3O_4 cannot be confirmed with the conventional X-ray\electron diffraction techniques or magnetometer measurement (See section 2.1 and 2.3 for detail). Therefore Raman spectroscopy was employed to confirm the exact form of the iron oxide nanoparticles. In fact, the Raman shifts for the Raman active phonons of $FeCl_3$ and PS-*b*-P2VP are also distinguishable from that of iron oxides. Consequently, Raman spectroscopy was also performed to monitor the processes at each stage, to investigate the evolution of iron oxide nanoparticles throughout the synthesis process. Table 4.1 summarized the characteristic peaks position for several phases of iron oxide, $FeCl_3$ (the iron precursor salt) and PS-*b*-P2VP. For Raman sample preparation, KBr

substrates were employed as its Raman features did not interfere the features of the materials in this study.

Table 4.1: Table of the observed Raman peaks for PS-*b*-P2VP, $FeCl_3$ and several phases of iron oxide

PS-*b*-P2VP[78, 79]	$FeCl_3$[80–82, 103]	α-Fe_2O_3[73]	γ-Fe_2O_3[100]	Fe_3O_4[104]
		225		
		247		
	282	293		
				301
	330*			
			365	
		412		
		498	511	
				533
		613		
				663
			700	
1005(s)				
1064(m)				
1583(m)				
1602(m)				

*hydrated $[FeCl_4]^-$

s = strong, m = medium, w = weak.

The Raman spectra from each step of the processes can be seen in Figure 4.1 from (a) to (f). Starting from the spectrum of P4824 empty micelles in Figure 4.1 (a), only two peaks at 1000cm^{-1} and 1591cm^{-1} were visible, which can be assigned to $\nu(1)$ symmetric ring breathing mode and $\nu(8b)$ ring stretching mode of 2-vinyl pyridine(2VP).[78, 79] After the loading of the $FeCl_3$(See Figure 4.1 (c)), a new peak appears at 294cm^{-1}, which could be related to $FeCl_3$ A_{1g} mode.[82, 103] Although the expected A_{1g} mode of a pristine $FeCl_3$ should be at 282cm^{-1}[103], the upshift was likely due to the configuration change as the $FeCl_3$ coordinated with 2VP.[69] Similar behaviour was observed when $FeCl_3$ was intercalated with graphite.[82, 103] Additionaly, new peaks emerged at 1160cm^{-1}, 1306cm^{-1}, 1446cm^{-1} which was not obsered in the empty micelles. The activation of those peaks probably arose from the $FeCl_3$-2VP interaction.[69] In fact, the Raman signal of the micelles was highly diminished due to the transparency in visible range of both the sample layer and the KBr substrate. While only a portion of incident laser intensity is reflected and scattered back to the detector, most of the incident laser is transmitted through the substrate, resulting

in a low count of detected Raman scattering signals. In fact, these polymer peaks would normally be quite visible under normal circumstances on reflective or even with opaque substrates. On the other hand, after the KBr substrate was drop-casted with the $FeCl_3$ loaded micelles, the incident laser light instead of being transmitted through the substrate was more diffuse scattered by the brownish loaded micelle layer and the resulted counts of Raman signals was much higher. To optimize the measurement, the Raman signals were specifically collected from "coffee stain" regions where it has high concentrations of materials, as a result of the drop-casting process.

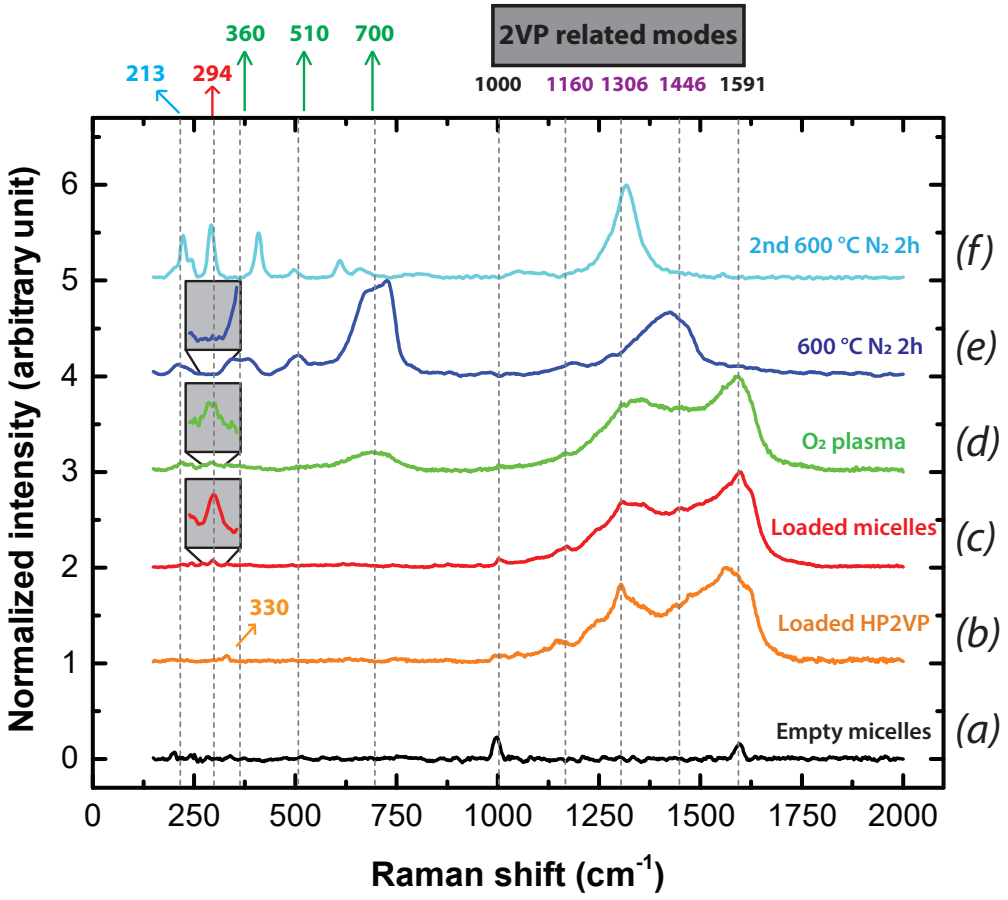

Figure 4.1: The Raman spectra of the evolution of the iron oxide nanoparticles synthesized by the reverse micelles method. Note that magnified insets above spectra (c)Loaded micelles (red line), (d)O_2 plasma (green line), and (e)600 °C N_2 (navy blue line) are amplified 5 times in the 270 to 320cm^{-1} region to highlight the $FeCl_3$-P2VP complex peak.

For comparison, $FeCl_3$ was mixed with HP2VP mixture in o-xylene(See Figure 4.1 (b) for the corresponding Raman spectrum). The peaks above 1000cm^{-1} were very similar to that of the loaded micelles, reinforcing that the new peaks could be attributed to the interaction between $FeCl_3$ and 2VP. The new peak at 330cm^{-1} from the $FeCl_3$ and HP2VP mixture solution can be assigned to the hydrated $FeCl_3$-P2VP complex A_1 mode[80, 81] due to hygroscopic nature of the $FeCl_3$ and the affinity of Fe ion with the VP group as proven by the presence of the 1306cm^{-1} $FeCl_3$-P2VP complex mode in the spectrum. Micelles normally provides a shielding environment for salts infiltrated inside, but the absence of micelles in this $FeCl_3$-HP2VP solution allows moisture in environment to combine with the $FeCl_3$ salts which is highly hygroscopic. All the above peaks and their assignments can be seen in table 4.2

The spectrum of loaded micelles after 25mins O_2 plasma treatment is shown in Figure 4.1 (d). A broad peak occurred at around 700cm^{-1}, which could be assigned to the A_{1g} mode of γ-Fe_2O_3, was evidence of iron oxide formation after plasma treatment (Further confirmation can be seen in section 5.2.1) This was further supported by the apperance of a new peak at 213cm^{-1} which could be attributed to A_{1g} mode of the laser induced α-Fe_2O_3 due to local heating[73, 105], as Chourpa[101] found that using laser power higher than 1.6mW could lead to instantaneous formation of α-Fe_2O_3 and downshift of the Raman peaks. However, the peaks above 1000cm^{-1} and at 294cm^{-1} persisted without significant change of intensity, suggesting that the majority of the loaded micelles were unaffected by O_2 plasma. One possible explanation is that only the surface region were affected by the 25mins O_2 plasma treatment due to the thick layer of loaded micelles from drop-casting.(25mins O_2 plasma treatment is sufficient to remove all the carbon-based micelles and convert the $FeCl_3$ to iron oxide in the monolayer case. See Chapter 5 and refchapterdispersion for detail.)

In order to promote the formation of γ-Fe2O3, the O_2 plasma treated sample was annealed at 600°C in N_2 for 2h(Raman spectrum in Figure 4.1 (e)). The 2VP related peaks above 1000cm^{-1} disappeared while the second order scattering broad peak of γ-Fe_2O_3 at around 1420cm^{-1} was revealed[100], demonstrating the complete removal of all the carbon-based micelles by heating. Additionally, the $FeCl_3$ A_{1g} peak at 294cm^{-1} also vanished as compared to that of the loaded micelles spectrum(Figure 4.1 (c)) and post O_2 plasma treated spectrum(Figure 4.1 (d)), as highlighted in the

insets. The disappearance of the 2VP related peaks and the $FeCl_3$ A_{1g} peak confirmed the complete removal of micelles and conversion of the $FeCl_3$ of the drop-casting sample. The iron oxide characteristic peaks below 900cm^{-1} were fitted with Lorentzian peaks(See Figure4.2 (a)). As 600°C is sufficient to convert γ form iron oxide to the thermal stable α form, we performed extra annealing under the same condition to study the evolution of the iron oxide nanoparticles.[39, 100] After that, the Raman spectrum was collected (See Figure 4.1 (f)) and then the spectrum below 900cm^{-1} was also fitted with Lorentzian peaks(Figure4.2 (b)) for further discussion.

4.3 Phase identification of iron oxide nanoparticles

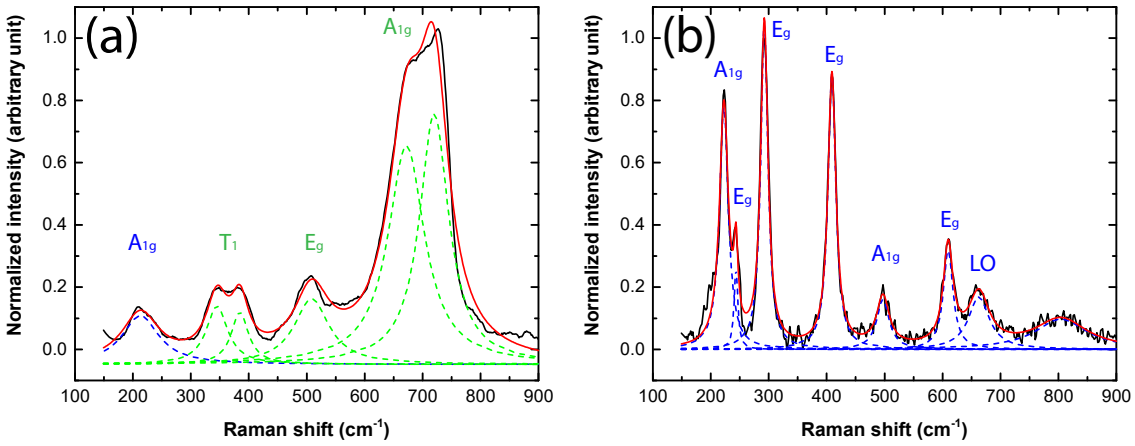

Figure 4.2: Raman spectra of the iron oxide nanoparticles under two step annealing conditions with peaks fitting. (a) Annealing at 600°C under N_2 environment for 2h; (b) Extra annealing at 600°C in N_2 environment for 2h. Note that the spectra were fitted with Lorentzian peaks.

The center positions of the fitted Lorentzian peaks from Figure4.2 were listed in the first column of Table4.2 along with the peak assignments and references. After the first annealing(600°C, N_2, 2h)(Figure4.2 (a)), the broad peak at around 700cm^{-1} could be fitted with two Lorenztian components at 670cm^{-1} and 720cm^{-1}, representing the A_{1g} stretching mode of tetrahedral units in γ-Fe_2O_3.[72, 74, 101, 106] The peak at

509cm^{-1} could be assigned to the E_g mode (symmetric bands of O with respect to Fe) of γ-Fe_2O_3 while the broad peak at around 360cm^{-1} related to the translatory T_1 mode of γ-Fe_2O_3 had two Lorenztian component at 345cm^{-1} and 384cm^{-1}.[74, 101] Those characteristic peaks indicated that the iron oxides nanoparticles were in γ form after annealing at 600°C in N_2 for 2h, as reference to table 4.1. Again, the peak at 213cm^{-1} could be related to the A_{1g} mode of α-Fe_2O_3, resulting from the laser heating effect as described above. Figure4.2 (b) shows the Lorentzian fitted spectrum after the second annealing(600°C, N_2, 2h), which is distinct from Figure4.2 (a). The spectrum features of Figure 4.2 (b) can be considered as characteristics of α-Fe_2O_3. Five E_g modes are expected for α-Fe_2O_3 but two of them (293cm^{-1} and 299cm^{-1}) are typically only be resolved below 100K.[73] As our Raman spectra were collected at room temperature, four E_g modes(243cm^{-1}, 292cm^{-1}, 409cm^{-1} and 610cm^{-1}) of α-Fe_2O_3 were observed.[73, 100] The other two peaks at 223cm^{-1} and 497cm^{-1} could be assigned to two the A_{1g} modes of α-Fe_2O_3.[73] In addition, the peak at around 660cm^{-1} was considered as the IR active longitudinal optical E_u mode activated by disorder.[100, 102, 107]. The transformation from γ-Fe_2O_3 to α-Fe_2O_3 is further supported by the shift of second order scattering peak from 1420cm^{-1} to 1320cm^{-1}, comparing Figure 4.1 (e) and (f).[100, 102] Consequently, the characteristic peaks in Figure4.2 (b) confirmed the complete conversion to α form after the second annealing step.

Summarizing the discussion from the above two sections, all the observed peaks were listed at table 4.2 in detail together with their assignments and corresponding references:

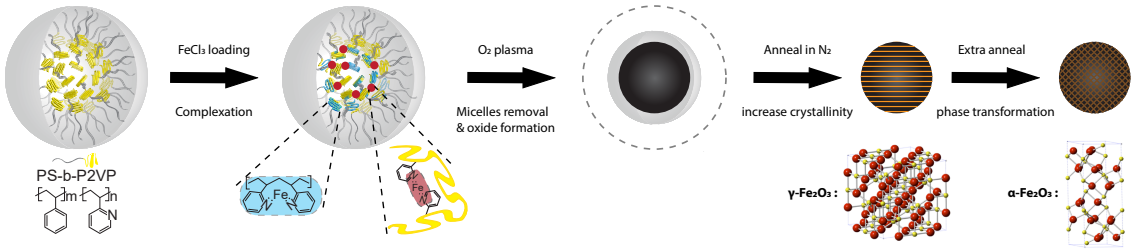

Figure 4.3: Schematic of the evolution of iron oxide nanoparticles synthesized by the reverse micelles method.

Using the Raman spectra, we can summarize the complete iron oxide nanoparticles evolution processes in Figure4.3: In the beginning, the PS-*b*-P2VP reverse micelles

Table 4.2: Table of the observed Raman peaks and their references

Observed Raman shift (cm^{-1})	Related spectra in Figure4.1	Assignment	References
213	(d)(e)	A_{1g} of α-Fe_2O_3	[73, 101]
223	(f)	A_{1g} of α-Fe_2O_3	[73, 101]
243	(f)	E_g of α-Fe_2O_3	[73, 101]
292	(f)	E_g of α-Fe_2O_3	[73, 101]
294	(c)(d)	$FeCl_3$-P2VP complex	[82, 103]
330	(b)	hydrated $FeCl_3$-P2VP complex	[80, 81]
345	(e)	T_1 of γ-Fe_2O_3	[100]
384	(e)	T_1 of γ-Fe_2O_3	[100]
409	(f)	E_g of α-Fe_2O_3	[73, 100]
497	(f)	A_{1g} of α-Fe_2O_3	[73, 100]
509	(e)	E_g of γ-Fe_2O_3	[100]
610	(f)	E_g of α-Fe_2O_3	[73, 100]
663	(f)	LO E_u of α-Fe_2O_3	[100]
670	(e)	A_{1g} of γ-Fe_2O_3	[72, 101, 106]
720	(e)	A_{1g} of γ-Fe_2O_3	[72, 101, 106]
1000	(a)(b)(c)(d)	Symmetric ring breathing of 2VP	[78, 79]
1160	(b)(c)(d)	*$FeCl_3$-P2VP complex	this work
1306	(b)(c)(d)	*$FeCl_3$-P2VP complex	this work
1446	(b)(c)(d)	*$FeCl_3$-P2VP complex	this work
1591	(a)(b)(c)(d)	Ring stretching of 2VP	[78, 79]

are formed. After that, the $FeCl_3$ is added and combined with P2VP for forming the loaded micelles. Oxygen plasma treatment can then be performed for removing the carbon-based micelles and forming the iron oxide(γ form). Annealing the nanoparticles at 600°C under N_2 environment for 2h produces γ-Fe_2O_3 with high degree of crystallinity, whereas the phase transformation to α-Fe_2O_3 can be achieved by further annealing in N_2 at the same temperature.

4.4 Summary

Along with the discussion about all the Raman spectra above, we were able to identify the exact phase of the iron oxide nanoparticles for the annealing treatments at 600°C under N_2. Moreover, three new peaks are proposed to arise from the $FeCl_3$-2VP interaction. The magnetic properties of the iron oxide nanoparticles will be discussed in the following Chapter 5.

Chapter 5

Characterization of monolayer iron oxide nanoparticles

Apart from the comprehensive results of Raman characterization in the last chapter, other characterization techniques were required to understand of the monolayer iron oxide nanoparticles by themselves instead in the thick layer as the drop-casted Raman sample. TEM, with its ability to reach atomic scale resolution, was employed to characterize the isolated iron oxide nanoparticles. With the same oxygen plasma treatment and annealing process(as described in the experimental of Chapter 4), the composition information and crystal structure of single nanoparticles were obtained directly through EELS\EDX and HRTEM. In addition, the magnetic properties of the monolayer iron oxide nanoparticles on thin silicon was studied by SQUID.

Our goal is to apply the iron oxide nanoparticles onto the anode substrates of the organic optoelectronic devices. The common anode substrates are indium tin oxide (ITO) coated float glass. The standard 600°C annealing temperature would deteriorate the electrical properties of the ITO layer and also induce the deformation of the float glass matrix, as it exceeds the maximum recommended annealing temperature of ITO from several suppliers and the strain point of the float glass. As a consequence, the annealing temperature was decreased to 350°C and the duration was extended to 12h, which should be sufficient to convert the nanosized iron oxide to either γ-Fe_2O_3.[39] In this case, TEM, Raman spectroscopy and SQUID characterization were also performed to investigate the nanoparticles, which will also be discussed later in this chapter.

5.1 Experimental

The $FeCl_3$ loaded micelles and iron oxide nanoparticles were synthesized in the procedures that have been described in section 3.2 and 3.3 in Chapter 3. Two different molecular weight polystyrene-block-poly(2-vinyl pyridine) (PS-*b*-P2VP) were used in this experiment (i.e. PS-*b*-P2VP, M_n: 75000-*b*-66500, labeled as P4824; PS-*b*-P2VP, M_n: 48500-*b*-70000, labeled as P1330).

TEM samples were prepared by spin coating (2000rpm, 45s) the loaded micelles solution on silicon nitride membranes window grids. To confirm the compositional and structural information of isolated iron oxides nanoparticles from different loaded micelles solutions, the 0.2 $FeCl_3$ loading ratio P1330 o-xylene solution and the 0.3 $FeCl_3$ loading ratio poly(2-vinyl pyridine) homopolymer in P4824 o-xylene solution (details can be seen in the experimental section in Chapter 6) were used for spin-coating and then treated by 25 mins oxygen plasma with 2h annealing at 600°C in N_2 in the end. Low temperature annealing conditions were also investigated in order to apply the resultant nanoparticles for actual device fabrication. Hence, TEM samples from 0.2 $FeCl_3$ loading ratio P4824 o-xylene solution were prepared and annealed at 350°C which was reported to produce γ phase iron oxide.[100] This temperature was suitable to be applied to the normal ITO glass substrates without degrading their properties according to the product information from several companies. In this case, two annealing processes (350°C for 12h in N_2; 350°C for 12h in air and then 350°C for 12h in N_2) were carried out for comparison.

Raman spectroscopy was again performed to study the nanoparticles with low temperature annealing processes. Following the similar sample preparation as described in experimental of chapter 4, two thick samples were prepared using low temperature annealing processes.(350°C for 12h in N_2; 350°C for 12h in air plus 350°C for 12h in N_2).

For magnetic properties measurement, the 275um thick Si substrates were cut into 40mm by 5mm stripes to accommodate the sample holder in the SQUID magnetometer. Only the center area(5mm by 5mm) of the stripe was spin-coated by the loaded micelles

solution at 2000rpm for 45s. All SQUID samples were treated with 25 mins oxygen plasma before annealing. To investigate the size effect on the magnetization, three different solutions(0.2 $FeCl_3$ loading ratio P1330 o-xylene, 0.3 $FeCl_3$ loading ratio poly(2-vinyl pyridine) homopolymer in P1330 o-xylene, 0.2 $FeCl_3$ loading ratio P4824 o-xylene) were used to produced different average size iron oxide nanoparticles with the same annealing condition(i.e. 600°C for 2h in N_2). To study the effect of low temperature annealing on the magnetization, the sample coated with 0.2 $FeCl_3$ loading ratio P4824 o-xylene solution was annealed in air at 350°C for 12h first and then was further annealed in N_2 at 350°C for 12h. In this case, the SQUID measurements were conducted between each annealing steps for direct comparison.

5.2 Composition, crystal structure and magnetic properties characterization of the nanoparticles

5.2.1 Compositional analysis of the nanoparticles

The elemental composition of the nanoparticles can be confirmed by EDX or EELS in the TEM\STEM system. The nano-size electron beam together with the thin windows of the TEM grids enables the acquisition of high-resolution EDX or EELS elemental maps and STEM images for the individual nanoparticle in the same time, which offers a powerful way to detect the nanoscale objects in great detail.[108]

Figure 5.1 (a) directly reveals the composition of the nanoparticles from P1330 o-xylene 0.2$FeCl_3$ loading ratio solution, by comparing the Fe elemental map(green) and O elemental map(red) to the selected area(purple rectangle) for EDX analysis in the STEM image. The Fe $K_{\alpha 1}$ and O $K_{\alpha 1}$ characteristic x-ray signals are concentrated in the area of the nanoparticles in the corresponding STEM image. In addition, the EDX spectrum from the same scan clearly shows the characteristic Fe $K_{\alpha 1}$ peak at 6.405KeV and $K_{\beta 1}$ peak at 7.059KeV together with characteristic O $K_{\alpha 1}$ peak at 0.525KeV, while the Cl characteristic peak($K_{\alpha 1}$ 2.622KeV and $K_{\beta 1}$ 2.812KeV) and C $K_{\alpha 1}$ peak(0.277KeV) are absent, indicating that the oxygen plasma and annealing

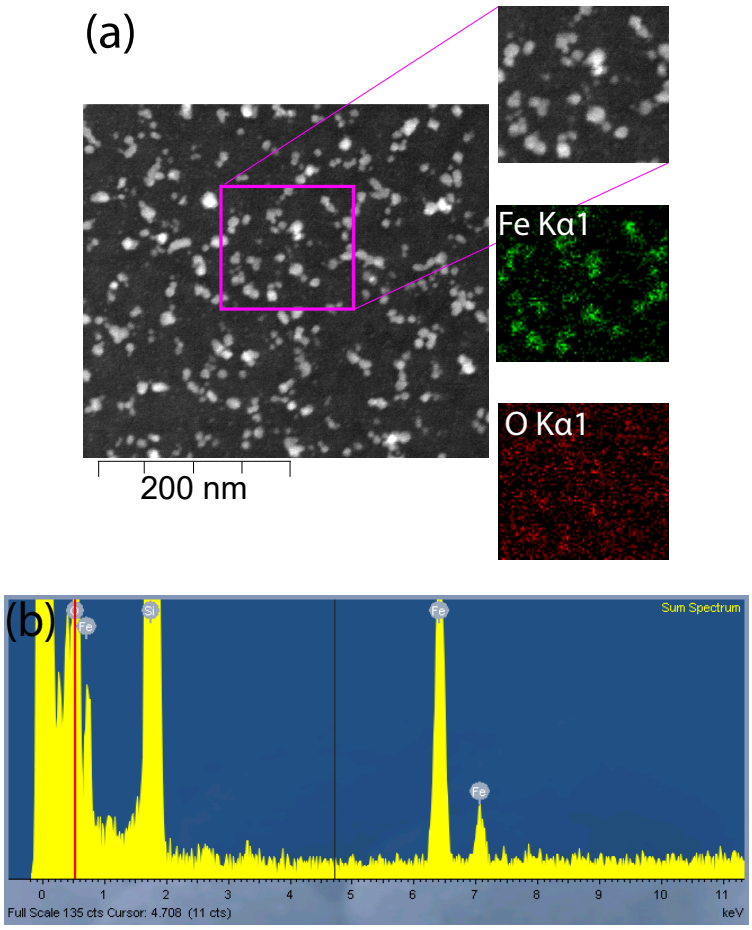

Figure 5.1: STEM/EDX analysis of nanoparticles from P1330 o-xylene 0.2$FeCl_3$ loading ratio solution. (a) Left: the STEM image of nanoparticles, right: enlarged selected area for EDX elemental mappings-Fe mapping(green color) and O mapping(red color), (b) The EDX spectrum from the EDX elemental mapping scan.

treatment are sufficient to remove the polymeric micelles and covert the $FeCl_3$ precursor to iron oxide for the spin-coated sample. This EDX result not only supports the Raman results of the sample with the treatment but provides the direct evidence of iron oxide in nanoparticle form.

We found that the EELS was more efficient for acquiring the compositional information of the nanoparticles. Decent results could be collected in a much smaller time frame because EELS measures the kinetic energy change of the inelastic electrons through the sample. Consequently, EELS was applied for investigating the composition of the smaller nanoparticles synthesized by using different type of PS-*b*-P2VP

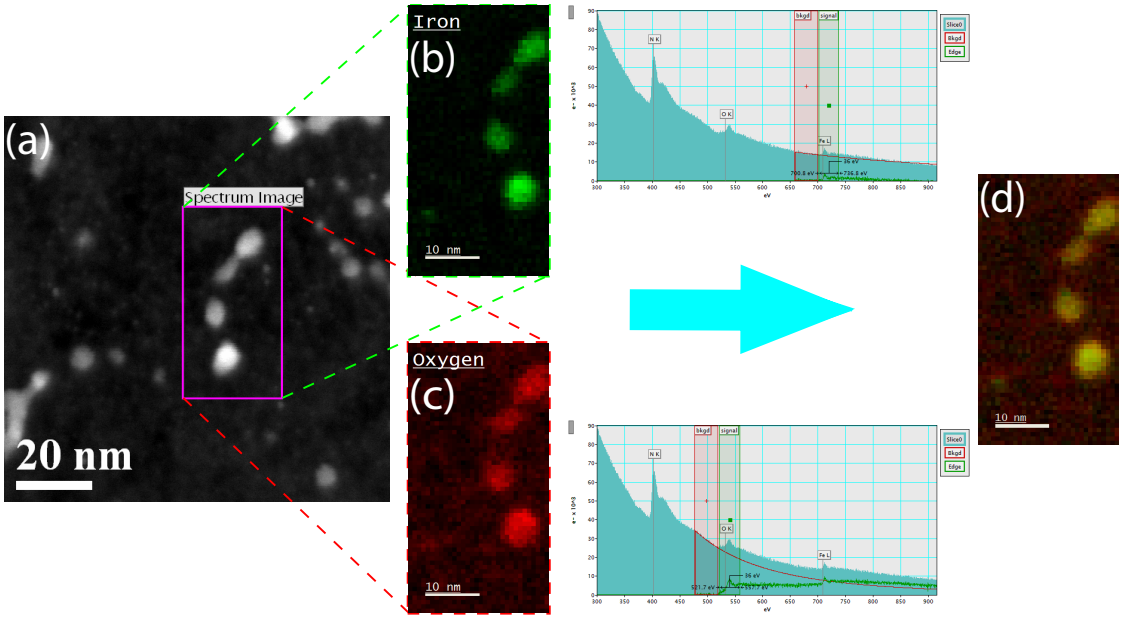

Figure 5.2: STEM/EELS analysis of nanoparticles from P4824 o-xylene HP2VP 0.3$FeCl_3$ loading ratio solution. (a) STEM image of nanoparticles(selected area for EELS indicated by purple rectangle), (b) EELS Fe mapping(green color) and corresponding EELS Fe edge, (c) EELS O mapping(red color) and corresponding EELS O edge, (d) Overlay of (b) and (c).

(P4824 o-xylene HP2VP 0.3$FeCl_3$ loading ratio solution) to verify the universality of producing the iron oxide nanoparticles using the similar reverse micelles procedures (details can be seen in the experimental of Chapter 6). The results can be seen in Figure 5.2 where (b) and (c) show the Fe (green) and O (red) elemental map with the corresponding EELS spectrums. The Fe and O elemental maps match well with the nanoparticles in the selected area highlighted in the STEM image (a), which is supported by the overlaid elemental map in the image (d). The spread out of the oxygen signal might be coming from the oxidation of the Si_3N_4 window during the oxygen plasma treatment. Nevertheless, the most intense oxygen signal arises from the nanoparticles region. Moreover, no Cl or C characteristic signals were detected, revealing that the nanoparticles consisted of only Fe and O. This EELS result shares the similar information compared to the previous EDX result.

Apart from the compositional analysis, the electron diffraction and high resolution

TEM of these two samples were also collected to study their actual crystal structure.

5.2.2 Crystal structure analysis of the nanoparticles

Although we have confirmed the exact form of the iron oxide in Chapter 4 by Raman spectroscopy, it is compelling to directly characterize the crystal structure of the individual nanoparticle in high resolution. The crystal structure analyses were performed in parallel with the above compositional analyses below.

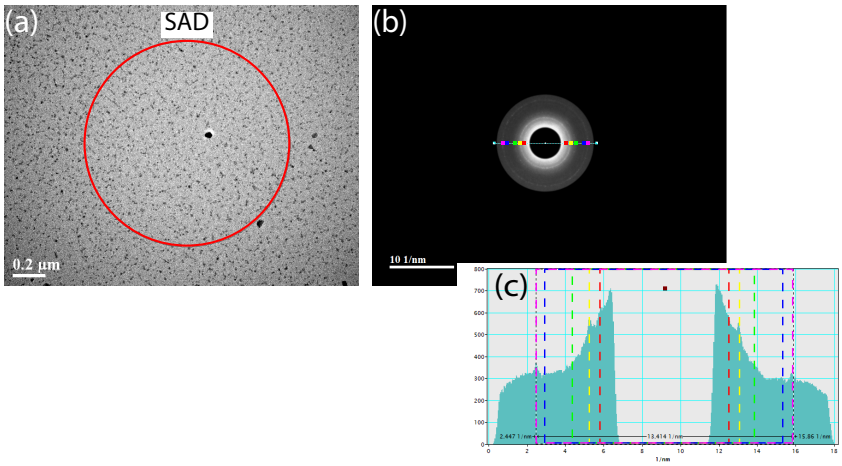

Figure 5.3: SAED of nanoparticles (annealing at 600°C for 2h in N_2) from P1330 o-xylene 0.2$FeCl_3$ loading ratio solution. (a)TEM image of the nanoparticles(selected area for electron diffraction highlighted in red circle), (b) Electron diffraction pattern from the highlighted area in (a), (c) The line intensity profile from the line in the electron diffraction pattern.

As shown in Figure 5.3, the SAED result confirms the crystal nature of iron oxide nanoparticles corresponding to the sample whose compositional information have been shown in Figure 5.1. Originating from the electron diffraction of the selected area in Figure 5.3 (a), the concentric ring patterns related to different lattice planes are clearly visible in Figure 5.3 (b). To extract and calculate the d-spacings, an intensity line profile (Figure 5.3 (c)) was drawn through the center of the diffraction pattern, where the intensity peak positions were highlighted with dash line in different colors.

The results of the d-spacings are shown in the following table 5.1:

Table 5.1: The d-spacings value of the sample, γ-Fe_2O_3 (JCPDS No.39-1346) and Fe_3O_4 (JCPDS No.75-0033), unit in Å.

Ring patterns	Sample of Figure 5.3	γ-Fe_2O_3	Fe_3O_4	(hkl)
1	2.9634	2.9530	2.9641	(220)
2	2.5490	2.5177	2.5278	(311)
3	2.0980	2.0886	2.0960	(400)
4	1.6018	1.6073	1.6135	(511)
5	1.4910	1.4758	1.4821	(440)

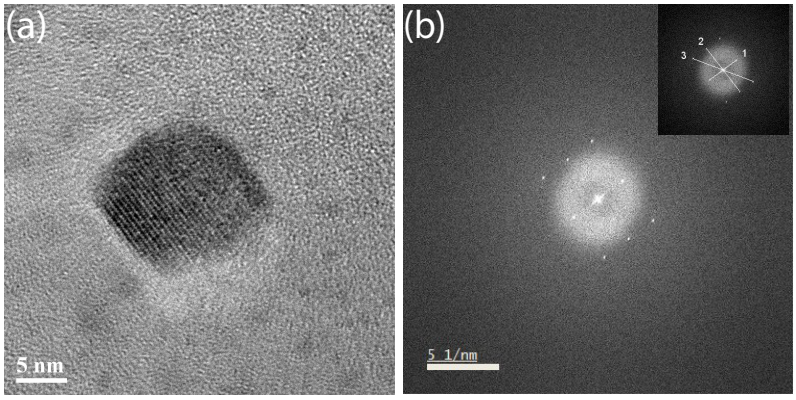

Figure 5.4: High resolution TEM image of nanoparticles (annealing at 600°C for 2h in N_2) from P1330 o-xylene 0.2$FeCl_3$ loading ratio solution. (a) A single crystal nanoparticles, (b) fast Fourier transform from (a)(inset indicates 3 reciprocal distances).

The d-spacings extracted from the first to fifth ring patterns(from the center of the diffraction pattern) can be assigned to the (220), (311), (400), (511) and (440) crystallographic planes of γ-Fe_2O_3 or Fe_3O_4, according to the information from table 5.1.[109] Moreover, the HRTEM image(Figure 5.4) from the same sample reveals clear fringes of a single iron oxide nanoparticle. The fast Fourier transform pattern from the nanoparticle shows three distinct sets of centrosymmetric diffraction spots. By interpreting those diffraction spots, we can obtain three d-spacings: 4.81Å, 2.93Åand 2.41Åwhich matches that of the (111), (220) and (222) crystallographic planes of γ-Fe_2O_3 or Fe_3O_4, agreeing with the results from Figure 5.3.

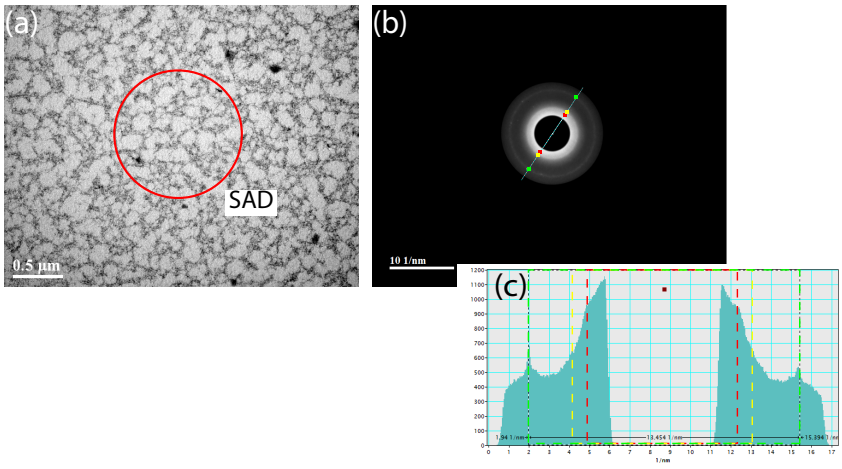

Figure 5.5: SAED of nanoparticles from P4824 o-xylene HP2VP 0.3$FeCl_3$ loading ratio solution. (a)TEM image of the nanoparticles(selected area for electron diffraction highlighted in red circle), (b) Electron diffraction pattern from the highlighted area in (a), (c) The line intensity profile from the line in the electron diffraction pattern.

The SAED of iron oxide nanoparticles synthesized by different types of PS-*b*-P2VP(P4824 o-xylene HP2VP 0.3$FeCl_3$ loading ratio solution) was also collected for comparison, as shown in Figure 5.5). The electron diffraction in Figure 5.5 (b) shows three distinguishable concentric rings. Using the intensity profile, the calculated d-spacings are summarized in the following table 5.2:

Table 5.2: The d-spacings value of the sample, γ-Fe_2O_3 (JCPDS No.39-1346) and Fe_3O_4 (JCPDS No.75-0033), unit in Å.

Ring patterns	Sample of Figure 5.5	γ-Fe_2O_3	Fe_3O_4	(hkl)
1	2.9625	2.9530	2.9641	(220)
2	2.5214	2.5177	2.5278	(311)
3	1.4865	1.4758	1.4821	(440)

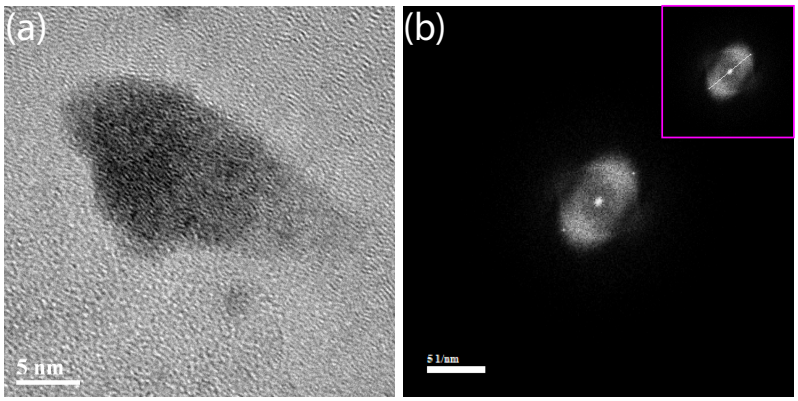

Figure 5.6: High resolution TEM image of nanoparticles (annealing at 600°C for 2h in N_2) from P4824 o-xylene HP2VP 0.3$FeCl_3$ loading ratio solution. (a) A single crystal nanoparticles, (b) fast Fourier transform from (a)(inset indicates 3 reciprocal distances).

The d-spacings extracted from the first to third ring patterns(from the center of the diffraction pattern) are consistent with that of (220), (311) and (440) planes of γ-Fe_2O_3 or Fe_3O_4, as shown in table 5.2.[109] Although the HRTEM image of the individual nanoparticle in Figure 5.6(a) does not have clear fringes as shown in Figure 5.4(a), the fast Fourier transform of it shows one clear set of diffraction spots. By analyzing that diffraction spots, we can calculate the d-spacings of 2.56Å, matching that of (311) plane of γ-Fe_2O_3 or Fe_3O_4. From the above SAED and HRTEM analyses, we can conclude that the iron oxide nanoparticles from this two samples share the same crystal structure.

Combining the compositional and structural analyses, we can confirm that the iron oxide nanoparticles with same crystal structure could be synthesized generally by the reverse micelles methods despite changing the molecular weight of PS/P2VP block and adding the HP2VP for $FeCl_3$ loading, under the typical O_2 plasma and annealing

treatment.

5.2.3 Magnetic properties of monolayer iron oxide nanoparticles after standard 600°C annealing

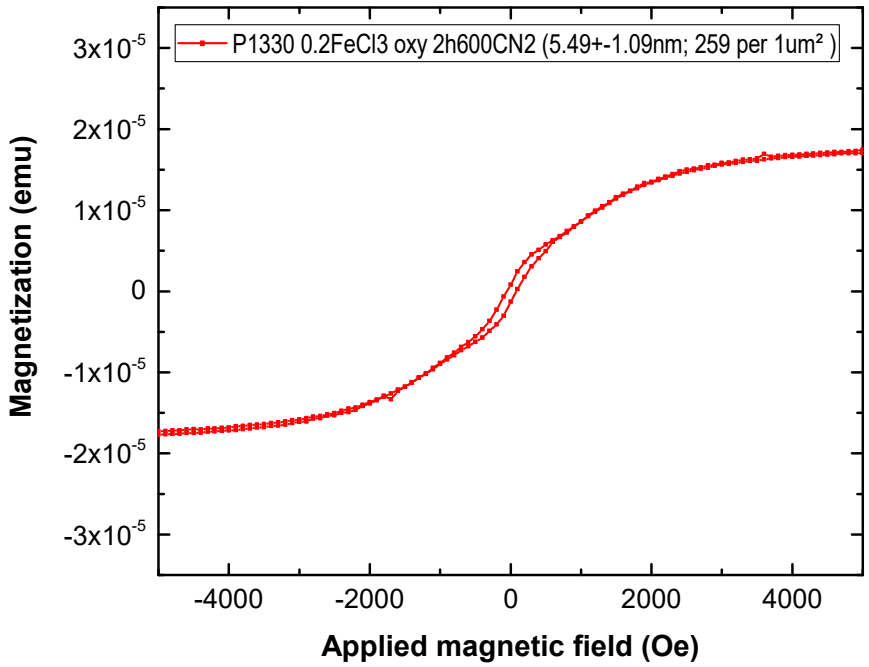

Figure 5.7: Magnetization-applied magnetic field curve of monolayer iron oxide nanoparticles on silicon substrates after 600°C annealing in N_2 for 2h. Note that nanoparticles were from P1330 o-xylene 0.2$FeCl_3$ loading ratio solution.

After the standard annealing process (600°C in N_2 for 2h), the magnetization-applied magnetic field (M-H) curve of iron oxide nanoparticles arrays on silicon was collected at 300K using SQUID, as shown in Figure 5.7. The average heights of nanoparticles were determined by randomly picking 100 nanoparticles in the corresponding AFM topography image,[110] which appeared to have an average height of 5.49nm with 1.09nm standard deviation. (The detailed procedure to extract the height will be discussed in section 6.5.2) According to the estimation from equations 2.1 and 2.3 in section 2.1.2, the size of those nanoparticles was below the single domain limit and superparamagnetic limit of γ-Fe_2O_3 if the nanoparticles were spherical. In

fact, the coercive field (H_c) was existed with the magnitude at around 50Oe extracted from the M-H curves. Although H_c was relatively small and below the applied field increment(100Oe), it did suggest that the nanoparticles were not superparamagnetic, implying the shape might not be a perfect sphere, which was consistent with the TEM results above. In addition, the remanence magnetization (M_r) was extremely small in the order of the 10^{-7} emu region, which was approaching the detection limit in the SQUID measurement. The M_r was less than 8% of the magnetization at 2000Oe applied field, indicating the net magnetization was low with the external magnetic field. The H_c and M_r indicated the soft magnetic nature of those nanoparticles, giving rise to almost an instantaneous response to the external applied magnetic field.

To confirm that the γ-Fe_2O_3 nanoparticles were responsible for this specific magnetic response, the above tested sample was further annealed in N_2 at 600°C for 2 hours, which would convert the ferrimagnetic γ-Fe_2O_3 to the α-Fe_2O_3 as confirmed in chapter 4. After the second annealing, the magnetic response of that sample was below the detection limit of the SQUID due to the weak magnetic ferromagnetic nature of the α-Fe_2O_3 at room temperature[111], supporting that the specific magnetic response was derived from the ferrimagnetic γ-Fe_2O_3 NPs.

5.2.4 Compositional and structural analysis of the nanoparticles from low temperature annealing processes

In this part, the compositional and structural analyses of the nanoparticles from low temperature annealing processes will be described.

The SAED result of the sample (annealing at 350°C for 12h in N_2) suggests an amorphous nature of the nanoparticles with the diffused electron diffraction pattern where the line intensity profile did not possess obvious peaks, as shown in Figure 5.8 (a) and (b). In addition, we changed the annealing condition by adding a new period annealing(350°C for 12h in air) first in order to make sure the full oxidation of the $FeCl_3$ and the removal of carbon-based residue through the oxidation, and then the sample was further annealed at 350°C for 12h in N_2. The related SAED result

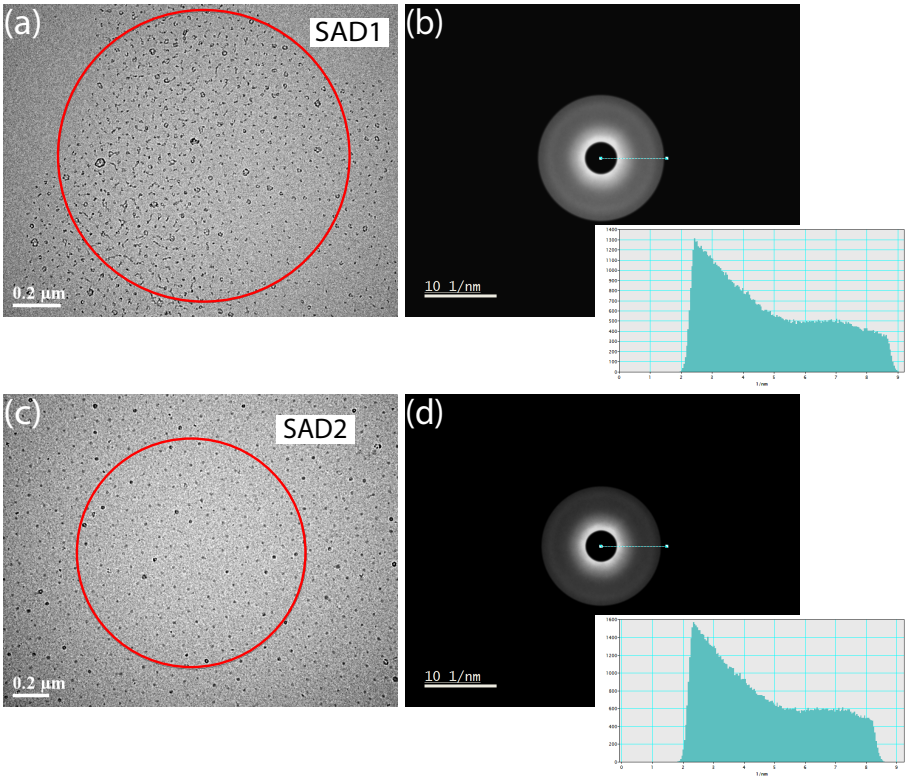

Figure 5.8: SAED of nanoparticles from P4824 o-xylene 0.2$FeCl_3$ loading ratio solution under different annealing conditions. (a) TEM image of the nanoparticles annealed at 350°C for 12h in N_2, (b) Electron diffraction pattern from the highlighted red circle area in (a) with line intensity profile, (c) TEM image of the nanoparticles annealed at 350°C for 12h in air and another 12h in N_2, (d) Electron diffraction pattern from the highlighted red circle area in (c) with line intensity profile.

was shown in Figure 5.8 (c) and (d), revealing the similar amorphous nature of the nanoparticles. However, the nanoparticles of the selected area(Figure 5.8 (a) and (c)) were sparser compared to that in Figure 5.3 (a) and Figure 5.5 (a), which indicates a small amount of materials. Those diffused ring patterns might be originated from the amorphous Si_3N_4, as the amount of the nanoparticles was probably inadequate in the selected area. Due to the limited size of electron aperture, the selected area for electron diffraction was small so that the amount of materials on that area was not enough to yield a clear diffraction pattern.

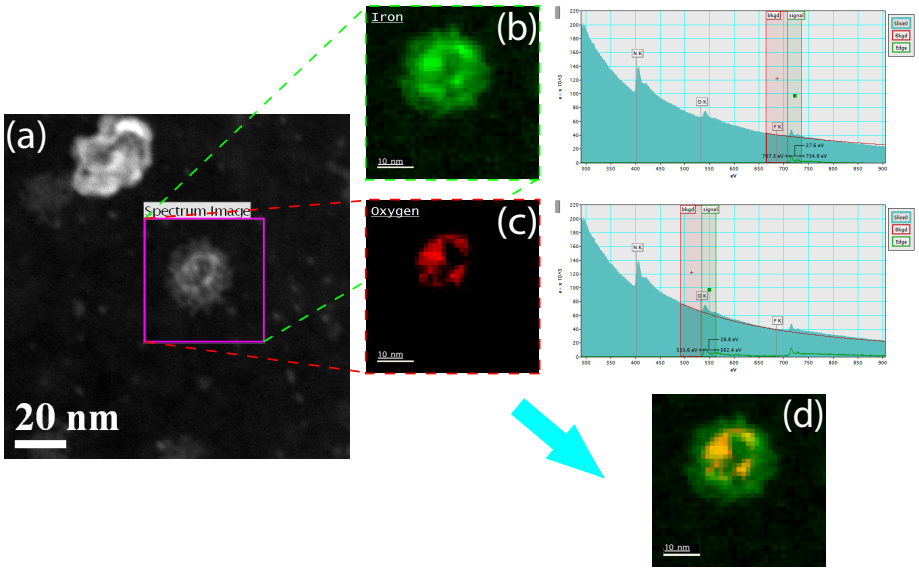

Figure 5.9: STEM/EELS analysis of nanoparticles from P4824 o-xylene 0.2$FeCl_3$ loading ratio solution. (a) STEM image of nanoparticles(selected area for EELS highlighted by purple rectangle), (b) EELS Fe mapping(green color) and corresponding EELS Fe edge, (c) EELS O mapping(red color) and corresponding EELS O edge, (d) Overlay of (b) and (c).

EELS was again applied for investigating the composition of the nanoparticles from the low temperature annealing processes(350°C for 12h in air and the 350°C for 12h in N_2). The results can be seen in Figure 5.9. The Fe and O characteristic signals were concentrated in the area of a single nanoparticle in the selected area highlighted in the STEM image (a), revealing the iron oxide nature of the nanoparticle. This was further supported by the overlaid elemental maps in Figure 5.9 (d). Moreover, no Cl or C characteristic signals were detected, confirming the complete conversion of $FeCl_3$ and removal of carbon-based residues using the low temperature annealing.

Without the structural information from the TEM, other methods were required to gain a further understanding of the resultant nanoparticles from the low temperature annealing. As Raman spectroscopy has shown conducive results before, it was thus applied to study the low temperature annealing, which would be discussed in the following section.

5.3 Phase identification under different annealing conditions by Raman spectroscopy

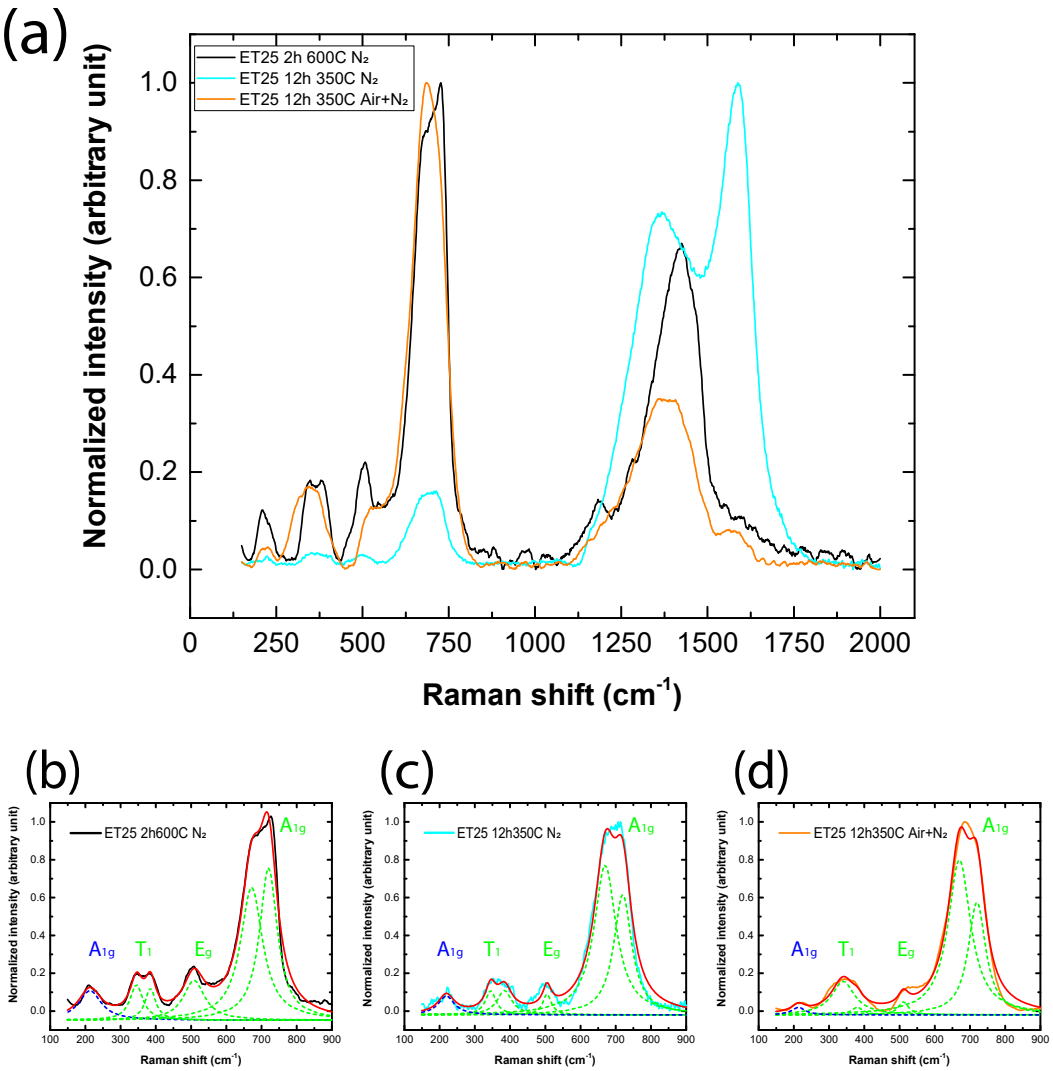

Figure 5.10: Raman spectra of iron oxide nanoparticles on KBr substrates under three annealing conditions. (a) Normalized full spectra of three annealing conditions; Normalized spectra in the region between 150 and 900 cm^{-1} and the related Lorentzian fits(Dash lines) of iron oxide nanoparticles on KBr substrates under (b) 600°C annealing for 2h in N_2, (c) 350°C annealing for 12h in N_2, (d) 350°C annealing for 12h in air with additional 12h in N_2.

As described above, comprehensive information of the iron oxide nanoparticles could be obtained conveniently by Raman spectroscopy. Therefore, two Raman samples were prepared following the sample preparation procedures in the experimental section for the purpose of examining the nature of the nanoparticles under two low-temperature annealing conditions.

The normalized full spectra of those two low-temperature annealing samples can be seen in Figure 5.10 (a) labeled with blue and orange respectively. For comparison, the spectrum of the well-characterized γ-Fe_2O_3 nanoparticles from annealing at 600°C in N_2 for 2h was also placed in the same figure. No obvious peaks related to the $FeCl_3$ or PS-*b*-P2VP micelles were observed after these three annealing processes. The samples annealed at 600°C in N_2 for 2h and at 350°C in Air for 12h plus in N_2 for another 12h showed only one prominent broad peak at around 1400cm^{-1} in the region above 1000cm^{-1}, which can be assigned to second order scattering of γ-Fe_2O_3,[100] implying the complete removal of the carbon-based micelles and conversion of $FeCl_3$ of the thick drop-casting sample. However, two broad peaks at around 1360cm^{-1} and 1587cm^{-1} remained from the sample under another low temperature annealing (350°C in N_2 for 12h). Those two peaks showed different features and Raman shift comparing to the peaks related to the micelles or $FeCl_3$-P2VP complex as described in Chapter 4. The disappearence of the PS-*b*-P2VP characteristic peak at 1000cm^{-1} and the $FeCl_3$ peak at 294cm^{-1} further reinforced the different origin of these two peaks. In fact, they were consistent with the amorphous carbon doublet peaks at that region.[112] Those amorphous carbon peaks indicated there was still carbon residue in the sample probably due to the anoxia environment with low-temperature annealing. As seen in table 4.1, the characteristic Raman active peaks for different phase of iron oxide occur below 900cm^{-1}. Thus the spectra of that region were plotted and fitted with Lorentzian peaks in Figure 5.10 (b), (c) and (d) for further discussion.

The detailed peaks analysis of Figure 5.10 (b) has being carried out in section 4.3, which confirmed the γ-Fe_2O_3 nature of the nanoparticles under the orignal annealing condition (600°C in N_2 for 2h). Moving toward the spectra of low temperature annealing, Figure 5.10 (c) displays the Lorentzian fitted spectrum of the sample annealed at 350°C in N_2 for 12h. The broad peak at around 700cm^{-1} can be decomposed to two Lorenztian components at 670cm^{-1} and 720cm^{-1} which are related to the A_{1g} stretching

mode of the tetrahedral units in γ-Fe_2O_3.[72, 74, 101, 106]. Additionally, the fitted peaks at 505cm^{-1}, 384cm^{-1} and 345cm^{-1} are also evidence of γ-Fe_2O_3, with the first peak related to the E_g mode and the other two to the T_1 mode.[74, 101] Likewise, the fitted peak at 219cm^{-1} can arise from the laser induced α-Fe_2O_3 as described above. The Lorentzian fitted spectrum from another low temperature annealing(350°C for 12h in air + 12h in N_2) can be seen in Figure 5.10 (d). The fitted Lorenztian components are located at 720cm^{-1}, 670cm^{-1}, 511cm^{-1}, 380cm^{-1}, 340cm^{-1} and 213cm^{-1}, sharing similar Raman shifts with the corresponding fitted peaks shown in Figure 5.10 (c) and thus can be assigned similarly. Zooming into the low Raman shift region in 5.10 (d), the normalized intensity of the laser induced α-Fe_2O_3 peak at 213cm^{-1} is just above the baseline, whereas that of in Figure 5.10 (b) is obvious higher, indicating that the 600°C annealing might have partially converted the iron oxide to α phase. The Lorentzian fitted peaks positions of Figure 5.10 (b) to (d) are summarized in table 5.3 with the assignments and references, indicating that those two 350°C annealing processes produce γ-Fe_2O_3 successfully.

Table 5.3: Table of the Lorentzian fitted Raman peaks positions(cm^{-1}) with assignments and references for different annealing conditions

600°C for 2h in N_2	350°C for 12h in N_2	350°C for 12h in air + 12h in N_2	Assignment	References
213	219	213	A_{1g} of α-Fe_2O_3	[73, 101]
345	345	340	T_1 of γ-Fe_2O_3	[100]
384	384	380	T_1 of γ-Fe_2O_3	[100]
509	505	511	E_g of γ-Fe_2O_3	[100]
670	670	670	A_{1g} of γ-Fe_2O_3	[72, 101, 106]
720	720	720	A_{1g} of γ-Fe_2O_3	[72, 101, 106]

Figure 5.11 clearly shows the mixture of the gamma and alpha phase with the thick layer, according to reference table 4.1. The sample was thick layer prepared by multiple drop casting, which underwent two annealing process: 600°C annealing for 2h in N_2 and another 600°C annealing for 6h in air.

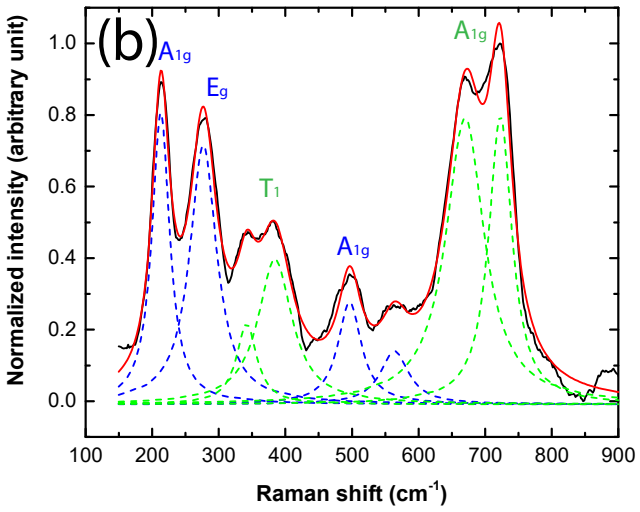

Figure 5.11: Raman spectra of iron oxide nanoparticles on KBr substrates showing both alpha and gamma phase.

Combining the information from Figure 5.10 (a) to (d), we can conclude that the low temperature annealing process(350°C for 12h in air + 12h in N_2) seems to be a good substitution for the original annealing one (600°C for 2h in N_2), as it was able to remove the carbon-based residues completely and produce γ-Fe_2O_3 nanoparticles while reducing partial conversion to α phase. As a result, the iron oxide nanoparticles could be applied to the practical device fabrication processes.

5.3.1 Magnetic properties of monolayer iron oxide nanoparticles under different annealing conditions

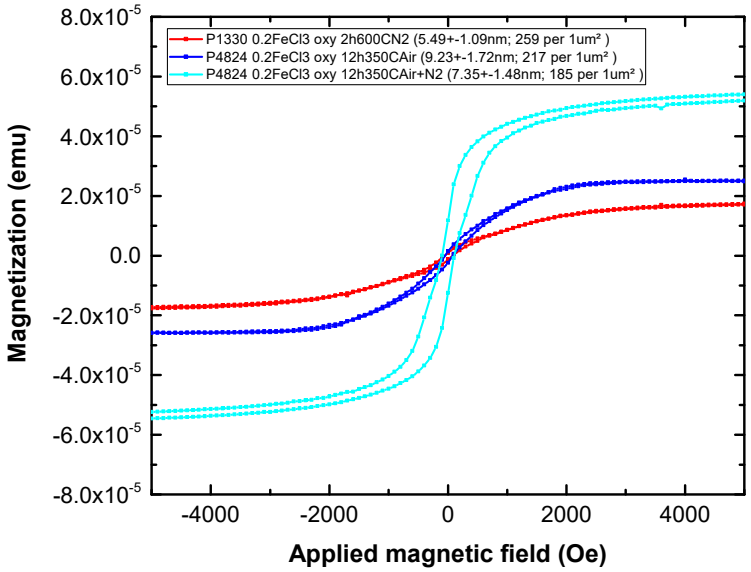

Figure 5.12: Magnetization-applied magnetic field curves of monolayer iron oxide nanoparticles on silicon substrates with different annealing conditions.

As we confirmed that the low temperature annealing process (350°C for 12h in air + 12h in N_2) could be applied to produce γ-Fe_2O_3 nanoparticles, it is worth checking the magnetic properties of the monolayer nanoparticles in each stage of this two steps annealing process. Figure 5.12 shows the magnetization-applied magnetic field (M-H) curves of the nanoparticles on silicon after first and second steps annealing, accompanied by a reference M-H curve from 600°C annealing process.

The coercive field (H_c) was at around 50Oe extracted from the sample after the first step annealing at low temperature, similar to that of the 600°C annealing. In addition, the remanence magnetization (M_r) was similarly small in the order of the 10^{-7} emu region, contributing to less than 8% of the magnetization at 2000Oe applied field. Both H_c and M_r indicated the soft magnetic nature of those nanoparticles, yielding a similar result as 600°C annealing. However, the magnetic properties changed after the second step annealing. In this case, the H_c was at around 100Oe with the M_r in the $^{-5}$ emu region which accounted for 25% of the magnetization at 2000Oe, showing a clear

hysteresis.

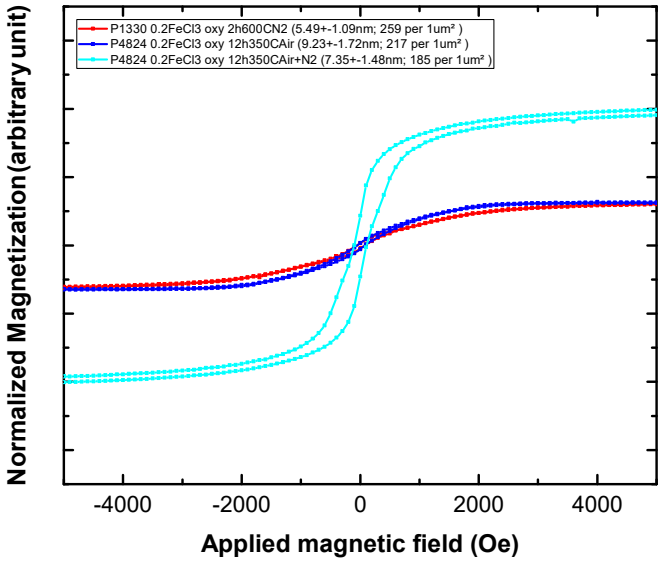

Figure 5.13: Normalized magnetization-applied magnetic field curves of monolayer iron oxide nanoparticles on silicon substrates with different annealing conditions. Note that the normalization was based on the average height and density of the nanoparticles from the corresponding AFM topography images.

In terms of saturation magnetization (M_s), the size and the density of nanoparticles need to be considered for a direct comparison. Figure 5.13 shows the normalized M-H curves from Figure 5.12. Surprisingly, the normalized magnetization at 5000Oe, which could be set as the M_s in all three curves (leveling off), is significantly higher for the sample after finishing two steps low temperature annealing, while M_s of the sample from first step low temperature annealing and 600°C annealing shares similar magnitude. This could be explained by the partial conversion of γ-Fe_2O_3 to α-Fe_2O_3 when using 600°C annealing, which reduces the M_s due to the weak ferromagnetic nature of α-Fe_2O_3, supporting the Raman results from above. Moreover, another sample was prepared and underwent two annealing process: 600°C annealing for 2h in N_2 and another 600°C annealing for 6h in air, which was the same condition being applied in Figure 5.11. In this case, the magnetic response of the sample was below the detection limit of the SQUID, indicating the SQUID was sensitive to monitor the conversion to alpha phase of monolayer iron oxide nanoparticles. Alternatively,

the crystallinity might not reach the maximum after first period low temperature annealing, resulting in relatively low M_s.

Comparing the M-H curves results, we can confirm the iron oxide nanoparticles possess decent magnetic properties using low temperature annealing process, which potentially yields higher purity γ-Fe_2O_3.

5.4 Preliminary organic solar cells testing

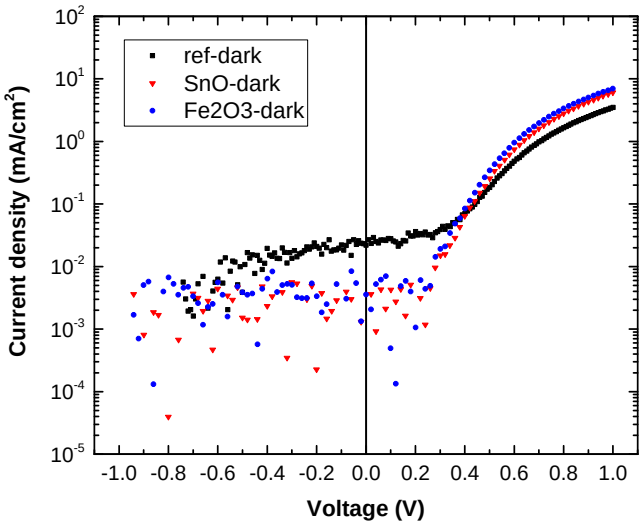

Figure 5.14: Current density-voltage characteristics for OPV devices with various interlayers under dark condition

Prevous work in our group[1] has shown that SnOx nanoparticles increased the performance of OLEDs by enhancing hole injection. Therefore, the SnOx nanoparticles were also used for comparison in this investigation. At room temperature, magnetic field showed positive impact on poly[4,4-bis(2-ethylhexyl)-cyclopenta-(2,1-b;3,4-b)dithiophen]-2,6-diyl-alt-(2,1,3- benzo-thiadiazole)24,7-diyl (PCPDTBT) which is

[1]submitted as "Improved hole injection for blue phosphorescent organic light-emitting diodes using solution deposited tin oxide nanoparticles decorated ITO anodes, S. Lee, G. Yun, J. Kim, G. Hanta, K. Liang, L. Kojvic, L. S. Hui, A. Turak, and W. Kim, Applied Physics Letters"

intensively used in bulk heterojunction solar cells, by affecting the current through the PCPDTBT-based diode.[97] Hence, it is interesting to investigate how the magnetic nanoparticles could affect the organic electronic devices.

Using the organic solar cells fabrication procedures in section 3.5, three devices were produced with bare ITO, SnOx nanoparticles coated ITO and γ-Fe_2O_3 nanoparticles coated ITO(using low temperature annealing: 350°C in air for 12h and in N_2 for another 12h), with the bare ITO representing the reference device.

The current density-voltage characteristics under dark condition can be seen in Figure 5.14. The high current rectification ratios at ±1V indicated that adding nanoparticles (SnOx or γ-Fe_2O_3) does not limit the device performance/shockley diode behaviors. The turn on voltage (corresponding to 1mA/cm^2 current density) is at around 0.64V and 0.61V for the SnOx nanoparticles and the γ-Fe_2O_3 device respectively, both lower than that of the reference (bare ITO device) at 0.71V. In addition, the reverse bias leakage current is less in both devices with nanoparticles compared to the reference device.

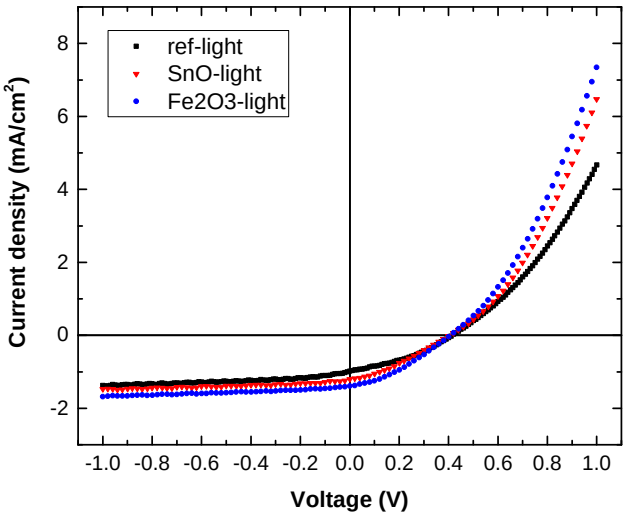

Figure 5.15: Current density-voltage characteristics for OPV devices with various interlayers under illumination.

Table 5.4: Solar cell performance of the illuminated diodes with anode modifications. Values are normalized to that of the reference device.

Sample	J_{SC}	V_{OC}	FF	R_{sh}	R_s
Ref	1	1	1	1	1
SnOx	1.22	0.97	0.88	1.82	1.19
γ-Fe_2O_3	1.41	0.98	0.95	1.74	1.00

Figure 5.15 shows the current density-voltage characteristics of three OPV devices under illumination. In this case, lab light source was applied in preliminary tests instead of using a standard 1.5AM solar simulator. Therefore, the power conversion efficiency was not calculated. Several solar cells parameters are summarized in table 5.4. The shunt resistance (R_{sh}), extracted by the slope of the J-V curve at V=0, is generally associated with leakage currents in the device.[113] The short circuit current (J_{SC}) shows an increase with respect to that of the reference OPV devices when the applying SnOx and γ-Fe_2O_3 on the ITO, suggesting the potential to reach higher output with adding the nanoparticles. In addition, the open circuit voltage is not affected as compared to a previous study using the same OPV structure.[114] The introduction of SnOx and γ-Fe_2O_3 nanoparticles to the ITO largely increase the R_{sh} values, indicating a reduction of the power loss.

This section presented the preliminary results on basic structure OPV devices. Further optimization of the devices needs to be carried out in order to elaborate the effect of magnetic nanoparticles on OPV and OLED devices. Additionally, applying an external magnetic field on OPV and OLED devices with the magnetic nanoparticles incorporated should be conducted.

5.5 Summary

Monolayer iron oxide nanoparticles were examined in detail throughout this chapter. With the help of TEM/STEM together with EDX/EELS, we were able to confirm the compositional and structural information of individual nanoparticles, showing that the PS-*b*-P2VP/$FeCl_3$ system possess the universality on the generation of iron oxide

nanoparticles after the typical O_2 plasma and annealing treatment. Moreover, SQUID magnetometer was used to characterize the magnetic properties of this nanoparticles arrays, revealing the soft magnetic nature of these nanoparticles. Importantly, low temperature annealing processes were carried out for the purpose of facilitating the fabrication of actual devices, which showed the success of producing γ-Fe_2O_3. The preliminary results of the OPV devices with γ-Fe_2O_3 exhibited a positive effect, constituting a good starting point for the further devices investigation.

Chapter 6

Dispersion of micelles and iron oxide nanoparticles

In this chapter, the dispersion of the micelles and nanoparticles will be evaluated using quantitative methods, as the distribution of the nanoparticles could have large influnce in the surface modificaiton of the substrates for devices. In addition, a method to reveal the loading ratio of $FeCl_3$ is introduced, accompanied by the discussion on the size control of iron oxide nanoparticles.

6.1 Experimental

The micelles formation was the same as described in section 3.2.2. Polystyrene-block-poly(2-vinyl pyridine)(PS-*b*-P2VP, M_n: 48500-*b*-70000, labeled as P1330; PS-*b*-P2VP, M_n: 75000-*b*-66500, labeled as P4824) diblock copolymer was dissolved in toluene and o-xylene with the same concentration to study the solvent effect on dispersion. The above two solutions were spin coated on clean silicon substrates using the same spin coating procedure in section 3.3 for dispersion analysis. To investigate the influence of spin coating speeds on micelles dispersion, the spin speed was varied from 2000rpm to 8000rpm with 2000rpm increment using the P1330\ o-xylene solution.[65] Two different concentrations of P4824\ o-xylene micelles solutions (3.00mg/ml and 3.75mg/ml) were applied to study the effect on micelles dispersion. In summary, different solvents, spin coating speeds, and concentrations were used to study the dispersion of the micelles,

which will be discussed in detail in section 6.3.

Similarly, the iron oxide nanoparticles array were generated following the same processes in section 3.2. Normally, the loading ratio(the number of the Fe^{3+} ion divided by the number of the 2VP molecular units in PS-*b*-P2VP) was set to 0.2 to examine nanoparticles array dispersion, yielding a clear solution without visible unloaded powder residues. Two additional methods were applied for tuning the dispersion of the nanoparticles, as described in section 6.1.2 and 6.1.3.

The above micelles or iron oxide nanoparticles array on silicon substrates were characterized by AFM or SEM to obtain the topographic information. WSxM were used to extract the AFM raw data.[99] The information related to the size, location(x, y coordinates) and number of nanoparticles was acquired by ImageJ[115] through the binary and finding maxima functions. Dispersion analysis was done by using the disLocate package[66] in Mathematica.(See 6.1.4)

6.1.1 Iodine stained micelles on TEM grid

Thin layer of micelles was deposited to the porous carbon thin film TEM grids by using dip-coating, which allowed direct TEM/STEM characterization of the individual micelles. In order to selectively stain the P2VP cores, the micelles coated TEM grids were then exposed to I_2 vapor for 3 hours at room temperature, by placing iodine crystals and TEM grids in a sealed glass container.[116, 117]

6.1.2 Co-solvents for tuning the dispersion of the nanoparticles array

Ethanol and methanol were selected in order to investigate the co-solvents effect on the dispersion of nanoparticles in our systems. In this experiment, the concentration of PS-*b*-P2VP(P1330) in o-xylene was set to 3.00mg/ml and the loading ratio of the $FeCl_3$ was 0.2. After stirring for one week, the small amount of ethanol and methanol(10ul for 1ml o-xylene)were added to the above loaded micelles solutions and were kept

stirring for one week again before the spin coating and O_2 treatment.

6.1.3 Poly(2-vinyl pyridine) homopolymer assisted loading for modifying the dispersion of the nanoparticles array

Poly(2-vinyl pyridine) homopolymer(HP2VP) was employed as a precursor carrier for the PS-*b*-P2VP micelles system in order to improve the dispersion of the nanoparticles array.[68] Following the similar procedures as described in reference,[68] 6mg of HP2VP (Mn: 77000g/mol) and $FeCl_3$ were mixed together in 1ml toluene or o-xylene in a vial which was kept stirring for 72 hours. Simultaneously, 15mg of PS-*b*-P2VP(P4824) was added to 4ml toluene or o-xylene and stirred for 72 hours to form the micelles in another vial. The micelles solution was then transferred to the $FeCl_3$-HP2VP mixture solution and stirred for another week. In addition, the resulted solution was centrifuged at 11500rpm for 12 minutes to remove any insoluble substances. The amount of $FeCl_3$ was accurately controlled to obtain the 0.3 loading ratio(in this case, the ratio between the number of Fe^{3+} ions and 2-vinyl pyridine in HP2VP). Following the same procedure as section 3.3, nanoparticles array was generated for further dispersion analysis.

6.1.4 Dispersion analysis using disLocate package in Mathematica

[1]

The disLocate package[66] developed by Dr.M. Bumstead from Dr. Turak's group encompasses a series of tools and metrics to gauge the spatial dispersion of two-dimensional distributed objects, which is particularly conducive to the quantitative analysis of our micelles and nanoparticles arrays. Among the tools in the package, the pair correlation function and the Voronoi area deviation were utilized as the major techniques for the dispersion analysis in this chapter.

[1] Parts of this section were published in Bumstead, M., Liang, K., Hanta, G., Hui, L. S., Turak, A. (2018). disLocate: tools to rapidly quantify local intermolecular structure to assess two-dimensional order in self-assembled systems. Scientific reports, 8(1), 1554.

The pair correlation function[118], also known as "the radial distribution function", can be applied to examine the translational order for particles. The probability of finding other particles at different distances(center to center) from each particle can be obtained using the following function:

$$g(r) = \frac{N_n(r)}{2\pi r \Delta r \rho} \tag{6.1}$$

Where Δr is the width of the annulus from the center of the particle; $N_n(r)$ is the neighbor probability as a function of distance, which is determined by counting the particle inside the annulus; ρ is the density of the configuration. The peaks from this function provide the information about short and long-range translational order. The relative interparticle spacing can be extracted from the position of the first peak. To get a reliable result from the pair correlation function, it usually requires a large number of particles. Thus a bootstrap technique was implemented to smooth the $g(r)$ generated by a finite set of data points from AFM or SEM images(Detail description can be found in reference [66]). Also, the root mean square difference (Δrms) from the related hexagonal array in g(r) and the root mean square hexatic displacement (σ) are generated to gauge the dispersion.

The Voronoi tessellation is a plane partitioning method depending on the coordinates information of the points inside the plane, resulting in polygonal segmentations within the plane. The polygons are constructed by a set of perpendicular bisectors of the lines connecting adjacent points.[119, 120] Random points dispersed inside the plane would lead to a wide distribution of shape and size of the Voronoi segmentation compared to those of highly ordered points.[121] The Voronoi area deviations in the disLocate package are calculated by the following equation:

$$\Delta A = \left| \frac{A^{vor} - A^{hex}}{A^{hex}} \right| \tag{6.2}$$

Where A^{vor} is the area of the Voronoi cell from the experimental data point; A^{hex} is the area of the corresponding Voronoi cell from the hexagonally arranged data point. The total area and the number of points are the same in this case. In addition, the levels of deviation from the ideal hexagonal Voronoi cells are highlighted in different

color for visualization with deep blue, blue, light blue, green, yellow, orange, red from 0 to 35% deviation with a 5% increment. This parameter, which is very sensitive to the random deviations of points, provides another way to gauge the order of the micelles and nanoparticles arrays.

6.2 Micellar core size

The PS-*b*-P2VP reverse micellar cores, in which the precursors are concentrated, have a direct impact on the resulting nanoparticles. As a result, investigating the size of the P2VP core is of interest. According to some previous reports,[116, 117, 122] iodine vapor could selectively stain the P2VP core of PS-*b*-P2VP micelles. The iodine stained core of the micelles could be observed directly via TEM/STEM due to the fact that the iodine yields a great phase and atomic number (Z) contrast from the carbon-based micelles.

6.2.1 Micellar core size of the PS-*b*-P2VP with different molecular weight

Typically, changing the molecular weight of the diblock copolymer has a direct impact on the aggregation number(the number of the diblock copolymer molecules that make up the micelle) which influences the core and corona size of the micelle.[56, 59, 123] To study this effect, two types of PS-*b*-P2VP(with different molecular weight in PS and P2VP block, P1330 and P4824)were dissolved in toluene to produce 3.00mg/ml solutions respectively.

As shown in Figure 6.1 (a) and (c), the iodine stained P2VP core appears to be darker than the background in the bright field TEM images, which facilitates determining the size information of the core. The size of the cores was acquired by ImageJ using the binary function. In addition, the binarized image was overlaid on top of the related TEM image to gauge the outcome before the size analysis.

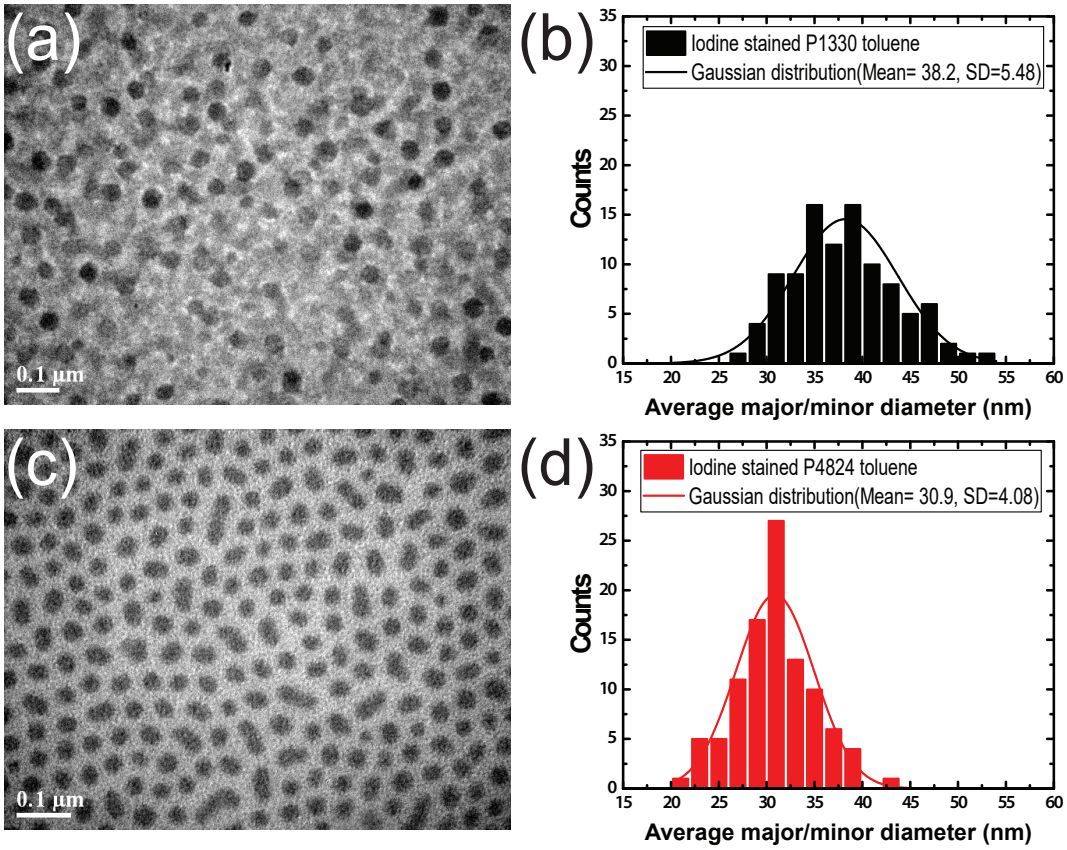

Figure 6.1: Iodine stained PS-*b*-P2VP micelles with different molecular weight using toluene as the solvent. (a) TEM image of iodine stained P1330 micelles, (b) core size histogram and the Gaussian distribution of P1330 micelles, (c) TEM image of iodine stained P4824 micelles, (d) core size histogram and the Gaussian distribution of P4824 micelles. Note that the cores appear to be darker due to the selective of iodine on P2VP block.

The size distribution of micellar cores was determined by randomly selecting individual cores in the binarized images. One hundred cores were analyzed to acquire the statistical representation of the size.[110] In addition, Gaussian function was applied to the raw data to minimize the effect of extra small or large outliers. The mean size of the P4824 core was 30.9 ± 4.08nm which was smaller than that of the P1330 core (38.2 ± 5.48nm), although they share a similar molecular weight of the P2VP block(66.5K in P4824, 70.0K in P1330). This phenomenon indicated that the core size of the micelles was not only determined by the P2VP block. In fact, it has to do with the aggregation number of the micelles and the solvent interaction with the polymer. The polydispersity indices(PDI, relative standard deviation from the

Gaussian function) were 0.13 and 0.14 for P4824 and P1330 respectively, revealing the narrow size distribution of both micellar cores.

6.2.2 PS-*b*-P2VP(P1330) micellar core size in different solvents

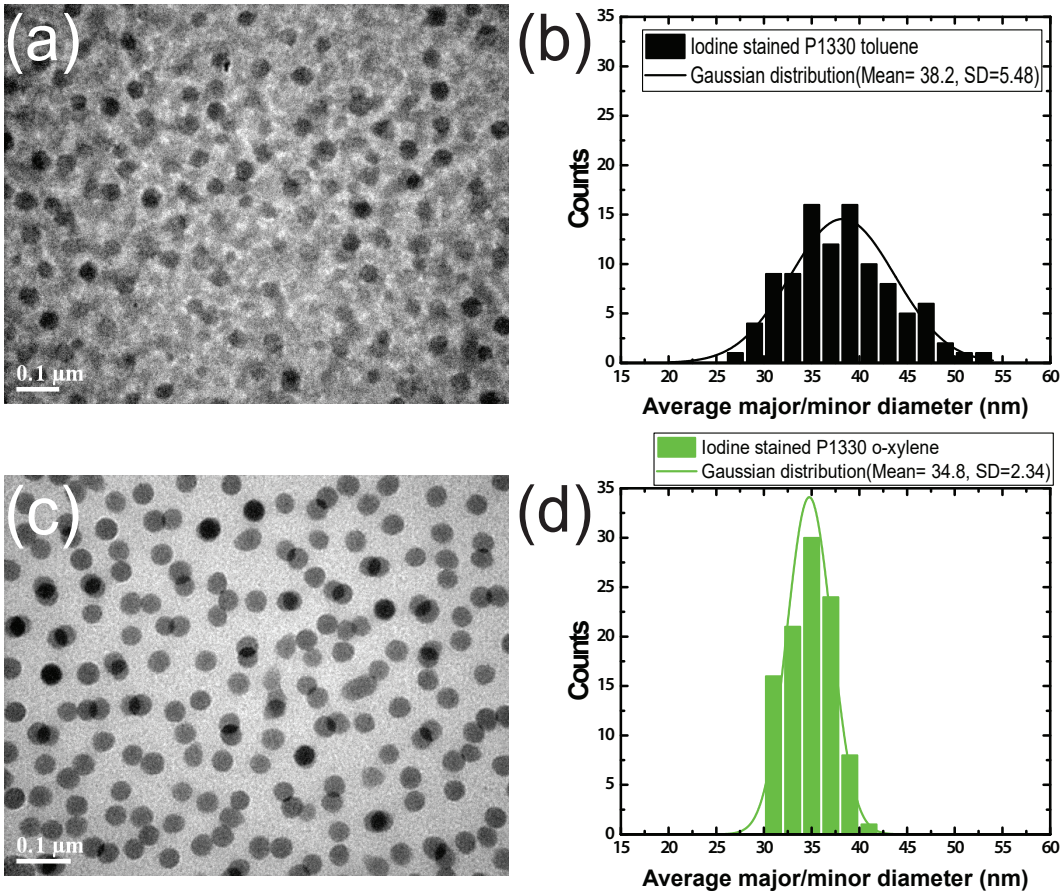

Figure 6.2: Iodine stained PS-*b*-P2VP(P1330) micelles with different solvent. TEM images of iodine stained P1330 micelles (a) in toluene and (c) in o-xylene; Core size histograms and the Gaussian distributions of P1330 micelles (b) in toluene and (d) in o-xylene.

The solvent is another essential factor for the formation of the micelles.[56, 59] Here, toluene and o-xylene, both the selective solvents for the PS block, were employed for the direct comparison of the P1330 core size. The concentration of the P1330 was kept the same using 3.00mg/ml for both toluene and o-xylene.

The core size distributions of the P1330 in toluene and o-xylene were obtained using the same procedures as described in last section. The mean size of the P1330 core in toluene and o-xylene were (38.2 ± 5.48nm) and (34.8 ± 2.34nm) respectively.

Interestingly, the PDI of the P1330 core in o-xylene was significantly decreased to 0.07, leading to a more uniform size distribution(Figure 6.2 (d)) compared to the toluene counterpart, despite the slightly smaller core size. This might have an influence on the size of the resultant nanoparticles, which will be discussed later.

6.3 The micelles array dispersion analysis

6.3.1 Different solvents

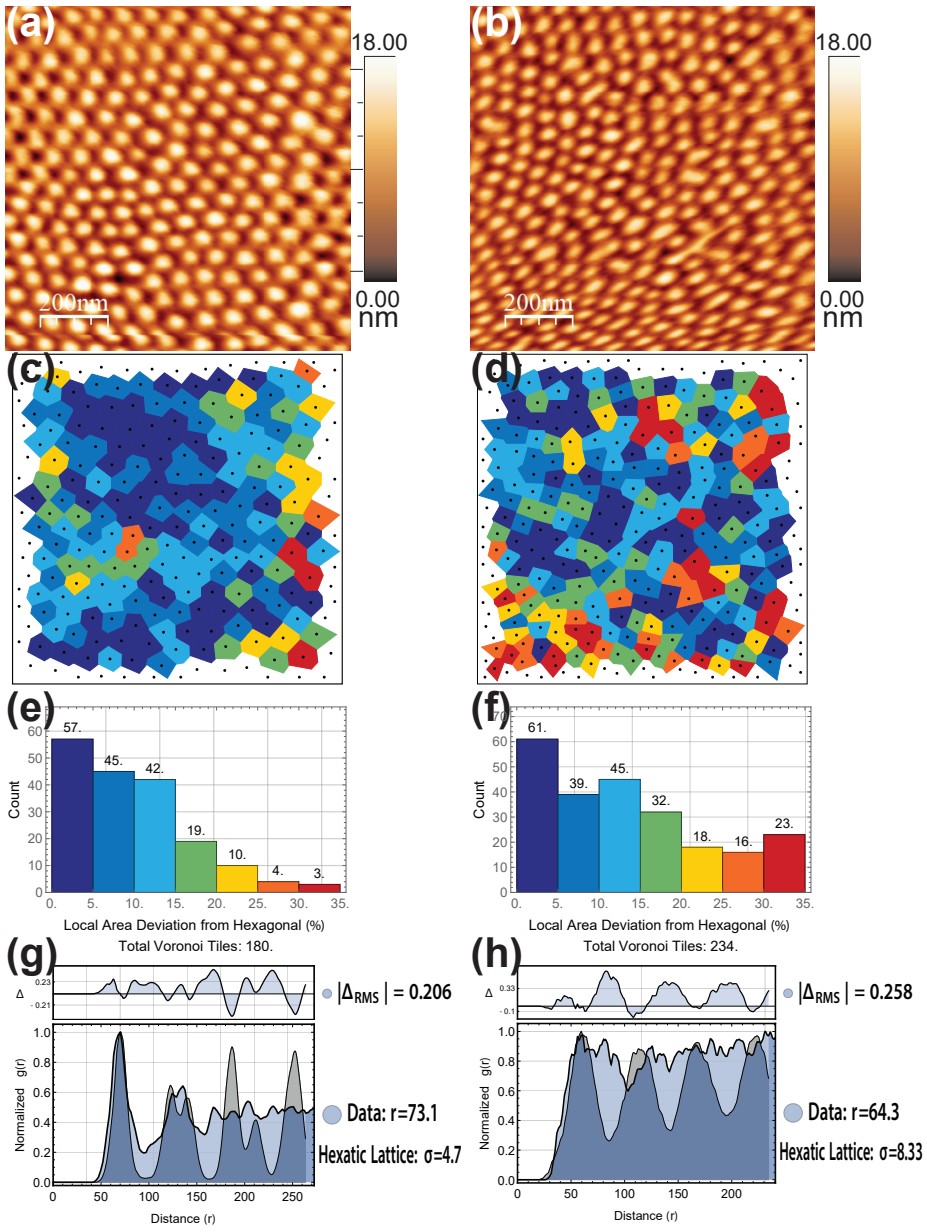

Figure 6.3: Dispersion comparison of PS-*b*-P2VP(P1330) micelles dissolved in o-xylene and toluene. AFM image of P1330 micelles in o-xylene (a) and toluene (b), and the corresponding Voronoi tessellation (c) and (d), Voronoi histogram of the local area deviation from hexagonal (e) and (f), pair correlation function (g) and (h).

In order to evaluate the dispersion of the micelles array, the P1330 was dissolved in toluene and o-xylene to yield 3.00mg/ml solutions respectively. After spinning for 24 hours, the micelles solutions were spin coated on the 1 by 1cm silicon substrates. The spin coating period was set to 45 seconds at 2000rpm spin speed using 4μ l solutions for the purpose of generating the monolayer micelles array.

Figure 6.3 (a) and (b) represents the typical AFM topography image of the micelles array from o-xylene and toluene solutions. By comparing the Voronoi tessellation and the corresponding histogram of the local area deviation from hexagonal, the micelles array from o-xylene solutions possesses a higher order of lateral distribution as only 9.4% of the Voronoi cells are above 20% deviation from hexagonal, whereas 24.4% of the Voronoi cells are above 20% deviation from hexagonal from toluene solutions(See Figure 6.3, (c) (e) and (d) (f)). The micelles array from toluene solutions yields a higher density of 234 micelles per $1um^2$, which is probably due to the faster solvent evaporation during spin coating(Vapor pressure at 20°C, toluene: 2.8kPa, o-xylene: 0.9kPa), leaving less time for the micelles to spread out. In addition, the pair correlation function (g(r)) in Figure 6.3(g) shows that the root mean square difference (Δrms) from the related hexagonal array in g(r) is 0.206 and the root mean square hexatic displacement (σ) is 4.7 from o-xylene solutions. Both are lower compared to that of the toluene solutions, again reinforcing a higher degree of order in micelles array with o-xylene. In addition, the nearest neighbor distance (r) of micelles array (o-xylene) is 73.1nm compared to the 64.3nm of micelles array (toluene), which is consistent with the lower density in micelles array from o-xylene. The pair correlation function difference of the micelles arrays from toluene and o-xylene is also plotted in Figure 6.4 for direct comparison. The results are similar as indicated in Figure 6.3.

Combining the Voronoi tessellation and pair correlation function analysis, we can conclude that the micelles array from o-xylene solutions yields a higher degree of lateral order.

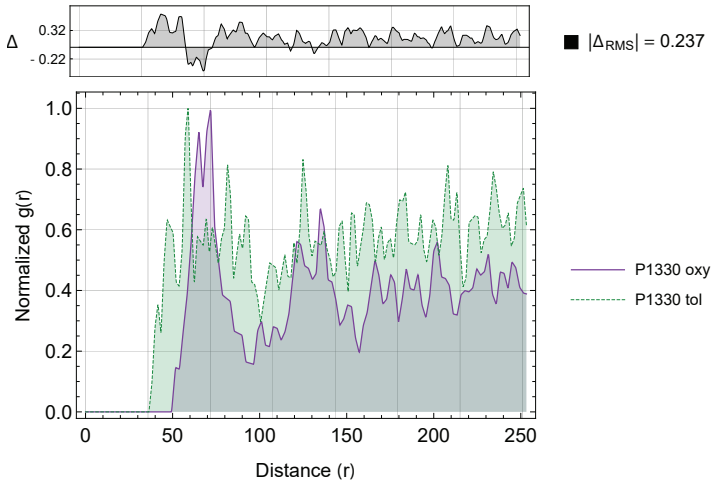

Figure 6.4: Pair correlation function difference of P1330 micelles array from toluene and o-xylene.

6.3.2 Different spin coating speeds

2

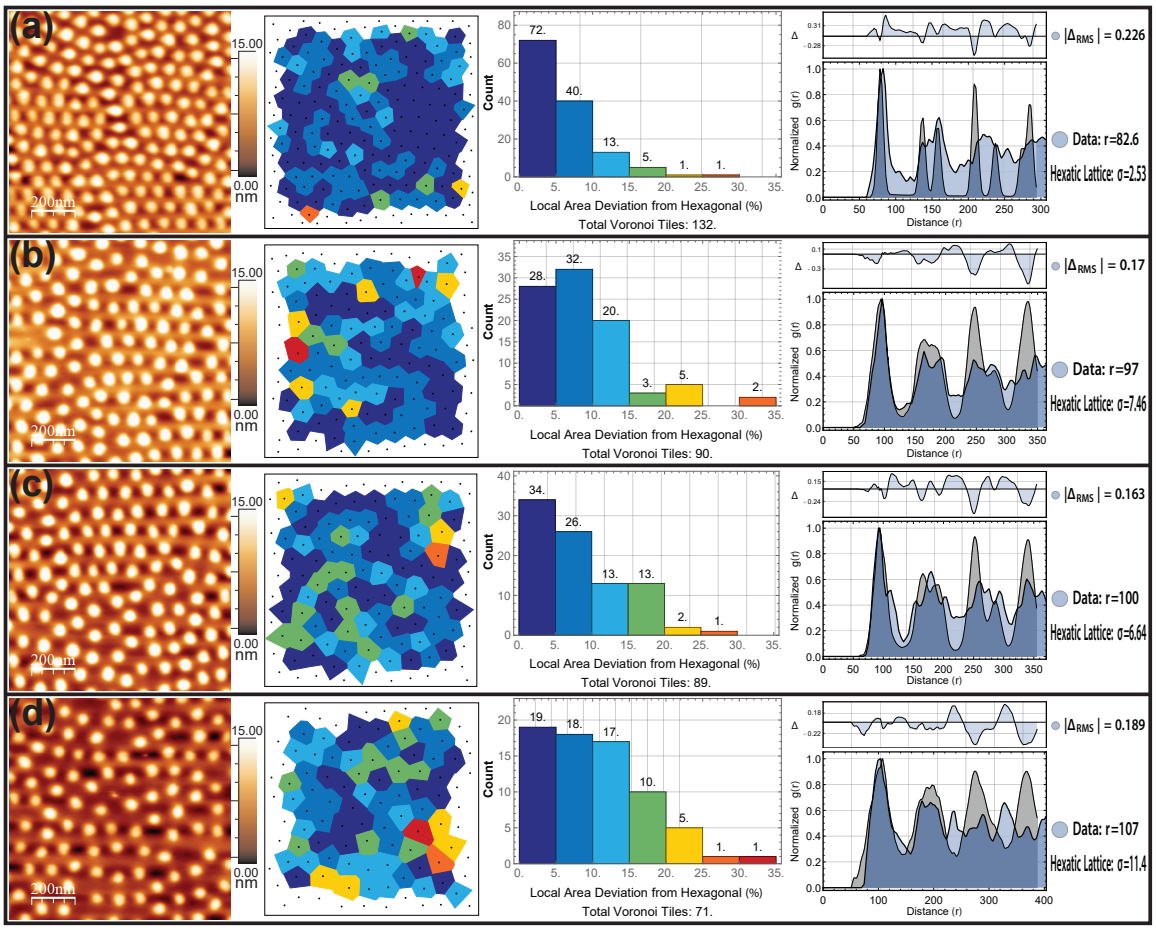

Figure 6.5: Dispersion comparison of P1330 micelles dissolved in o-xylene(3.00mg/ml) with varying spin speed. AFM topography, Voronoi tessellation, histogram of local area deviation from hexagonal and pair correlation function of (a) 2000rpm, (b) 4000rpm, (c) 6000rpm, (d) 8000rpm.

When spin coating is applied to deposit the material, the spin coating speed is considered as a convenient parameter to control the final thickness of the materials due to the difference in centrifugal force. The same idea could be applied to changing the dispersion of the monolayer micelles. In this case, the solution was 3.00mg/ml

[2]Parts of this section were published in Bumstead, M., Liang, K., Hanta, G., Hui, L. S., Turak, A. (2018). disLocate: tools to rapidly quantify local intermolecular structure to assess two-dimensional order in self-assembled systems. Scientific reports, 8(1), 1554.

P1330 in o-xylene because of the better dispersion as shown in last section. It was also reported that the micelles dissolved in toluene tend to pack closely due to the fast evaporation of toluene, which was not influence by changing the spin coating speed.[65] Four spin coating speeds: 2000rpm, 4000rpm, 6000rpm and 8000rpm were employed in this study. The AFM topography image and corresponding Voronoi tessellation, histogram and pair correlation function (g(r)) of the micelles arrays from different spin coating speeds can be seen in Figure 6.5. The density of the micelles decreases with increasing spin coating speed, which is consistent with the increasing nearest neighbor distance (r) in the corresponding g(r). Comparing the Voronoi cells and histogram of local area deviation from hexagonal between these four spin-coating speeds, the local dispersion does not decay with the increasing spin coating speed. In addition, the differences of pair correlation functions for four different speeds are shown in Figure 6.6, showing the first peak shift towards larger distance with increasing speed.

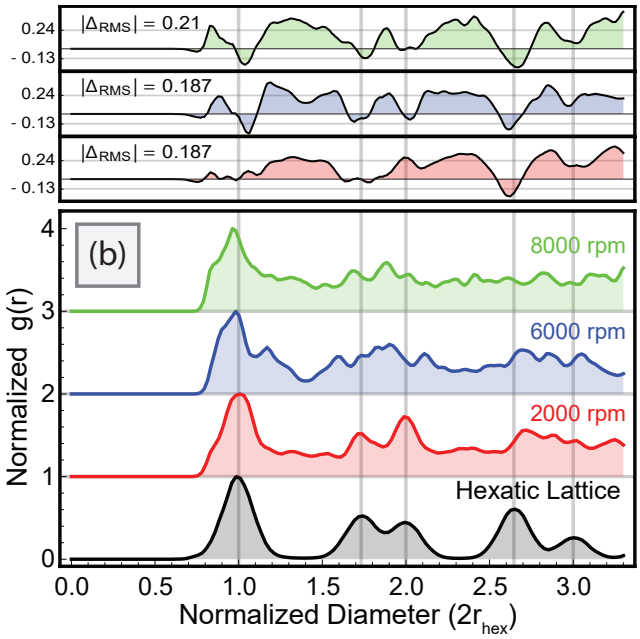

Figure 6.6: Pair correlation function difference of various spin speeds compared to the 2000rpm data set.

According to the above disLocate analysis, changing the spin speed offers the convenient way to alter the separation and thus the density of the micelles(P1330 o-xylene) while maintaining high degree of lateral order.

6.3.3 Different PS-*b*-P2VP concentrations

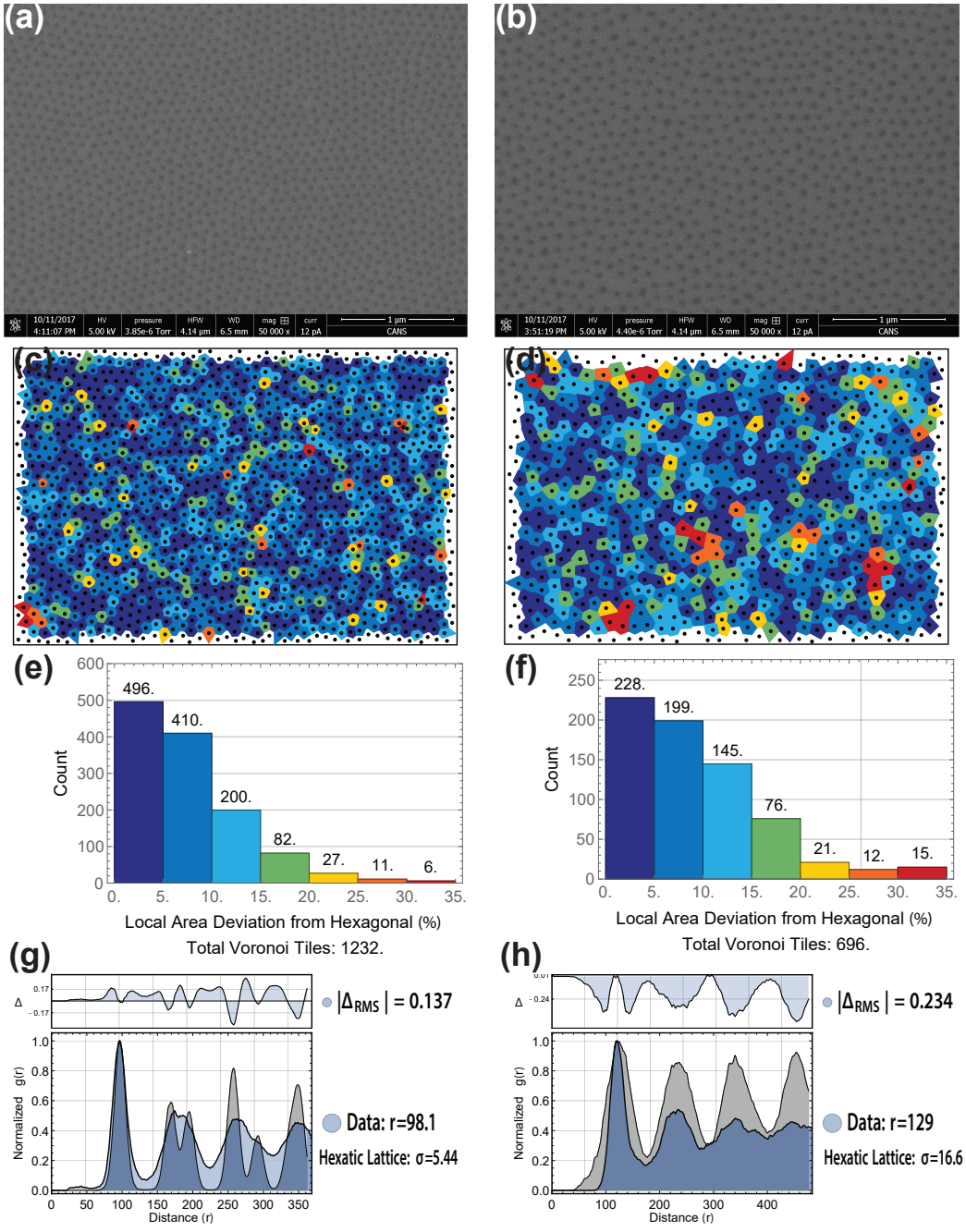

Figure 6.7: Dispersion comparison of P4824 micelles dissloved in o-xylene with different concentrations. 3.75mg/ml: (a) SEM image, (c) Voronoi tessellation, (e) histogram of local area deviation from hexagonal and (g) pair correlation function; 3.00mg/ml: (b) SEM image, (d) Voronoi tessellation, (f) histogram of local area deviation from hexagonal and (h) pair correlation function.

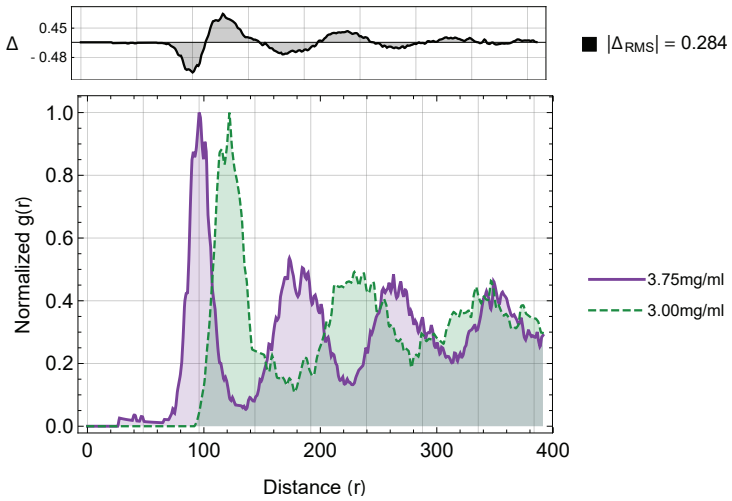

Figure 6.8: Pair correlation function difference for two micelles concentrations with reference with 3.00mg/ml data set

The concentration of the P4824 using o-xylene as a solvent was also investigated to see how it affects the dispersion. In this study, the spin coating speed was 2000rpm for 45s coating duration. Two different concentrations, 3.00mg/ml and 3.75mg/ml, were chosen, which were within the range where the size of micelles could remain unchanged.[98] As shown in Figure 6.7, raising the concentration of the diblock copolymer from 3.00mg/ml to 3.75mg/ml resulted in significant difference for the micelles density. The number of micelles for 3.75mg/ml solutions was 109 micelles per $/mu\text{m}^2$ in SEM image, which is around 1.8 times of that for 3.00mg/ml solutions. Both micelles arrays yielded a decent hexagonal dispersion as indicated by the Voronoi tesselations and the corresponding histograms of local area deviation from hexagonal, showing more than 90% of the micelles were within 20% deviation from the related hexagonal array. From pair correlation function g(r) perspective, the expected first neighbor distance (r) in g(r) was decreased to 98.1nm with 3.75mg/ml solution from 129nm with 3.00mg/ml solution, supporting the density difference in these two cases. In addition, Figure 6.8 gives the direct comparison of the pair correlation functions, showing a clear shift of the peaks towards smaller distance with a higher concentration P4824 solution.

Therefore, the average distance of the micelles(P4824 o-xylene) can be changed easily by changing the concentration of the diblock copolymer without causing a decrease in lateral order.

6.4 The nanoparticles array dispersion analysis

6.4.1 Changing the solvent and PS-*b*-P2VP

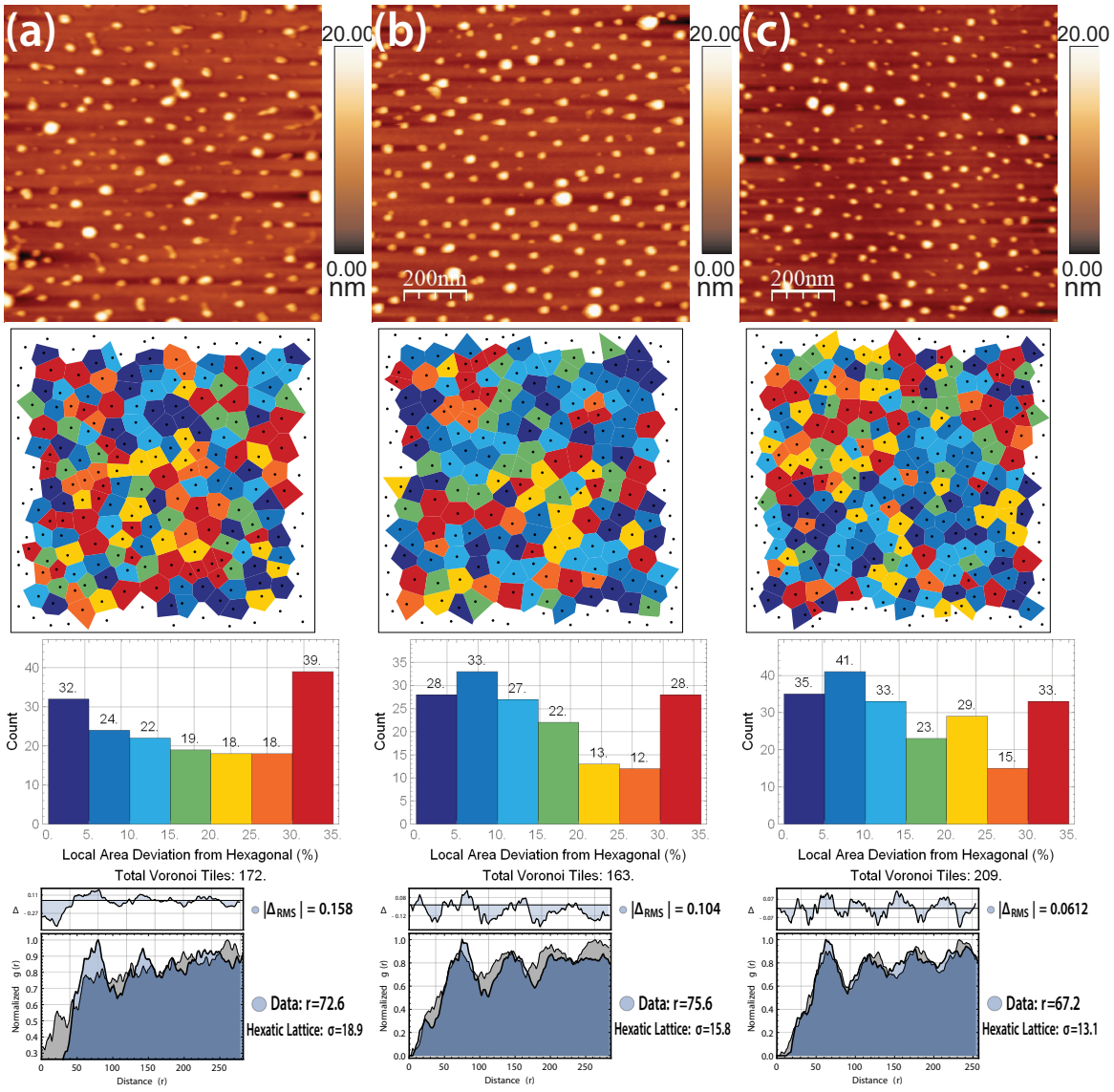

Figure 6.9: Dispersion comparison of iron oxide nanoparticles. Note that the PS-*b*-P2VP concentration was 3.00mg/ml and the $FeCl_3$ loading ratio was 0.2. (a) P4824 toluene solution, (b) P4824 o-xylene solution, (c) P1330 o-xylene solution.

After loading $FeCl_3$, the resultant loaded micelles and iron oxide nanoparticles could yield a different dispersion compared to the empty micelles themselves, due to the $FeCl_3$/P2VP interaction as described in section 2.2.2. Here, the dispersion comparison was carried out for nanoparticles arrays from P4824 0.2 $FeCl_3$ loading ratio in toluene or o-xylene. The results can be seen in Figure 6.9 (a) and (b), similar to the empty micelles dispersion outcome as described in section 6.3.1. Although the Voronoi tessellation shared similar features, the nanoparticles arrays from o-xylene solutions possessed a lower root mean square difference (Δrms) from the corresponding hexagonal array in the pair correlation function g(r) as compared to that from the toluene solutions, revealing a higher lateral order of the nanoparticles. Also, the density of nanoparticles was slightly higher when using toluene as a solvent, showing a similar result as that of the empty micelles.

In addition, when using the same solvent (o-xylene), the average distance between the nanoparticles was changed using PS-*b*-P2VP with different block length as indicated by the change in nearest neighbor distance (r) in g(r) of Figure 6.9 (b) and (c). As the PS block of P1330 is much shorter than that of P4824, the thickness of the corona is smaller in P1330, indicating less seperation for the resulted nanoparticles, which is again supporting the decrease of r in g(r).

The spin coating speeds and the concentration of the PS-*b*-P2VP could also be used to change the density/average distance of the resulted nanoparticles, which was expected to yield a similar results as that of the empty micelles in section 6.3.2 and 6.3.3. However, unlike the empty micelles, the regional dispersion was deteriorated in the nanoparticles cases, showing a higher local area deviation in the Voronoi tessellation. Hence, other methods were required to improve the order of the nanoparticle array.

6.4.2 Co-solvents effect

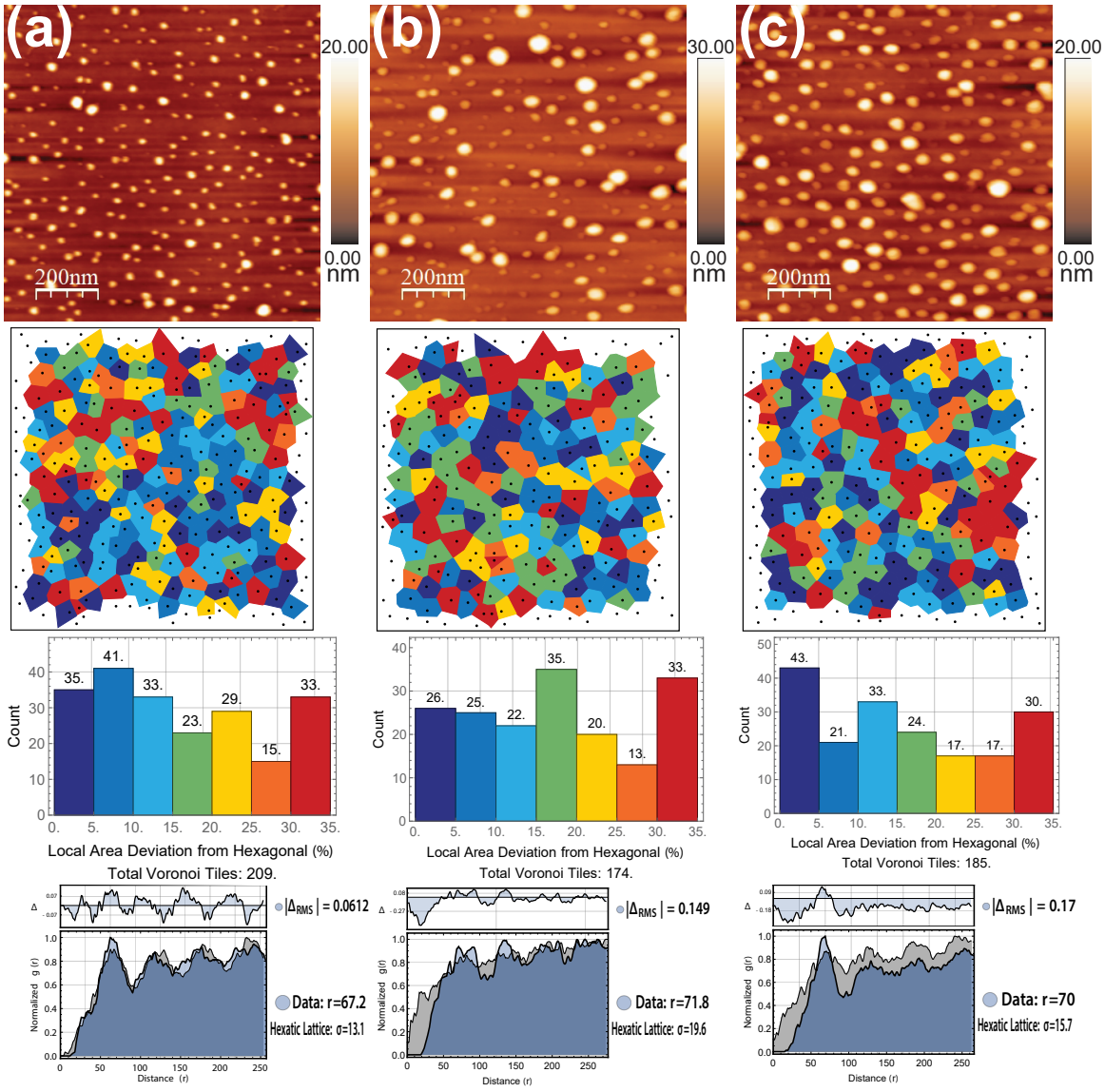

Figure 6.10: Dispersion comparison of iron oxide nanoparticles with and without co-solvent. Note that the P1330 concentration was 3.00mg/ml. (a) 0.2 ratio $FeCl_3$ loading, (b) 0.2 ratio $FeCl_3$ loading with additional methanol co-solvent(10ul to 1ml o-xylene), (c) 0.2 ratio $FeCl_3$ loading with additional ethanol co-solvent(10ul to 1ml o-xylene).

Adding a small volume of appropriate co-solvents into the loaded PS-*b*-P2VP micelles could be introduced to fine-tuning the morphology of the micelles arrays and hence

improve the lateral order of the resultant nanoparticles.[124] In this study, ethanol and methanol were selected for the purpose of tuning the dispersion of the nanoparticles

The co-solvents were applied to tune the dispersion of the nanoparticles array, following the processes in section 6.1.2. Figure 6.10 shows the related AFM images and the corresponding disLocate dispersion analysis. By comparing the Voronoi tessellation and the local area deviation histogram, neither adding methanol nor ethanol could improve the local order as more than 30% of the voronoi cells are above 20% deviation from the hexagonal, showing the similar dispersion behavior as their direct loading counterpart. From the pair correlation function (g(r)) perspective, the lateral order decays to a certain extent as indicated by the larger root mean square difference (Δrms) from the corresponding hexagonal array in the g(r) for adding co-solvent compared to the g(r) of the direct loading, while the first nearest neighbor distances (r) are roughly the same. According the above disLocate analysis, the methanol and ethanol were not suitable to be applied to the $FeCl_3$/P1330 systems for the purpose of improving the lateral order of the resulted nanoaprticles.

6.4.3 Poly(2-vinyl pyridine) homopolymer assisted loading

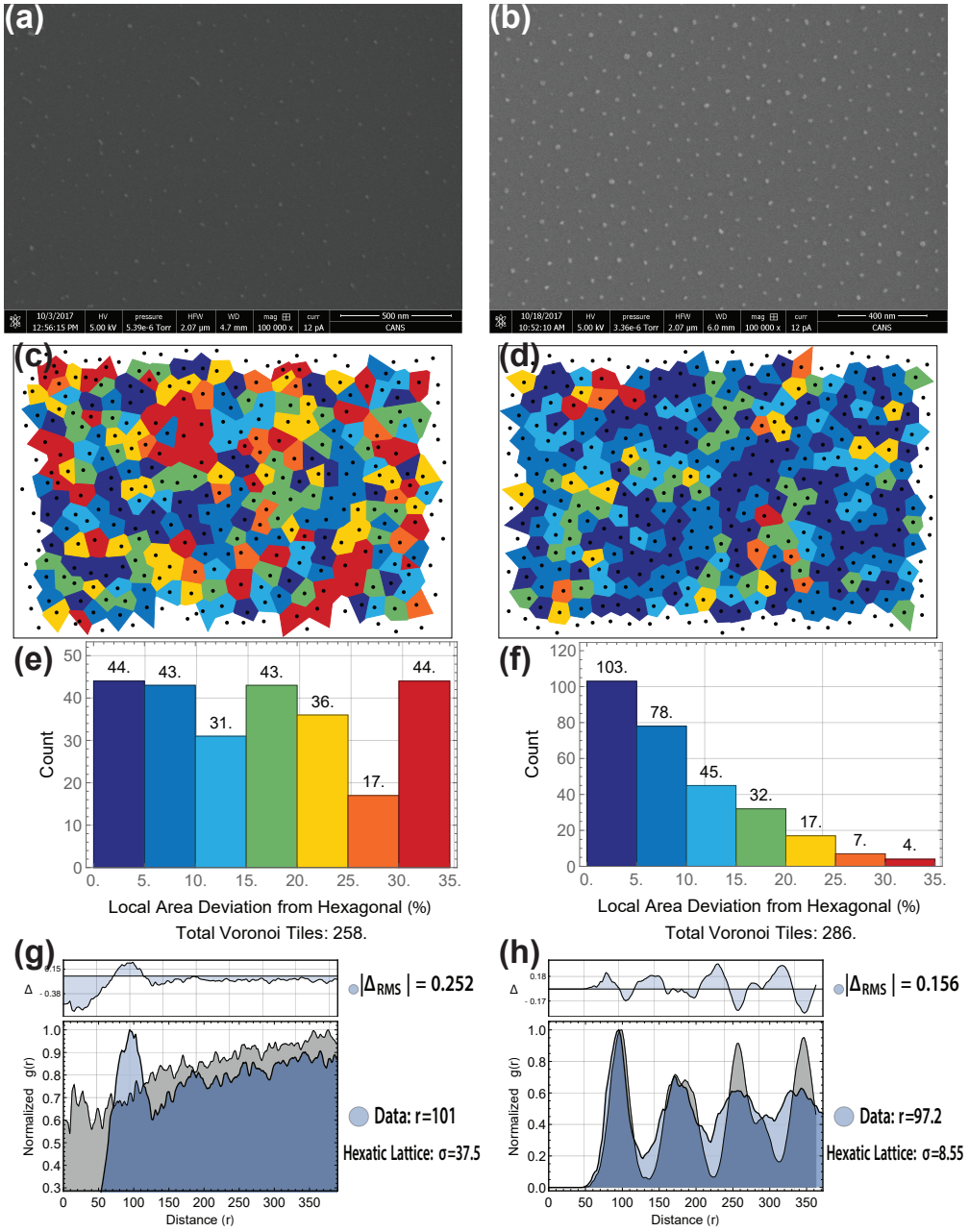

Figure 6.11: Dispersion comparison of iron oxide nanoparticles from HP2VP assisted loading of P4824 in toluene and o-xylene. Note that the loading ratio is 0.3 with respect to 2VP in HP2VP. Nanoparticles from toluene solutions: (a) SEM image, (c) Voronoi area deviation, (e) histogram of Voronoi area deviation, (g) pair correlation function. Nanoparticles from o-xylene solutions: (b) SEM image, (d) Voronoi area deviation, (f) histogram of Voronoi area deviation, (h) pair correlation function.

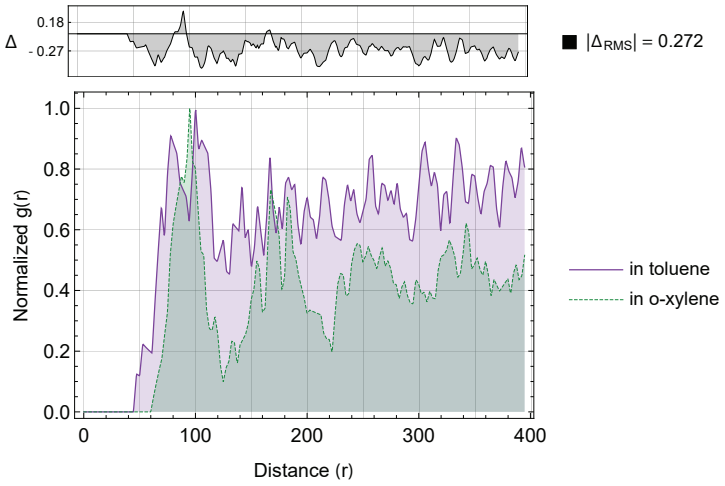

Figure 6.12: Pair correlation function difference of HP2VP assisted loading of P4824 in toluene and o-xylene with o-xylene data set as reference.

The over-loading of $FeCl_3$ into PS-*b*-P2VP reverse micelles has been reported to result in bad dispersion of the resultant nanoparticles.[68] As described in Chapter 4, the $FeCl_3$ can interact with 2VP units, so there could be a saturation limit for loading, above which could affect the micelles structure and thus jeopardize the control over the size and dispersion of the following nanoparticles.

Here, the nanoparticles arrays were generated as indicated in section 6.1.3. As seen in the left column of Figure 6.11, the HP2VP assisted loading of the P4824 micelles did not significantly improve of the local order for the nanoparticles when using toluene as solvent, compared with the previous results of direct loading. Specifically, by looking at Figure 6.11 (c) and (e), around 36% of Voronoi cells possesses more than 20% local area deviation with relatively even distribution from 0% to 35% local area deviation when using toluene as a solvent, which shares similar features as the voronoi cells from the previous direct loading or adding co-solvents.

In contrast, using o-xylene as solvent, iron oxide nanoparticles array had a significant improvement in the Voronoi tessellation, using the same iron precursor loading ratio, HP2VP concentration and P4824 concentration. 90% of Voronoi cells were within 20% local area deviation with only a few Voronoi cells possessing more than 30% local area deviation, indicating a high degree of local order. Additionally, the pair

correlation function (g(r)) also showed a significant difference. The root mean square difference (Δrms) from the corresponding hexagonal array in the g(r) is significantly lower in o-xylene case, reinforcing the higher degree of lateral order. The pair correlation function difference is also plotted in Figure 6.12 for direct comparison, showing a long-range order in the o-xylene case. In addition, the average distance between nanoparticles is similar in both HP2VP assisted loading, but is obviously larger than that of the previous direct loading. This might be caused by the change of micelles core/corona by addition HP2VP. Moreover, the size of the resultant nanoparticles from HP2VP assisted loading was significantly smaller than that of the direct loading(detail can be see in table 6.1 in section6.5), probably causing by the fact that the HP2VP also occupy the space in the core of reverse micelles.

Hence, using o-xylene as a solvent, the HP2VP assisted loading could be used to generate a high lateral order nanoparticles arrays.

6.5 Size control of the iron oxide nanoparticles

[3]

6.5.1 Size control experimental

We also tested the size of the resulted iron oxide nanoparticles by using only P4824(3mg/ml in toluene) reverse micelles with different $FeCl_3$ loading ratio (the number of the Fe^{3+} ion divided by the number of the 2VP units in PS-*b*-P2VP). The reverse micelles formation and $FeCl_3$ was described in section 3.2.2. In this experiment set, the loaded micelles solutions were created with the loading ratios of 0.05, 0.10, 0.15, 0.20, 0.30, 0.45, 0.60 and 0.70. The solutions were kept stirring for at least 24h to allow adequate precursor infiltration. After that, the loaded micelles arrays with different loading ratio were prepared on 1cm by 1cm Si substrates by spin-coating(4ul volume, 2000rpm, 45s) for quantum nanomechanical mapping(QNM) by AFM. After that, the samples were treated with O_2 plasma(29.6W, 25mins) to produce the iron oxide nanoparticles

[3]Results from this section submitted as "G. Hanta, K. Liang, A. Turak, "Young's Modulus variations to track loading precursor salts in reverse micelles", Langmuir"

for further AFM characterization to determine their sizes.

Additionally, homopolymer poly(2vinyl pyridine)(HP2VP) was applied to our reverse micelles systems to investigate how it affects the size of the resulted nanoparticles. In this route, the $FeCl_3$ was mixed with 6 mg HP2VP in 1ml toluene in a vial while 15 mg PS-*b*-P2VP was dissolved in 4 ml toluene in a separate vial. After continuous stirring for 72 hours, these two solutions were mixed together yielding the same PS-*b*-P2VP concentration as we used before, and then the mixtures were stirred for 7 days. The loading ratio was determined by the molar ratio of $FeCl_3$ to the 2VP units of HP2VP in this case. Two loading ratios (0.30 and 0.53) using P4824 and one loading ratio (0.30) using P1330 were fabricated for comparison. The corresponding nanoparticles samples were prepared by the same procedures as described in the above paragraph.

AFM was done using a Bruker Bioscope Catalyst with an RTESPA probe. The probe was selected to match the range of elastic modulus we were investigating based on the recommendation from Bruker. For each measurements, the probe was calibrated using a relative method of calibration from a sample of known modulus. The calibration first involves the calculation of the deflection sensitivity by ramping the probe onto a clean sapphire substrate provided by Bruker. A minimum of three ramps were done and the average deflection sensitivity was used. The probe was then withdrawn from the substrate and a thermal tune was performed to calculate the spring constant. Lastly, a polystyrene sample of known modulus provided by Bruker is loaded and imaged. The tip radius is adjusted until the measured modulus agrees with the known modulus. AFM images were taken on a scale of 1 μm x 1 μm and at a scanning rate of 0.5 Hz.

AFM images were analyzed in WSxM[99]. The elastic modulus was determined by taking a line profile through 100 micelles by matching the coordinates in the topography channel to the elastic modulus channel. The schematic of how to extract the modulus can be seen in Figure 6.13. The elastic modulus for each micelle was determined by taking the average of the centre points of the line profile. The number of points averaged to determine the modulus varied due to a range in the size of micelles measured. However, typically 10 points were taken. The modulus measurements for each micelle were fitted using a Gaussian approximation to calculate the average modulus value and error for each treatment.

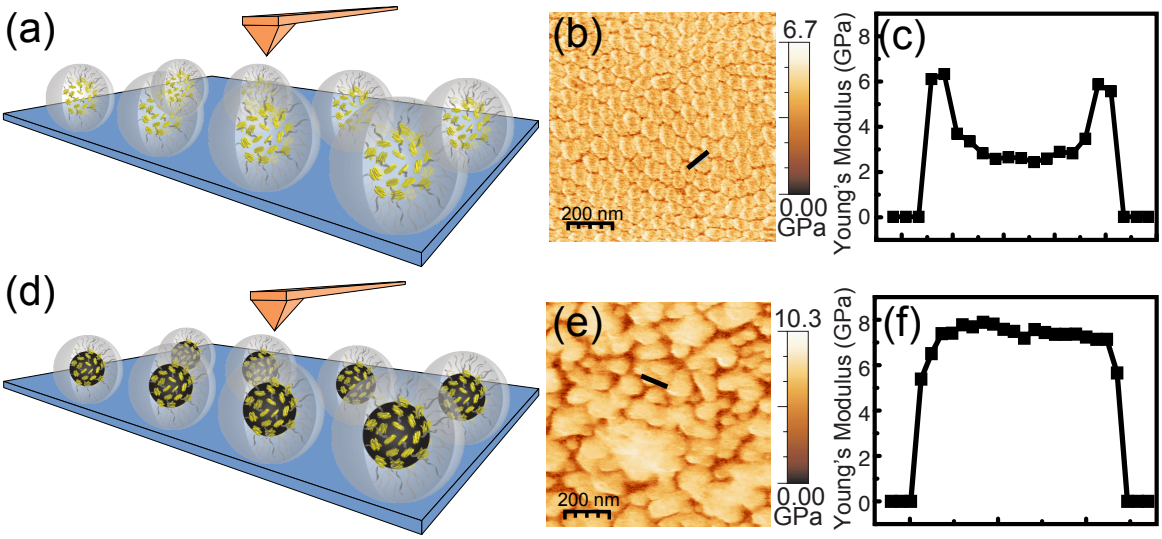

Figure 6.13: Schematic showing AFM procedure for quantum nanomechanimcal (QNM) mapping. (a) and (d): schematic of the empty and loaded micelles; (b) and (e): AFM images of empty and loaded micelles with line corresponding to the Young's modulus line profile in (c) empty and (f) loaded micelles.

6.5.2 size control discussion

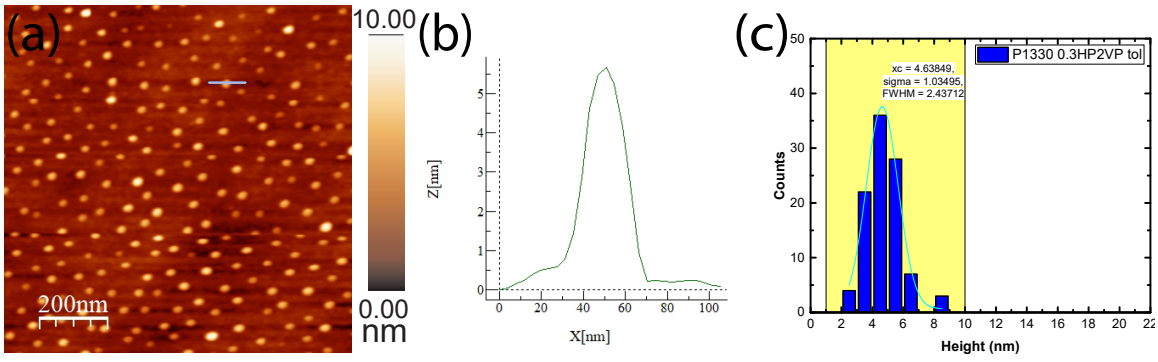

Figure 6.14: The illustration for average height determinations of the nanoparticles. (a) AFM of a typical spin-coated nanoparticles array on Si substrates, (b) The height profile of a single nanoparticles, (c) The height histograms with Gaussian fitting.

The average size of the nanoparticles was obtained from the height profiles of nanoparticles in AFM images by the help of WSxM.[99] One hundred randomly selected height

profiles were analyzed to acquire a the statistical representation.[110] Moreover, a Gaussian function was then applied to the raw data in order to minimize the influence of the small and large anomalies. The overall processes were shown in Figure 6.14.

Representative AFM images of the nanoparticles related to different loading ratios were listed together in Figure 6.15, with the homopolymer assisted loading conditions labelled in white from (i) to (k). Following the same size determination procedures, the average size of the nanoparticles were summarized in table 6.1 along with their standard deviations(SD) and polydispersity indices(PDI). Here the PDI was defined as the ratio between the standard deviation and the related average height. Observing the average height only, it increased as the loading ratio was raised till 0.45. However, the density of the nanoparticles went up with loading ratio higher than 0.30 as shown in Figure 6.15 (e) to (h). Table 6.1 summarized the average height with SD of the different loading ratios and also the PDIs. In addition, the average nearest neighbor distance between the nanoparticles (r in the g(r)) and the lattice disorder parameter (σ in g(r)) were also listed in the same table.

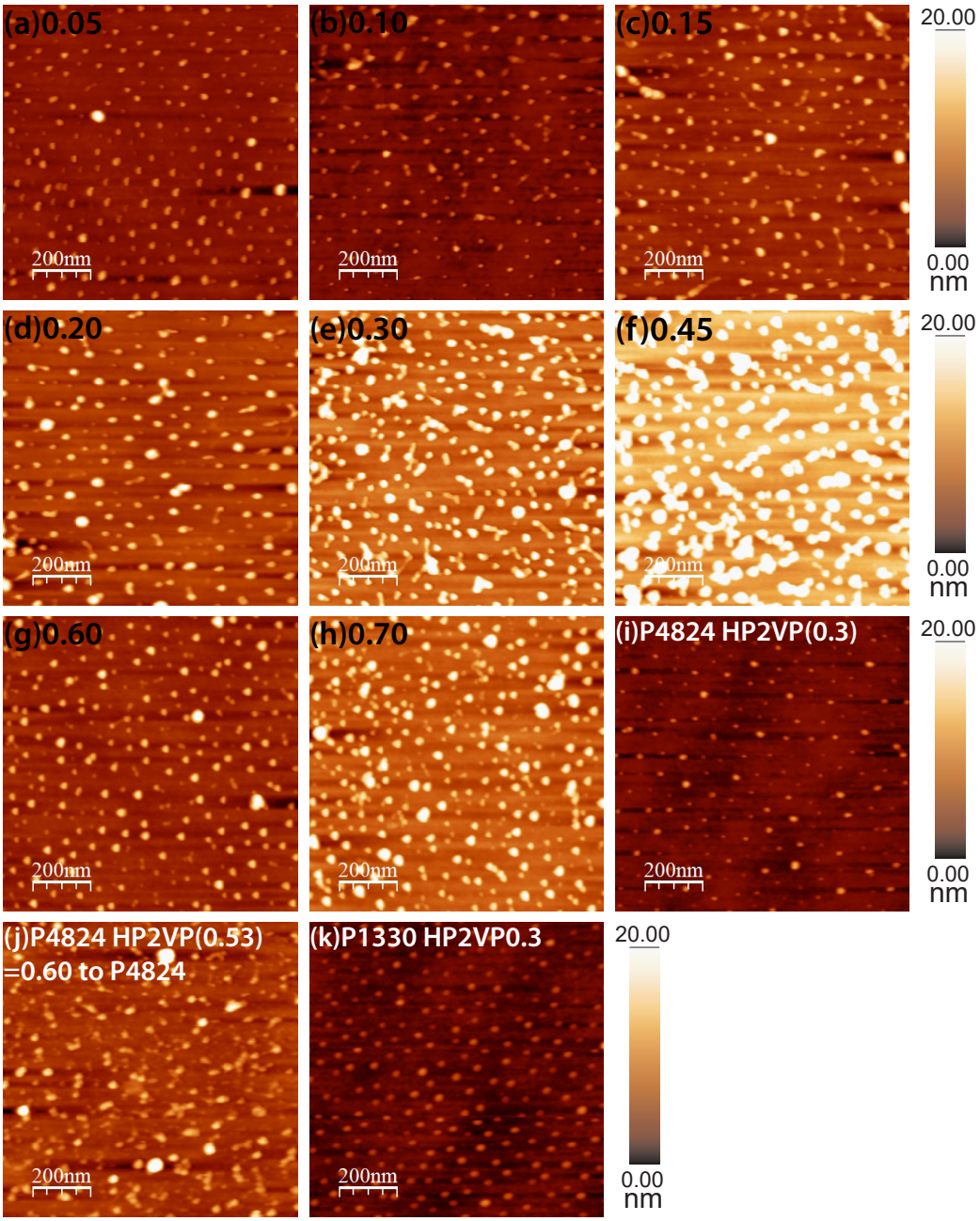

Figure 6.15: Representative AFM images of nanoparticles with different loading ratio.

Using one type of PS-*b*-P2VP, the size of the nanoparticles could be tuned to a certain degree by simply varying the loading ratio of the $FeCl_3$. According to table 6.1, the height of the nanoparticles seemed to peak at 0.45 loading ratio. Exceeding that loading ratio resulted in smaller nanoparticles with decreased nearest neighbor distance,

Table 6.1: Summary of average heights and polydispersity indexes for different $FeCl_3$ loading ratios using P4824 in toluene solvent

Loading Ratio	Average Height (nm) ± SD	PDI	Nearest Neighbor Distance (nm)
0.05	6.5 ± 0.66	0.10	51.2
0.10	6.0 ± 1.50	0.25	54.8
0.15	7.2 ± 2.47	0.34	48.5
0.20	7.0 ± 2.74	0.39	53.9
0.30	11.0 ± 3.19	0.29	42.9
0.45	13.0 ± 2.41	0.19	43.7
0.60	8.1 ± 1.99	0.25	45.6
0.70	9.4 ± 7.22	0.77	39.6
P1330-HP2VP(0.30)	4.6 ± 1.03	0.22	53.1
0.34-HP2VP(0.30)	3.5 ± 0.75	0.21	57.6
0.60-HP2VP(0.53)	6.3 ± 1.66	0.26	N.A.

indicating a change in dispersion. It suggested that there should be a maximum loading limit of the $FeCl_3$.

The loaded micelles were characterized using QNM to extract the Young's modulus, showing the relation between the loading ratio and the relative Young's modulus. Figure 6.16 shows the QNM results together with the schematic depicting the $FeCl_3$/P2VP interaction.

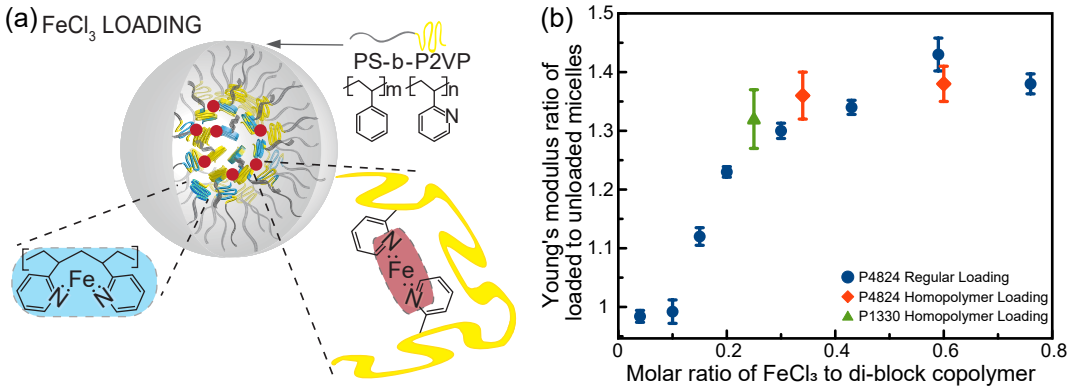

Figure 6.16: (a)$FeCl_3$ incorporated into the micellar core by binding along the P2VP block backbone and connecting adjacent P2VP blocks, leading to an increase in Young's modulus, (b) the Young's modulus ratio of the loaded micelles to empty micelles.

Comparing the Young's modulus ratio of the regular loading(direct loading) in Figure 6.16 (b), it increases rapidly from 0.1 to 0.2 loading ratio, indicating an increase in loading. After 0.3 loading ratio, the increase in Young's modulus becomes insignificant and begins to level off after 0.45 loading ratio, indicate a maximum infiltration at this point. The use of homopolymer appears to have led to an earlier maximum infiltration. This is consistent with the AFM height results in table 6.1 showing the maximum height at 0.45 loading ratio. Moreover, the QNM measurements of the homopolymer HP2VP assisted loading can also be seen in Figure 6.16 (b). In this case, the HP2VP appears to have smaller maximum infiltration, as the Young's modulus begins to flatten at below 0.3 loading ratio. This could be a explanation on why the size of the nanoparticles in HP2VP assisted loading was significantly smaller than the direct loading. Additionally, the HP2VP could occupy the space inside the micelles' core, decreasing the actual amount of $FeCl_3$ in that region, which again lead to the smaller resulted nanoparticles.

In summary, we could changed the loading of $FeCl_3$ to tune the size of the resulted iron oxide nanoparticles under the maximum loading ratio which is around 0.45 for direct loading.

6.5.3 Size effect on the magnetization-applied magnetic field curves of the monolayer iron oxide nanoparticles array

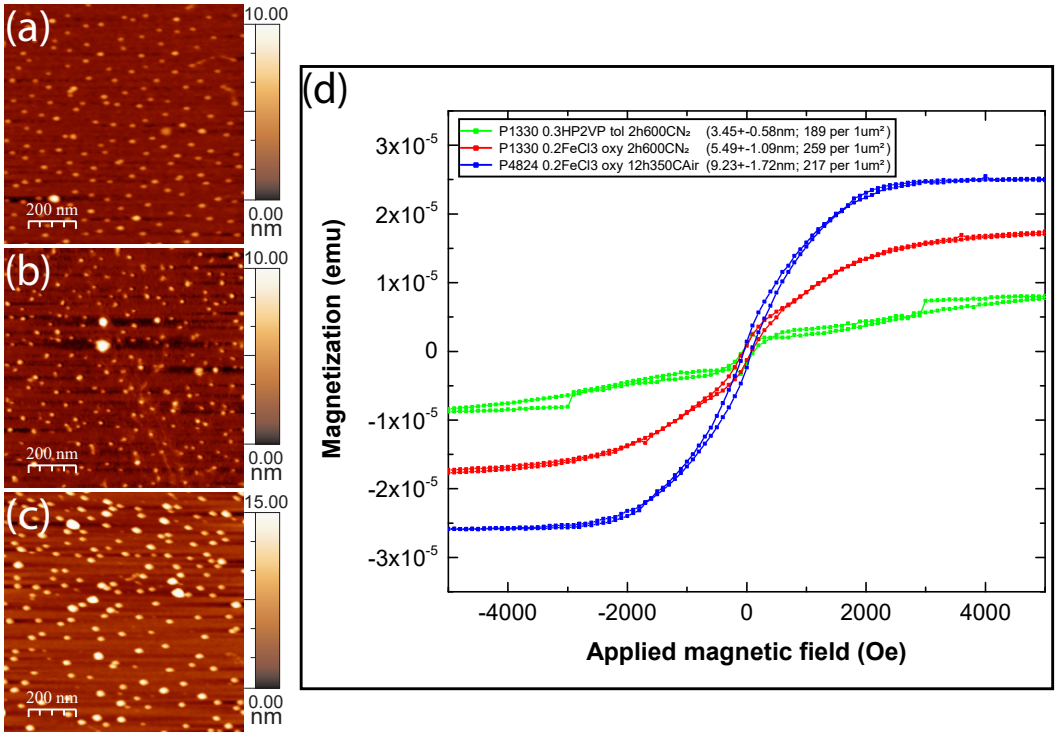

Figure 6.17: Comparison of M-H curves with varying the size of iron oxide nanoparticles. AFM images of SQUID samples-single layer iron oxide nanoparticles on Si with different mean height: (a) 3.45±0.58nm, (b) 5.49±1.09nm, (c) 9.23±1.72nm; (d)M-H curves of the related SQUID samples.

The magnetization-applied magnetic field (M-H) curves of 3 different averaged heights iron oxide nanoparticles arrays were measured at 300K using SQUID. The average heights of nanoparticles were calculated from 100 randomly picked nanoparticles in the corresponding AFM images(Figure 6.17(a), (b) and (c)) to acquire an accurate representation of the height.[110] Figure 6.17(d) shows the M-H curves of three SQUID samples with 3.45±0.58nm (in green), 5.49±1.09nm (in red) and 9.23±1.72nm (in navy) nanoparticles respectively. The corresponding coercive field (H_c) was all at around 50Oe extracted from the M-H curves. The H_c was relatively small which was below the applied field increment(100Oe). In addition, the remanence magnetization (M_r) were extremely small in all three cases in the order of the

10^{-7} emu region, which was approaching the detection limit in the SQUID measurement.

Three M-H curves were also normalized by their height and density from the related AFM analysis, shown in Figure 6.18. The normalized saturation magnetization(M_s) converges to a similar magnitude at relatively high field strength at 5000Oe, but showing different responses on the low field strength region. The normalized magnetization of the sample with 9.23±1.72nm nanoparticles appears to saturate at lower field strength compared to that of the smaller size nanoparticles. This phenomenon could arise from the higher ratio of the surface atoms. Due to the incomplete coordinations and broken exchange bonds on the surface, surface magnetic anisotropy affect the saturation magnetization, decreasing the M_s. [50–53]

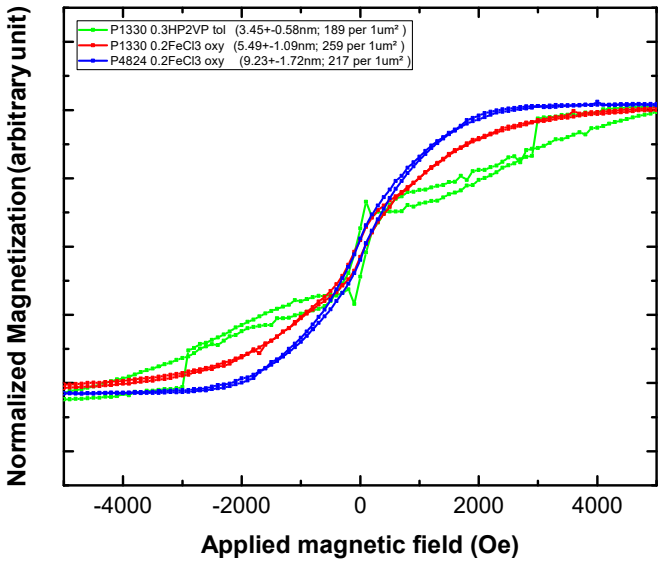

Figure 6.18: M-H curves normalized by the average height and density of the nanoparticles.

6.6 Summary

In this chapter, the micellar core size of different PS-*b*-P2VP was determined using toluene as a solvent, showing that P1330 micelles possessed larger average core size than that of P4824 micelles. The cores of P1330 micelles appeared to be slightly

smaller and also yielded a smaller PDI when using o-xylene as a solvent. Moreover, the dispersion of the empty micelles have been examined, showing a higher degree of lateral order in o-xylene. The average first nearest neighbor distance of the micelles can be altered by spin coating speeds and diblock copolymer concentration. However, the dispersion of the nanoparticles decayed compared to the empty micelles. In this case, homopolymer poly(2-vinyl pyridine) assisted loading improved the lateral order of the nanoparticles, whereas the methanol and ethanol co-solvents seemed to have negligible impact on the dispersion. Moreover, tuning the size of the nanoparticles was also achieved by changing the loading ratio of $FeCl_3$ under the maximum loading, using different PS-*b*-P2VP and applying poly(2-vinyl pyridine) assisted loading. The M-H curves of several selected size monolayer iron oxide nanoparticles were collected to reveal their magnetic properties, indicating the size dependence of the saturation magnetization.

Chapter 7

Conclusion and outlook

7.1 Conclusion

This thesis focused on developing a simple magnetic γ-Fe_2O_3 nanoparticles synthesis processes with a high degree of control over the size and dispersion with the help of di-block copolymer reverse micelles. By using Raman spectra, the iron oxide nanoparticles evolution processes was elucidated in detail in Chapter 4. The overall processes could be described as: **a.** Formation of the PS-*b*-P2VP reverse micelles; **b.** Adding $FeCl_3$ precursor; **c.** Dispensing (spin coating and dip coating); **d.** Oxygen plasma treatment; **e.** Annealing treatment. Importantly, the low temperature annealing condition was also developed for the purpose of incorporating into the actual organic electronic devices.

Moreover, the compositional and structural information of individual nanoparticles were also characterized thoroughly with TEM/STEM equipped with EDX/EELS in Chapter 5 where the magnetic properties of the nanoparticles arrays were also evaluated by SQUID magnetometer. The preliminary results of the OPV devices with γ-Fe_2O_3 showed a positive effect on the performance, yet more device investigation needed to be carried out for further exploration.

As dispersion of the nanoparticles is of interest in terms of actual organic electronic devices and magnetic properties, Chapter 6 summarized several methods to effect the dispersion which was evaluated quantitatively using the disLocate package in Mathematica, showed that homopolymer poly(2-vinyl pyridine) assisted loading improved

the lateral order of the nanoparticles with great success. In addition, the size tuning of the nanoparticles was also achieved by changing the loading ratio of $FeCl_3$ below the maximum loading.

7.2 Outlook

γ-Fe_2O_3 nanoparticles can be generated with high degree controllability in terms of size and dispersion using the method in this thesis, whose processes are compatible with the actual organic electronic devices (such as OPV, and OLED) fabrication. Incorporating these nanoparticles into the standard devices is a good starting point moving forward to investigate the electrode modification effect with and without the external magnetic field, which might provide a further understanding about the charge carriers spin injection mechanism. In addition, potential future studies could be devoted to exploring the relationship between the dispersion of magnetic nanoparticles and the related magnetic properties. The iron oxide nanoparticles are ready to be applied to many potential applications in either academia or industry.

Bibliography

[1] Stephen R. Forrest. "The path to ubiquitous and low-cost organic electronic appliances on plastic". In: *Nature* 428.6986 (2004), pp. 911–918. ISSN: 00280836. DOI: 10.1038/nature02498. arXiv: 1.

[2] Bernard Geffroy, Philippe le Roy, and Christophe Prat. "Organic light-emitting diode (OLED) technology: Materials, devices and display technologies". In: *Polymer International* 55.6 (2006), pp. 572–582. ISSN: 09598103. DOI: 10.1002/pi.1974.

[3] Serap Günes, Helmut Neugebauer, and Niyazi Serdar Sariciftci. "Conjugated polymer-based organic solar cells". In: *Chemical Reviews* 107.4 (2007), pp. 1324–1338. ISSN: 00092665. DOI: 10.1021/cr050149z. arXiv: arXiv:1011.1669v3.

[4] Frederik C. Krebs. *Fabrication and processing of polymer solar cells: A review of printing and coating techniques*. 2009. DOI: 10.1016/j.solmat.2008.10.004.

[5] Chengmei Zhong, Chunhui Duan, Fei Huang, Hongbin Wu, and Yong Cao. "Materials and devices toward fully solution processable organic light-emitting diodes". In: *Chemistry of Materials* 23.3 (2011), pp. 326–340. ISSN: 08974756. DOI: 10.1021/cm101937p.

[6] Takatoshi Tsujimura et al. "Development of flexible organic light-emitting diode on barrier film and roll-to-roll manufacturing". In: *Journal of the Society for Information Display* 22.8 (2014), pp. 412–418. ISSN: 19383657. DOI: 10.1002/jsid.261.

[7] Lukas Kinner et al. "Inkjet-printed embedded Ag-PEDOT:PSS electrodes with improved light out coupling effects for highly efficient ITO-free blue polymer light

emitting diodes". In: *Applied Physics Letters* 110.10 (2017). ISSN: 00036951. DOI: 10.1063/1.4978429.

[8] Tsuyoshi Sekitani and Tokao Someya. "Stretchable, large-area organic electronics". In: *Advanced Materials* 22.20 (2010), pp. 2228–2246. ISSN: 09359648. DOI: 10.1002/adma.200904054. arXiv: 84863200485.

[9] Hong Ma, Hin-Lap Yip, Fei Huang, and Alex K.-Y. Jen. "Interface Engineering for Organic Electronics". In: *Advanced Functional Materials* 20.9 (2010), pp. 1371–1388. ISSN: 1616301X. DOI: 10.1002/adfm.200902236. URL: http://doi.wiley.com/10.1002/adfm.200902236.

[10] By Hisao Ishii, Kiyoshi Sugiyama, Eisuke Ito, and Kazuhiko Seki. "Energy Level Alignment and Interfacial Electronic Structures at Organic / Metal and Organic / Organic Interfaces **". In: *Advanced Materials* (1999), pp. 605–625. ISSN: 0935-9648. DOI: 10.1002/(SICI)1521-4095(199906)11:8<605::AID-ADMA605>3.0.CO;2-Q.

[11] Mark T Greiner and Zheng-Hong Lu. "Thin-film metal oxides in organic semiconductor devices: their electronic structures, work functions and interfaces". In: *NPG Asia Materials* 5.7 (2013), e55. ISSN: 1884-4057. DOI: 10.1038/am.2013.29. URL: http://dx.doi.org/10.1038/am.2013.29.

[12] Yuhang Liu et al. "Aggregation and morphology control enables multiple cases of high-efficiency polymer solar cells". In: *Nature Communications* 5 (2014). ISSN: 20411723. DOI: 10.1038/ncomms6293. arXiv: arXiv:1011.1669v3.

[13] Z. B. Wang et al. "Unlocking the full potential of organic light-emitting diodes on flexible plastic". In: *Nature Photonics* 5.12 (2011), pp. 753–757. ISSN: 17494885. DOI: 10.1038/nphoton.2011.259.

[14] Bin Hu, Liang Yan, and Ming Shao. "Magnetic-field effects in organic semiconducting materials and devices". In: *Advanced Materials* 21.14-15 (2009), pp. 1500–1516. ISSN: 09359648. DOI: 10.1002/adma.200802386.

[15] Kai Wang et al. "Solution-processed Fe3O4magnetic nanoparticle thin film aligned by an external magnetostatic field as a hole extraction layer for polymer solar cells". In: *ACS Applied Materials and Interfaces* 5.20 (2013), pp. 10325–10330. ISSN: 19448244. DOI: 10.1021/am4033179.

[16] Yue Wu, Bin Hu, Jane Howe, An Ping Li, and Jian Shen. "Spin injection from ferromagnetic Co nanoclusters into organic semiconducting polymers". In: *Physical Review B - Condensed Matter and Materials Physics* 75.7 (2007), pp. 1–5. ISSN: 10980121. DOI: 10.1103/PhysRevB.75.075413.

[17] Dan-Dan Zhang et al. "Enhanced hole injection in organic light-emitting devices by using Fe3O4 as an anodic buffer layer". In: *Applied Physics Letters* 94.22 (2009), p. 223306. ISSN: 0003-6951. DOI: 10.1063/1.3148657. URL: http://aip.scitation.org/doi/10.1063/1.3148657.

[18] Jing Feng et al. "Magnetic Nanofilm of Fe3O4 for Highly Efficient Organic Light-Emitting Devices". In: *Journal of Physical Chemistry C* 114.14 (2010), pp. 6718–6721. ISSN: 1932-7447. DOI: 10.1021/jp9122503.

[19] R M Cornell and U Schwertmann. "The iron oxides: structure, properties, reactions, occurences and uses". In: *Wiley-Vch.* 2003, ISBN: 3–527–30274–3. ISBN: 3527302743. DOI: 10.1002/3527602097. arXiv: arXiv:1011.1669v3.

[20] Ajay Kumar Gupta and Mona Gupta. *Synthesis and surface engineering of iron oxide nanoparticles for biomedical applications*. 2005. DOI: 10.1016/j.biomaterials.2004.10.012. arXiv: 9809069v1 [arXiv:gr-qc].

[21] S Laurent et al. "Magnetic Iron Oxide Nanoparticles: Synthesis, Stabilization, Vectorization, Physicochemical Characterizations, and Biological Applications (vol 108, pg 2064, 2008)". In: *Chemical Reviews* 108.6 (2008), pp. 2064–2110. ISSN: 00092665. DOI: Doi10.1021/Cr900197g.

[22] Monty Liong et al. "Multifunctional inorganic nanoparticles for imaging, targeting, and drug delivery". In: *ACS Nano* 2.5 (2008), pp. 889–896. ISSN: 19360851. DOI: 10.1021/nn800072t. arXiv: NIHMS150003.

[23] Zhen Li, Li Wei, Mingyuan Gao, and Hao Lei. "One-pot reaction to synthesize biocompatible magnetite nanoparticles". In: *Advanced Materials* 17.8 (2005), pp. 1001–1005. ISSN: 09359648. DOI: 10.1002/adma.200401545.

[24] Hyon Bin Na, In Chan Song, and Taeghwan Hyeon. "Inorganic nanoparticles for MRI contrast agents". In: *Advanced Materials* 21.21 (2009), pp. 2133–2148. ISSN: 09359648. DOI: 10.1002/adma.200802366. arXiv: arXiv:1408.1149.

[25] Sophie Laurent, Silvio Dutz, Urs O. Häfeli, and Morteza Mahmoudi. *Magnetic fluid hyperthermia: Focus on superparamagnetic iron oxide nanoparticles*. 2011. DOI: 10.1016/j.cis.2011.04.003. arXiv: NIHMS150003.

[26] Ana Espinosa et al. "Duality of Iron Oxide Nanoparticles in Cancer Therapy: Amplification of Heating Efficiency by Magnetic Hyperthermia and Photothermal Bimodal Treatment". In: *ACS Nano* 10.2 (2016), pp. 2436–2446. ISSN: 1936086X. DOI: 10.1021/acsnano.5b07249. arXiv: NIHMS150003.

[27] Taeghwan Hyeon. "Chemical synthesis of magnetic nanoparticles". In: *Chemical Communications* 8 (2003), pp. 927–934. ISSN: 13597345. DOI: 10.1039/b207789b. URL: http://xlink.rsc.org/?DOI=b207789b.

[28] Pier Paolo Prosini, Maria Carewska, Stefano Loreti, Carla Minarini, and Stefano Passerini. "Lithium iron oxide as alternative anode for li-ion batteries". In: *International Journal of Inorganic Materials* 2.4 (2000), pp. 365–370. ISSN: 14666049. DOI: 10.1016/S1466-6049(00)00028-3.

[29] Karel Široký, Jana Jirešová, Lubomir Lubomír Hudec, Karel Sirok, and Jana Jire. "Iron oxide thin film gas sensor". In: *Thin Solid Films* 245.1–2 (1994), pp. 211–214. ISSN: 00406090. DOI: http://dx.doi.org/10.1016/0040-6090(94)90902-4. URL: http://www.sciencedirect.com/science/article/pii/0040609094909024.

[30] Benjamin M. Klahr, Alex B. F. Martinson, and Thomas W. Hamann. "Photoelectrochemical Investigation of Ultrathin Film Iron Oxide Solar Cells Prepared by Atomic Layer Deposition". In: *Langmuir* 27.1 (2011), pp. 461–468. ISSN: 0743-7463. DOI: 10.1021/la103541n. URL: http://pubs.acs.org/doi/abs/10.1021/la103541n.

[31] Kai Wang et al. "Effects of magnetic nanoparticles and external magnetostatic field on the bulk heterojunction polymer solar cells". In: *Scientific Reports* 5 (2015), pp. 1–9. ISSN: 20452322. DOI: 10.1038/srep09265.

[32] An Hui Lu, E. L. Salabas, and Ferdi Schüth. "Magnetic nanoparticles: Synthesis, protection, functionalization, and application". In: *Angewandte Chemie - International Edition* 46.8 (2007), pp. 1222–1244. ISSN: 14337851. DOI: 10.1002/anie.200602866.

[33] Liheng Wu, Adriana Mendoza-Garcia, Qing Li, and Shouheng Sun. "Organic Phase Syntheses of Magnetic Nanoparticles and Their Applications". In: *Chemical Reviews* 116.18 (2016), pp. 10473–10512. ISSN: 15206890. DOI: 10.1021/acs.chemrev.5b00687.

[34] Unyong Jeong, Xiaowei Teng, Yong Wang, Hong Yang, and Younan Xia. "Superparamagnetic colloids: Controlled synthesis and niche applications". In: *Advanced Materials* 19.1 (2007), pp. 33–60. ISSN: 09359648. DOI: 10.1002/adma.200600674.

[35] Shunsuke Sakurai, Asuka Namai, Kazuhito Hashimoto, and Shin-ichi Ohkoshi. "First Observation of Phase Transformation of All Four Fe 2O 3Phases ($\gamma \rightarrow \epsilon \rightarrow \beta \rightarrow \alpha$-Phase)". In: *Journal of the American Chemical Society* 131.51 (2009), pp. 18299–18303. URL: http://pubs.acs.org/doi/abs/10.1021/ja9046069{\%}0Apapers3://publication/doi/10.1021/ja9046069.

[36] Libor MacHala, Jiří Tuček, and Radek Zbořil. "Polymorphous transformations of nanometric iron(III) oxide: A review". In: *Chemistry of Materials* 23.14 (2011), pp. 3255–3272. ISSN: 08974756. DOI: 10.1021/cm200397g.

[37] Young Soo Kang, Subhash Risbud, John F. Rabolt, and Pieter Stroeve. "Synthesis and Characterization of Nanometer-Size Fe ₃ O ₄ and γ-Fe ₂ O ₃ Particles". In: *Chemistry of Materials* 8.9 (1996), pp. 2209–2211. ISSN: 0897-4756. DOI: 10.1021/cm960157j. URL: http://pubs.acs.org/doi/abs/10.1021/cm960157j.

[38] Wenhui Zhu et al. "Atomic structural evolution during the reduction of α-Fe2O3nanowires". In: *Journal of Physical Chemistry C* 120.27 (2016), pp. 14854–14862. ISSN: 19327455. DOI: 10.1021/acs.jpcc.6b02033.

[39] M. Ibrahim Dar and S. A. Shivashankar. "Single crystalline magnetite, maghemite, and hematite nanoparticles with rich coercivity". In: *RSC Adv.* 4.8 (2014), pp. 4105–4113. ISSN: 2046-2069. DOI: 10.1039/C3RA45457F. URL: http://xlink.rsc.org/?DOI=C3RA45457F.

[40] Radek Zboril, Miroslav Mashlan, Dagmar Krausova, and Petr Pikal. "Cubic β-Fe2O3 as the product of the thermal decomposition of Fe2(SO4)3". In: *Hyperfine Interactions* 120/121 (1999), pp. 497–501. ISSN: 03043843.

[41] Jian Jin, Shin Ichi Ohkoshi, and Kazuhito Hashimoto. "Giant Coercive Field of Nanometer-Sized Iron Oxide". In: *Advanced Materials* 16.1 (2004), pp. 48–51. ISSN: 09359648. DOI: 10.1002/adma.200305297.

[42] Jiří Tuček, Radek Zbořil, Asuka Namai, and Shin Ichi Ohkoshi. *ϵ-Fe2O3: An advanced nanomaterial exhibiting giant coercive field, millimeter-wave ferromagnetic resonance, and magnetoelectric coupling.* 2010. DOI: 10.1021/cm101967h.

[43] Xavier Batlle and A Labarta. "Finite-size effects in fine particles: magnetic and transport properties". In: *Journal of Physics D: Applied Physics* 15.35 (2002), R15–R42. ISSN: 0022-3727. DOI: 10.1088/0022-3727/35/6/201. URL: http://iopscience.iop.org/0022-3727/35/6/201.

[44] J. FRENKEL and J. DOEFMAN. "Spontaneous and Induced Magnetisation in Ferromagnetic Bodies". In: *Nature* 126.3173 (1930), pp. 274–275. ISSN: 0028-0836. DOI: 10.1038/126274a0. URL: http://www.nature.com/articles/126274a0.

[45] D L Hou, X F Nie, and H L Luo. "Studies on the magnetic viscosity and the magnetic anisotropy of gamma - Fe2O3 powders". In: *Applied Physics A* 66.1 (1998), pp. 109–114. ISSN: 09478396. DOI: 10.1007/s003390050646.

[46] A. I. Figueroa et al. "Magnetic Anisotropy of Maghemite Nanoparticles Probed by RF Transverse Susceptibility". In: *Physics Procedia* 75 (2015), pp. 1050–1057. ISSN: 18753892. DOI: 10.1016/j.phpro.2015.12.174.

[47] W. Wu et al. "Synthesis and magnetic properties of maghemite (γ-Fe2O3) short-nanotubes". In: *Nanoscale Research Letters* 5.9 (2010), pp. 1474–1479. ISSN: 19317573. DOI: 10.1007/s11671-010-9664-4.

[48] Diandra L. Leslie-Pelecky and Reuben D. Rieke. *Magnetic properties of nanostructured materials.* 1996. DOI: 10.1021/cm960077f.

[49] R. W. Chantrell, A. Lyberatos, M. El-Hilo, and K. O'Grady. "Models of slow relaxation in particulate and thin film materials (invited)". In: *Journal of Applied Physics* 76.10 (1994), pp. 6407–6412. ISSN: 00218979. DOI: 10.1063/1.358281.

[50] M. P. Morales, C. J. Serna, F. Bødker, and S. Mørup. "Spin canting due to structural disorder in maghemite". In: *Journal of Physics Condensed Matter* 9.25 (1997), pp. 5461–5467. ISSN: 09538984. DOI: 10.1088/0953-8984/9/25/013.

[51] M P Morales et al. "Surface and Internal Spin Canting in gamma -Fe2O3 Nanoparticles". In: *Chemistry of Materials* 11.11 (1999), pp. 3058–3064. ISSN: 08974756.

[52] Sang Hyun Yun et al. "Tunable magnetic arrangement of iron oxide nanoparticles in situ synthesized on the solid substrate from diblock copolymer micelles". In: *Langmuir* 21.14 (2005), pp. 6548–6552. ISSN: 07437463. DOI: 10.1021/la050418g.

[53] Masih Darbandi et al. "Nanoscale size effect on surface spin canting in iron oxide nanoparticles synthesized by the microemulsion method". In: *Journal of Physics D: Applied Physics* 45.19 (2012). ISSN: 00223727. DOI: 10.1088/0022-3727/45/19/195001.

[54] Asep Bayu Dani Nandiyanto and Kikuo Okuyama. "Progress in developing spray-drying methods for the production of controlled morphology particles: From the nanometer to submicrometer size ranges". In: *Advanced Powder Technology* 22.1 (2011), pp. 1–19. ISSN: 09218831. DOI: 10.1016/j.apt.2010.09.011. URL: http://dx.doi.org/10.1016/j.apt.2010.09.011.

[55] Cian Cummins, Tandra Ghoshal, Justin D. Holmes, and Michael A. Morris. "Strategies for Inorganic Incorporation using Neat Block Copolymer Thin Films for Etch Mask Function and Nanotechnological Application". In: *Advanced Materials* 28.27 (2016), pp. 5586–5618. ISSN: 09359648. DOI: 10.1002/adma.201503432. URL: http://doi.wiley.com/10.1002/adma.201503432.

[56] By Stephan Förster and Markus Antonietti. "Amphiphilic Block Copolymers in Structure- Controlled Nanomaterial Hybrids". In: *Advanced Materials* 10.3 (1998), pp. 195–217. ISSN: 0935-9648. DOI: 10.1002/(SICI)1521-4095(199802)10:3<195::AID-ADMA195>3.0.CO;2-V.

[57] Joachim P Spatz et al. "Ordered Deposition of Inorganic Clusters from Micellar Block Copolymer Films Ordered Deposition of Inorganic Clusters from Micellar

Block Copolymer Films". In: *Thin Solid Films* 16.2 (2000), pp. 407–415. DOI: 10.1021/la990070n.

[58] Stefan Mössmer et al. "Solution Behavior of Poly(styrene)- b lock -poly(2-vinylpyridine) Micelles Containing Gold Nanoparticles". In: *Macromolecules* 33.13 (2000), pp. 4791–4798. ISSN: 0024-9297. DOI: 10.1021/ma992006i. URL: http://pubs.acs.org/doi/abs/10.1021/ma992006i.

[59] S Foerster, M Zisenis, E Wenz, and M Antonietti. "Micellization of strongly segregated block copolymers". In: *The Journal of Chemical Physics* 104.24 (1996), pp. 9956–9970. ISSN: 00219606. DOI: 10.1063/1.471723. URL: http://link.aip.org/link/?JCPSA6/104/9956/1{\%}5Cnpapers2://publication/uuid/1EA3F467-0985-44A8-BFF9-0154EF86AC66.

[60] S. Förster, E. Wenz, and P. Lindner. "Density Profile of Spherical Polymer Brushes". In: *Physical Review Letters* 77 (1996), p. 95. ISSN: 0031-9007. DOI: 10.1103/PhysRevLett.77.95.

[61] Gerd Kästle et al. "Micellar Nanoreactors - Preparation and Characterization of Hexagonally Ordered Arrays of Metallic Nanodots". In: *Advanced Functional Materials* 13.11 (2003), pp. 853–861. ISSN: 1616301X. DOI: 10.1002/adfm.200304332.

[62] Ulf Wiedwald, Luyang Han, Johannes Biskupek, Ute Kaiser, and Paul Ziemann. "Preparation and characterization of supported magnetic nanoparticles prepared by reverse micelles". In: *Beilstein Journal of Nanotechnology* 1.1 (2010), pp. 24–47. ISSN: 21904286. DOI: 10.3762/bjnano.1.5.

[63] M Antonietti, E Wenz, L Bronstein, and M Seregina. "Synthesis and characterization of noble metal colloids in block copolymer micelles". In: *Advanced Materials* 7.12 (1995), 1000–&. DOI: 10.1002/adma.19950071205.

[64] C. W. Ow-Yang et al. "Work function tuning of tin-doped indium oxide electrodes with solution-processed lithium fluoride". In: *Thin Solid Films* 559 (2014), pp. 58–63. ISSN: 00406090. DOI: 10.1016/j.tsf.2013.11.035. URL: http://dx.doi.org/10.1016/j.tsf.2013.11.035.

[65] Sivashankar Krishnamoorthy, Raphaël Pugin, Jürgen Brugger, Harry Heinzelmann, and Christian Hinderling. "Tuning the dimensions and periodicities of nanostructures starting from the same polystyrene-block-poly(2-vinylpyridine)

diblock copolymer". In: *Advanced Functional Materials* 16.11 (2006), pp. 1469–1475. ISSN: 1616301X. DOI: 10.1002/adfm.200500524.

[66] Matt Bumstead, Kunyu Liang, Gregory Hanta, Lok Shu Hui, and Ayse Turak. "DisLocate: Tools to rapidly quantify local intermolecular structure to assess two-dimensional order in self-assembled systems". In: *Scientific Reports* 8.1 (2018), pp. 1–15. ISSN: 20452322. DOI: 10.1038/s41598-017-18894-7. URL: http://dx.doi.org/10.1038/s41598-017-18894-7.

[67] B. Roldan Cuenya et al. "Size-dependent evolution of the atomic vibrational density of states and thermodynamic properties of isolated Fe nanoparticles". In: *Physical Review B - Condensed Matter and Materials Physics* 86.16 (2012), pp. 1–11. ISSN: 10980121. DOI: 10.1103/PhysRevB.86.165406.

[68] Lianchen Shan et al. "Homopolymers as Nanocarriers for the Loading of Block Copolymer Micelles with Metal Salts: A Facile Way to Large-scale Ordered Arrays of Transition-metal Nanoparticles". In: *Journal of Materials Chemistry C* 2.4 (2014), pp. 701–707. ISSN: 2050-7526. DOI: 10.1039/c3tc31333f. URL: http://dx.doi.org/10.1039/C3TC31333F.

[69] Yoshio Sageshima, Atsushi Noro, and Yushu Matsushita. "Structural isomer effects on the morphology of block copolymer/metal salts hybrids". In: *Journal of Polymer Science, Part B: Polymer Physics* 52.5 (2014), pp. 377–386. ISSN: 08876266. DOI: 10.1002/polb.23421.

[70] Vitalij K. Pecharsky and Peter Y. Zavalij. *Fundamentals of powder diffraction and structural characterization of materials*. 2005, pp. 1–713. ISBN: 0387241477. DOI: 10.1007/b106242. arXiv: arXiv:1011.1669v3.

[71] S. Poulin, R. França, L. Moreau-Bélanger, and E. Sacher. "Confirmation of X-ray photoelectron spectroscopy peak attributions of nanoparticulate iron oxides, using symmetric peak component line shapes". In: *Journal of Physical Chemistry C* 114.24 (2010), pp. 10711–10718. ISSN: 19327447. DOI: 10.1021/jp100964x.

[72] Challa S.S.R. Kumar. *Raman spectroscopy for nanomaterials characterization*. Vol. 9783642206. 2012, pp. 1–645. ISBN: 9783642206207. DOI: 10.1007/978-3-642-20620-7. arXiv: arXiv:1011.1669v3.

[73] D.L.a. de Faria, S.V. Silva, and M.T. de Oliveira. "Raman microspectroscopy of some iron oxides and oxyhydroxides". In: *Journal of Raman Spectroscopy* 28.February (1997), pp. 873–878. ISSN: 1097-4555. DOI: 10.1002/(SICI)1097-4555(199711)28:11<873::AID-JRS177>3.0.CO;2-B.

[74] Irina Chamritski and Gary Burns. "Infrared- And raman-active phonons of magnetite, maghemite, and hematite: A computer simulation and spectroscopic study". In: *Journal of Physical Chemistry B* 109.11 (2005), pp. 4965–4968. ISSN: 15206106. DOI: 10.1021/jp048748h.

[75] Yongqi Liang and Roel van de Krol. "Influence of Si dopant and SnO2interfacial layer on the structure of the spray-deposited Fe2O3films". In: *Chemical Physics Letters* 479.1-3 (2009), pp. 86–90. ISSN: 00092614. DOI: 10.1016/j.cplett.2009.07.093. URL: http://dx.doi.org/10.1016/j.cplett.2009.07.093.

[76] J. López-Sánchez et al. "Sol–Gel Synthesis and Micro-Raman Characterization of ϵ-Fe ₂ O ₃ Micro- and Nanoparticles". In: *Chemistry of Materials* 28.2 (2016), pp. 511–518. ISSN: 0897-4756. DOI: 10.1021/acs.chemmater.5b03566. URL: http://pubs.acs.org/doi/10.1021/acs.chemmater.5b03566.

[77] John R Ferraro, Kazuo Nakamoto, and Chris W Brown. *Introductory Raman Spectroscopy*. 2003, pp. 406–421. ISBN: 9780122541056. DOI: 10.1002/jrs.1407. arXiv: arXiv:1011.1669v3.

[78] W H Tsai, F J Boerio, S J Clarson, E E Parsonage, and M Tirrell. "characterization of Adsorbed 2-Vinylpyridine/Styrene Diblock Copolymers on Silver Surfaces Using Surface-Enhanced Raman Scattering." In: *Macromolecules* 25 (1992), p. 2538.

[79] P P Hong, F. J. Boerio, and M. Tirrell. "An Investigation of the Adsorption of Polystyrene/ Poly(2-vinylpyridine) Diblock Copolymers onto Silver Substrates Using Surface-Enhanced Raman Scattering". In: *Macromolecules* (1993), pp. 3953–3959.

[80] Katsuo Murata and Donald E. Irish. "Raman studies of the hydrated melt of FeCl36H2O". In: *Spectrochimica Acta Part A: Molecular Spectroscopy* 44.7 (1988), pp. 739–743. ISSN: 05848539. DOI: 10.1016/0584-8539(88)80136-3.

[81] Pamela S. Hill and Edwin A. Schauble. "Modeling the effects of bond environment on equilibrium iron isotope fractionation in ferric aquo-chloro complexes". In: *Geochimica et Cosmochimica Acta* 72.8 (2008), pp. 1939–1958. ISSN: 00167037. DOI: 10.1016/j.gca.2007.12.023.

[82] W. J. Zhao, P. H. Tan, J. Liu, and A. C. Ferrari. "Intercalation of Few-Layer Graphite Flakes with FeCl3: Raman Determination of Fermi Level, Layer Decoupling and Stability". In: (2010), pp. 5941–5946. arXiv: 1012.1836. URL: http://arxiv.org/abs/1012.1836.

[83] M Aizawa and J Buriak. "Block Copolymer Templated Chemistry for the Formation of \nMetallic Nanoparticle Arrays on Semiconductor Surfaces \n". In: *Chem. Mater* 1 (2007), pp. 5090–5101. ISSN: 0897-4756. DOI: 10.1021/cm071382b. URL: http://www.ncbi.nlm.nih.gov/entrez/query.fcgi?db=pubmed{\&}cmd=Retrieve{\&}dopt=AbstractPlus{\&}list{_}uids=13512680900064352339related:U5iKc6-vhrsJ{\%}5Cnhttp://pubs.acs.org/doi/abs/10.1021/cm071382b.

[84] Jinan Chai and Jillian M. Buriak. "Using cylindrical domains of block copolymers to self-assemble and align metallic nanowires". In: *ACS Nano* 2.3 (2008), pp. 489–501. ISSN: 19360851. DOI: 10.1021/nn700341s.

[85] Nathanael L.Y. Wu et al. "Density doubling of block copolymer templated features". In: *Nano Letters* 12.1 (2012), pp. 264–268. ISSN: 15306984. DOI: 10.1021/nl203488a.

[86] L Reimer. "Scanning Electron Microscopy: Physics of Image Formation and Microanalysis, Second Edition". In: *Measurement Science and Technology* 11.Dlc (2000), p. 1826. ISSN: 0957-0233. DOI: 10.1088/0957-0233/11/12/703. URL: http://stacks.iop.org/0957-0233/11/i=12/a=703.

[87] Joseph Goldstein et al. *Scanning Electron Microscopy and X-Ray Microanalysis: A Text for Biologists, Materials Scientists, and Geologists*. 2012. DOI: 10.10071/978-1-4613-0491-3. URL: https://books.google.com/books?hl=en{\&}lr={\&}id=25nxBwAAQBAJ{\&}pgis=1.

[88] Dong Ok Shin et al. "Multicomponent nanopatterns by directed block copolymer self-assembly". In: *ACS Nano* 7.10 (2013), pp. 8899–8907. ISSN: 19360851. DOI: 10.1021/nn403379k.

[89] Seung Hyun et al. "Self-Positioned Nanosized Mask for Transparent and Flexible Ferroelectric Polymer Nanodiodes Array". In: *ACS Applied Materials and Interfaces* 8.40 (2016), pp. 27074–27080. ISSN: 19448252. DOI: 10.1021/acsami.6b08459.

[90] Ulf Wiedwald et al. "From colloidal Co/CoO core/shell nanoparticles to arrays of metallic nanomagnets: Surface modification and magnetic properties". In: *ChemPhysChem* 6.12 (2005), pp. 2522–2526. ISSN: 14394235. DOI: 10.1002/cphc.200500148.

[91] R. Russo et al. "Nanoparticle magnetization measurements by a high sensitive nano-superconducting quantum interference device". In: *Applied Physics Letters* 101.12 (2012), pp. 1–5. ISSN: 00036951. DOI: 10.1063/1.4751036.

[92] J Orna et al. "Origin of the giant magnetic moment in epitaxial Fe3O4 thin films". In: *Phys. Rev. B* 81.14 (2010), p. 144420. ISSN: 1550-235X. DOI: 10.1103/PhysRevB.81.144420. URL: http://link.aps.org/doi/10.1103/PhysRevB.81.144420.

[93] J. A. Moyer, S. Lee, P. Schiffer, and L. W. Martin. "Magnetically disordered phase in epitaxial iron-deficient <math> <mrow> <mi mathvariant="normal">F</mi> <msub> <mi mathvariant="normal">e</mi> <mn>3</mn> </msub> <msub> <mi mathvariant="normal">O</mi> <mn>4</mn> </msub> </mrow> </math> thin films". In: *Physical Review B* 91.6 (2015), p. 064413. ISSN: 1098-0121. DOI: 10.1103/PhysRevB.91.064413. URL: https://link.aps.org/doi/10.1103/PhysRevB.91.064413.

[94] R. L. Fagaly. "Superconducting quantum interference device instruments and applications". In: *Review of Scientific Instruments* 77.10 (2006), pp. 1–45. ISSN: 00346748. DOI: 10.1063/1.2354545.

[95] E. L. Frankevich et al. "Polaron-pair generation in poly(phenylene vinylenes)". In: *Physical Review B* 46.15 (1992), pp. 9320–9324. ISSN: 01631829. DOI: 10.1103/PhysRevB.46.9320.

[96] Vom Fachbereich Material and Grades Doktor-ingenieur. "Magnetic field effect in organic light emitting diodes". In: (2010).

[97] O. Taboubi et al. "Magnetic Field Effects on the Current of PCPDTBT-based Diode". In: *Journal of Physical Chemistry C* 121.21 (2017), pp. 11727–11732. ISSN: 19327455. DOI: 10.1021/acs.jpcc.7b03539.

[98] Frkdkric Calderara, Ge Riess, Ecole Nationale, Supcrieure De Chimie, and Alfred Werner. "Characterization of polystyrene-block-poly (4-vinyl- pyridine) block copolymer micelles in toluene solution". In: *Macromol.Chem.Phys* 197 (1996), pp. 2115–2132.

[99] I. Horcas et al. "WSXM: A software for scanning probe microscopy and a tool for nanotechnology". In: *Review of Scientific Instruments* 78.1 (2007). ISSN: 00346748. DOI: 10.1063/1.2432410.

[100] Aaron M. Jubb and Heather C. Allen. "Vibrational spectroscopic characterization of hematite, maghemite, and magnetite thin films produced by vapor deposition". In: *ACS Applied Materials and Interfaces* 2.10 (2010), pp. 2804–2812. ISSN: 19448244. DOI: 10.1021/am1004943.

[101] Igor Chourpa et al. "Molecular composition of iron oxide nanoparticles, precursors for magnetic drug targeting, as characterized by confocal Raman microspectroscopy". In: *The Analyst* 130.10 (2005), p. 1395. ISSN: 0003-2654. DOI: 10.1039/b419004a. URL: http://xlink.rsc.org/?DOI=b419004a.

[102] D Bersani, P P Lottici, and a Montenero. "Micro-Raman Investigation of Iron Oxide Films and Powders Produced by Sol – Gel Syntheses". In: *Journal of Raman Spectroscopy* 30.February 1998 (1999), pp. 355–360. ISSN: 03770486. DOI: 10.1002/(SICI)1097-4555(199905)30:5<355::AID-JRS398>3.0.CO;2-C.

[103] N. Caswell and S. A. Solin. "Vibrational excitations of pure FeCl3and graphite intercalated with ferric chloride". In: *Solid State Communications* 27.10 (1978), pp. 961–967. ISSN: 00381098. DOI: 10.1016/0038-1098(78)91015-3.

[104] Maria F. Casula et al. "The concept of delayed nucleation in nanocrystal growth demonstrated for the case of iron oxide nanodisks". In: *Journal of the American Chemical Society* 128.5 (2006), pp. 1675–1682. ISSN: 00027863. DOI: 10.1021/ja056139x.

[105] Olga N. Shebanova and Peter Lazor. "Raman spectroscopic study of magnetite (FeFe2O4): A new assignment for the vibrational spectrum". In: *Journal of Solid State Chemistry* 174.2 (2003), pp. 424–430. ISSN: 00224596. DOI: 10.1016/S0022-4596(03)00294-9.

[106] Guilherme V M Jacintho, Paola Corio, and Joel C. Rubim. "Surface-enhanced Raman spectra of magnetic nanoparticles adsorbed on a silver electrode". In: *Journal of Electroanalytical Chemistry* 603.1 (2007), pp. 27–34. ISSN: 15726657. DOI: 10.1016/j.jelechem.2007.02.019.

[107] I. V. Chernyshova, M. F. Hochella Jr, and A. S. Madden. "Size-dependent structural transformations of hematite nanoparticles. 1. Phase transition". In: *Physical Chemistry Chemical Physics* 9.14 (2007), p. 1736. ISSN: 1463-9076. DOI: 10.1039/b618790k. URL: http://xlink.rsc.org/?DOI=b618790k.

[108] Ryan D. Bennett et al. "Strategies for controlling the planar arrangement of block copolymer micelles and inorganic nanoclusters". In: *Macromolecules* 38.26 (2005), pp. 10728–10735. ISSN: 00249297. DOI: 10.1021/ma0518555.

[109] Wei Cheng, Kaibin Tang, Yunxia Qi, Jie Sheng, and Zhongpin Liu. "One-step synthesis of superparamagnetic monodisperse porous Fe3O4 hollow and core-shell spheres". In: *Journal of Materials Chemistry* 20.9 (2010), p. 1799. ISSN: 0959-9428. DOI: 10.1039/b919164j. URL: http://xlink.rsc.org/?DOI=b919164j.

[110] M. Baalousha and J. R. Lead. "Rationalizing nanomaterial sizes measured by atomic force microscopy, flow field-flow fractionation, and dynamic light scattering: Sample preparation, polydispersity, and particle structure". In: *Environmental Science and Technology* 46.11 (2012), pp. 6134–6142. ISSN: 0013936X. DOI: 10.1021/es301167x.

[111] I. Dzyaloshinsky. "A thermodynamic theory of "weak" ferromagnetism of antiferromagnetics". In: *Journal of Physics and Chemistry of Solids* 4.4 (1958), pp. 241–255. ISSN: 00223697. DOI: 10.1016/0022-3697(58)90076-3. URL: http://linkinghub.elsevier.com/retrieve/pii/0022369758900763.

[112] Pham V. Huong. "Structural studies of diamond films and ultrahard materials by Raman and micro-Raman spectroscopies". In: *Diamond and Related Materials*

1.1 (1991), pp. 33–41. ISSN: 09259635. DOI: 10.1016/0925-9635(91)90009-Y.

[113] André Moliton and Jean-Michel Nunzi. "How to model the behaviour of organic photovoltaic cells". In: *Polymer International* 55.6 (2006), pp. 583–600. ISSN: 1097-0126. DOI: 10.1002/pi.2038. URL: http://onlinelibrary.wiley.com/doi/10.1002/pi.2038/abstract{\%}5Cnhttp://onlinelibrary.wiley.com/doi/10.1002/pi.2038/full{\%}5Cnhttp://onlinelibrary.wiley.com/doi/10.1002/pi.2038/pdf.

[114] A. Turak et al. "Systematic analysis of processing parameters on the ordering and performance of working poly(3-hexyl-thiophene):[6,6]-phenyl C61 -butyric acid methyl ester solar cells". In: *Journal of Renewable and Sustainable Energy* 2.5 (2010), pp. 1–14. ISSN: 19417012. DOI: 10.1063/1.3488381.

[115] Caroline A Schneider, Wayne S Rasband, and Kevin W Eliceiri. "NIH Image to ImageJ: 25 years of image analysis". In: *Nature Methods* 9.7 (2012), pp. 671–675. ISSN: 1548-7091. DOI: 10.1038/nmeth.2089. arXiv: arXiv:1011.1669v3. URL: http://www.nature.com/doifinder/10.1038/nmeth.2089.

[116] Seong Il Yoo, Byeong Hyeok Sohn, Wang Cheol Zin, Jin Chul Jung, and Cheolmin Park. "Mixtures of diblock copolymer micelles by different mixing protocols". In: *Macromolecules* 40.23 (2007), pp. 8323–8328. ISSN: 00249297. DOI: 10.1021/ma071534o.

[117] Seung Min Jeon, Sung Hwa Lee, Seong Il Yoo, and Byeong Hyeok Sohn. "Ordered complex nanostructures from bimodal self-assemblies of diblock copolymer micelles with solvent annealing". In: *Langmuir* 27.19 (2011), pp. 12191–12196. ISSN: 07437463. DOI: 10.1021/la202664m.

[118] John G. Kirkwood and Elizabeth Monroe Boggs. "The Radial Distribution Function in Liquids". In: *The Journal of Chemical Physics* 10.6 (1942), pp. 394–402. ISSN: 0021-9606. DOI: 10.1063/1.1723737. URL: http://aip.scitation.org/doi/10.1063/1.1723737.

[119] A Okabe, B Boots, K Sugihara, Chiu SN, and D.G. Kendall. *Spatial Tessellations - Concepts and Applications od Voronoi Diagrams*. 1. 2000, pp. 503–526. ISBN: 9780470317013. DOI: 10.1002/9780470317013. URL: http://doi.wiley.com/10.1002/9780470317013.

[120] Larysa Burtseva and Frank Werner. "Modeling of Spherical Particle Packing Structures Using Mathematical Tessellation". In: *Integration The Vlsi Journal* MARCH (2007), pp. 1–29. DOI: 10.13140/2.1.2664.7840.

[121] J B Parse and J A Wert. "A geometrical description of particle distributions in materials". In: *Modelling and Simulation in Materials Science and Engineering* 1.3 (1993), pp. 275–296. ISSN: 0965-0393. DOI: 10.1088/0965-0393/1/3/003. URL: http://stacks.iop.org/0965-0393/1/i=3/a=003{\%}0Ahttp://stacks.iop.org/0965-0393/1/i=3/a=003?key=crossref.1ae1759cd3eeb1f81cad96f70e0d8931.

[122] Yong Wang, Ulrich Go, and Martin Steinhart. "Mesoporous Block Copolymer Nanorods by Swelling-Induced Morphology Reconstruction". In: (2008).

[123] D Voulgaris, C Tsitsilianis, F J Esselink, and G Hadziioannou. "Polystyrene poly(2-vinyl pyridine) heteroarm star copolymer micelles in toluene: morphology and thermodynamics". In: *Polymer* 39.25 (1998), pp. 6429–6439. ISSN: 00323861.

[124] Anitha Ethirajan, Sathya Punniyakoti, Marc D'Olieslaeger, Patrick Wagner, and Hans Gerd Boyen. "Ultrafast self-assembly using ultrasound: A facile route to the rapid fabrication of well-ordered dense arrays of inorganic nanostructures". In: *Angewandte Chemie - International Edition* 52.37 (2013), pp. 9709–9713. ISSN: 14337851. DOI: 10.1002/anie.201301980.

Acknowledgements

At the end of my thesis, I would like to show my appreciation and thank to all the people who have helped and supported my study at McMaster University for the past two years.

I would like to express my gratitude to Dr. Ayse Turak for offering me the opportunity to become a graduate student in her group and for giving me academic supervision. Thanks for her supports, suggestions, and discussions, I have learned and developed many professional skills that will definitely lay a solid foundation for my future career.

Many thanks go to Dr. Turak's research group for the strong support throughout the project. Notable graduate student group members include Lok Shu Hui, Gregory Hanta, Matt Bumstead, Erinn van Wynsberghe. Thank you all for the valuable discussions and feedbacks which exert a positive impact on my thesis project. Thanks to the undergraduate student Emma Mogus, Lazar Kojovic, Colin Beswick for their work in devices fabrication. In addition, special thanks go to Dr. Zhilin Peng for the help in using SEM, to Dr. Carmen Andrei for the help in using TEM, and to Dr. Dube for the help in using SQUID.

I would like to thank the committee members: Dr. Preston, Dr. Knights, Dr. Saravanamuttu and Dr. Turak for their valuable input and time for my thesis defense.

Finally, I am very grateful to my parents for their endless support and encouragement.